

Study on Image Quality Improvement Methods for Underwater Imaging Systems

著者	Lu Huimin
year	2014-03
その他のタイトル	水中イメージングシステムのための画質改善に関する研究
学位授与年度	平成25年度
学位授与番号	17104甲工第367号
URL	http://hdl.handle.net/10228/5288

博士学位論文

水中イメージングシステムのための画
質改善に関する研究

平成25年度

陸 慧敏

九州工業大学大学院 工学府 電気電子工学専攻

Ph.D. Thesis

Study on Image Quality Improvement Methods
for Underwater Imaging Systems

by

Huimin Lu

B.S., Yangzhou University (2009)

M.E., Yangzhou University (2011)

M.E., Kyushu Institute of Technology (2011)

Submitted in partial fulfillment of the requirements for

the degree of Ph.D. of Engineering

at the

KYUSHU INSTITUTE OF TECHNOLOGY

March, 2014

© Copyright 2014 by Huimin Lu
All Rights Reserved

TABLE OF CONTENTS

LIST OF TABLES	IV
LIST OF FIGURES	V
LIST OF ACRONYMS	VIII
ABSTRACT	X
CHAPTER 1 INTRODUCTION.....	1
1.1 BACKGROUND	1
1.2 UNDERWATER IMAGING SYSTEMS	2
1.2.1 Acoustic Imaging	2
1.2.2 Optical Imaging	3
1.3 CHALLENGES OF UNDERWATER IMAGING SYSTEMS	7
1.3.1 Hardware Based Approach	8
1.3.2 Non-hardware Based Approach.....	10
1.4 OUTLINE OF THE APPROACHES	12
1.5 CONTRIBUTIONS	13
1.6 THESIS STRUCTURE	14
CHAPTER 2 MULTI-SOURCE IMAGES FUSION	17
2.1 BACKGROUND	17
2.2 SONAR IMAGE PRE-PROCESSING	18
2.3 LOCAL ENERGY FUSION	22
2.3.1 Energy of Image	22
2.3.2 Principle of Local Energy	23
2.3.3 Maximum Local Energy	25
2.4 EXPERIMENTS AND DISCUSSIONS	27

2.5 CONCLUSION	31
CHAPTER 3 LASER IMAGES DENOISING	32
3.1 BACKGROUND	34
3.1.1 Soft-thresholding Denoising.....	34
3.1.2 Generalized Spherically Contoured Exponential	34
3.2 BAYESIAN CONTOURLET ESTIMATOR OF BKF.....	35
3.3 QUALITY METRICS	38
3.4 EXPERIMENTS AND DISCUSSIONS	39
3.5 CONCLUSION	41
CHAPTER 4 OPTICAL IMAGE DEHAZING	42
4.1 BACKGROUND	42
4.2 BILATERAL FILTER AND TRIGONOMETRIC BILATERAL FILTER	44
4.2.1 Bilateral Filter.....	44
4.2.2 Box Filter.....	45
4.2.3 Trigonometric Bilateral Filter.....	45
4.3 GTBF FOR DEHAZING	46
4.3.1 Guided Trigonometric Bilateral Filtering.....	49
4.3.2 Recovering the Scene Radiance	49
4.4 ARTIFICIAL LIGHT INHOMOGENEITIES CORRECTION.....	50
4.5 EXPERIMENTS AND DISCUSSIONS	52
4.6 CONCLUSION	63
CHAPTER 5 SHALLOW WATER DE-SCATTERING.....	65
5.1 BACKGROUND	65
5.2 UNDERWATER IMAGING MODEL	68
5.3 DE-SCATTERING	70
5.3.1 Camera-object Distance $d(x)$ Estimation.....	70
5.3.2 Depth Map Refinement by Guided Multilayer Filter	72

5.3.3 De-scattering.....	74
5.4 EXPERIMENTS.....	75
5.5 CONCLUSION.....	83
CHAPTER 6 CONCLUSIONS	84
6.1 SUMMARY	84
6.2 CONTRIBUTIONS.....	86
6.3 FUTURE WORK.....	87
BIBLIOGRAPHY	89
ACKNOWLEDGMENTS.....	101
APPENDIX A: UNDERWATER OPTICAL IMAGING SYSTEM.....	102
APPENDIX B: PUBLICATIONS.....	105

List of Tables

<i>Number</i>	<i>Page</i>
Table 2-1: Fusion quality assessment of MES and SSS sonar intensity images.....	31
Table 3-1: PSNR and SSIM values of denoised images for LLS image with different methods.....	40
Table 4-1: CPU time of dehazed images in processing Figure 4-5 and Figure 3-6.....	59
Table 4-2: Quantitative Analysis.....	64
Table 5-1: Comparative Analysis of Different De-scattering Methods (Figure 5-6).....	81
Table 5-2: Comparative Analysis of Different De-scattering Methods (Figure 5-9).....	84

List of Figures

<i>Number</i>	<i>Page</i>
Figure 1-1: The diagram shows the depth that light will penetrate in clear ocean water.....	4
Figure 1-2: NOAA basic illustration of the depth at which different color of light penetrates ocean waters. Water absorbs warm colors like reds and oranges and scatters the cooler colors (known as short wavelength light).....	5
Figure 1-3: Example of backward scatter, forward scatter and refraction.....	6
Figure 1-4: The authorised copy of the timing plot of range-gated imaging system from [83]. Reflected Image Temporal Profile (RITP) in time domain, for clear water condition with attenuation coefficient, $c=0.26/m$; absorption coefficient, $a=0.04/m$ 1. Front RITP, 2. Middle RITP, 3. Tail RITP.....	9
Figure 2-1: Curvelet transform flowchart.....	20
Figure 2-2: Maximum energy in 3×3 window.....	23
Figure 2-3: Selected maximum energy in two images.....	24
Figure 2-4: The principle of Maximum Local Energy rule.....	26
Figure 2-5: Intensity-based images. (a) MES intensity sonar image. (b) SSS intensity sonar image.....	29
Figure 2-6: Curvelet-based image denoising. (a) MES sonar image denoising. (b) SSS sonar image denoising.....	30
Figure 2-7: Curvelet-based image contrast enhancement. (a) MES sonar image enhancement. (b) SSS sonar image enhancement.....	30
Figure 2-8: The fused images of MES and SSS. (a) Wavelet transform-based fusion. (b) curvelet transform-based fusion.....	31
Figure 3-1: Controulet coefficient relationships in different scales	35
Figure 3-2: Denoised images from the LLS dataset. (a) original noisy image. (b) Wavelet hard thresholding. (c) BLS-GSM. (d) Curvelet K-sigma.	

(e) ContourletHMT. (f) denoised with the proposed method.....	39
Figure 3-3: After denoising PSNR values of different methods in 100 samples, PSNR(K-Sigma1)=25.28 dB, PSNR(K-Sigma2)=26.16 dB, PSNR(BLS-GSM)=30.01dB, PSNR(GSCE)=28.89dB, PSNR(ContourletHMT) =23.28 dB, PSNR(Proposed)=31.36 dB.....	40
Figure 4-1: Underwater optical imaging haze model.....	47
Figure 4-2: (a) s_α and its degree approximation; (b) approximation error.....	50
Figure 4-3: Underwater imaging vignetting model.....	51
Figure 4-4: Illumination of our proposed system.(a) Captured video frame; (b) After Homomorphic filtering; (c)After Dual-tree complex wavelet denoising; (d) GTB Filter Dehazing; (e) After α ACE Color Enhancement.....	54
Figure 4-5: Probability of detection map of underwater fish. (a) Fattal's model. (b) He's model. (c) Xiao's model. (d) Our proposed model.....	57
Figure 4-6: Enhanced underwater tank images. (a) Fattal's model. (b) He's model. (c) Xiao's model. (d) Our proposed model.....	59
Figure 4-7: Different models for underwater image dehazing. (a) Captured video frame; (b) Schechner; (c)Bazeille; (d) Fattal; (e) Nicholas; (f) He; (g) Ancuti; (h) Chiang; (i) Xiao; (j) GTB Filter Dehazing.....	61
Figure 4-8: Simulations of Mine Detection in our Laboratory. (a) Captured video frame; (b) Denoised by Homomorphic filter and DTC-wavelet transform; (c) Vignetting correction; (d) GTB Filter Dehazing; (e) α ACE Color Enhancement; (f) Segmentation.....	62
Figure 4-9: (a) Original degraded image; (b) Our result of artificial light correction; (c) Our result of GTBF dehazing; (d) Result of histogram correction.....	63
Figure 5-1: Views of situation in spent fuel pool at No.3 nuclear reactor of Fukushima Daiichi Nuclear Power Station. (a) Rubble near the water surface. (b) Part view of the fuel switch. (Courtesy by Tokyo Electric Power	

Company, Japan).....	67
Figure 5-2: Underwater Optical Imaging Model.....	69
Figure 5-3: RGB histogram of Underwater Images.....	71
Figure 5-4: Weighted normalized convolution domain filtering.....	74
Figure 5-5: Depth map refinement by weighted normalized convolution domain filter. (a) Input course depth image. (b) Refined depth image.....	75
Figure 5-6: Results of different De-scattering methods.....	77
Figure 5-7: Boat image de-scattering results. (a) Input image. (b) Bazeille's result. (c) Fattal's result. (d) He's result. (e) Ancuti's result. (f) Nicholas's result. (g) Lu13's result. (h) Lu14's result.....	79
Figure 5-8: Fish image de-scattering results. (a) Input image. (b) Bazeille's result. (c) Fattal's result. (d) He's result. (e) Ancuti's result. (f) Nicholas's result. (g) Lu13's result. (h) Lu14's result.....	81
Figure 5-9: Simulation results by different descattering algorithms. (a) Noise-free image. (b) Noisy image. (c) Ancuti's result. (d) Bazeille's result. (e) Chiang's result. (f) Fattal's result. (g) He's result. (h)Nicholas's result. (i) Xiao's result. (j) Lu13's result. (k) Lu14's result.....	83
Figure A-1: Concept figure of deep-sea monitoring.....	102
Figure A-2: Experimental Equipment Image.....	102
Figure A-3: Equipment Sets.....	103
Figure A-4: Interface of Underwater Image Dehazing Software.....	104

List of Acronyms

UV	Underwater Vehicles
BCE	Bayesian Contourlet Estimator
BKF	Bessel K Form
PDF	Probability Density Function
MAP	Maximum A Posteriori
AUV	Autonomous Underwater Vehicles
ROV	Remotely Operated Vehicles
USBL	Ultra Short Base Line
LBL	Long Base Line
DVL	Doppler Velocity Log
TOBI	Towed Ocean Bottom Instrument
2D FDCT	2D Fast Discrete Curvelet Transform
GSCE	Generalized Spherically Contourlet Exponential
SSIM	Structural Similarity
PSNR	Peak Signal to Noise Ratio
RMSE	Root Mean Squared Error
MSE	Mean Squared Error
LLS	Laser Light Sheet
NGMS	Anisotropic Multivariate Shrinkage
SCM	Search Classify Map
RI	Reacquire and Identify
EO	Electro Optic
ACE	Automatic Color Equalization
BF	Bilateral Filter
TBF	Trigonometric Bilateral Filter
GTBF	Guided Trigonometric Bilateral Filter

HDR	High Dynamic Range
VDP	Visual Difference Predictor
DMS	Deep-sea Mining System
MES	Multi-beam Sonar
SSS	Side-scan Sonar
ANAF	Admissible Neural Activation Function
CRT	Coefficient of Ridgelet Transform
MLE	Maximum Local Energy
HVS	Human Visual System
PDI	Polarization Difference Imaging
RITP	Reflected Image Temporal Profile
HE	Histogram Equalization
UM	Unsharp Masking

Abstract

Underwater survey systems have numerous scientific or industrial applications in the fields of geology, biology, mining, and archeology. These application fields involve various tasks such as ecological studies, environmental damage assessment, and ancient prospection. During two decades, underwater imaging systems are mainly equipped by Underwater Vehicles (UV) for surveying in water or ocean. Challenges associated with obtaining visibility of objects have been difficult to overcome due to the physical properties of the medium. In the last two decades, sonar is usually used for the detection and recognition of targets in the ocean or underwater environment. However, because of the low quality of images by sonar imaging, optical vision sensors are then used instead of it for short range identification. Optical imaging provides short-range, high-resolution visual information of the ocean floor. However, due to the light transmission's physical properties in the water medium, the optical imaged underwater images are usually performance as poor visibility. Light is highly attenuated when it travels in the ocean. Consequence, the imaged scenes result as poorly contrasted and hazy-like obstructions. The underwater imaging processing techniques are important to improve the quality of underwater images.

As mentioned before, underwater images have poor visibility because of the medium scattering and light distortion. In contrast to common photographs, underwater optical images suffer from poor visibility owing to the medium, which causes scattering, color distortion, and absorption. Large suspended particles cause scattering similar to the scattering of light in fog or turbid water that contain many suspended particles. Color distortion occurs because different wavelengths are attenuated to different degrees in water; consequently, images of ambient in the underwater environments are dominated by a bluish tone, because higher wavelengths are attenuated more quickly. Absorption of light in water substantially reduces its intensity. The random attenuation of light

causes a hazy appearance as the light backscattered by water along the line of sight considerably degrades image contrast. Especially, objects at a distance of more than 10 meters from the observation point are almost unreadable because colors are faded as characteristic wavelengths, which are filtered according to the distance traveled by light in water. So, traditional image processing methods are not suitable for processing them well.

This thesis proposes strategies and solutions to tackle the above mentioned problems of underwater survey systems. In this thesis, we contribute image pre-processing, denoising, dehazing, inhomogeneities correction, color correction and fusion technologies for underwater image quality improvement. The main content of this thesis is as follows.

First, comprehensive reviews of the current and most prominent underwater imaging systems are provided in Chapter 1. A main features and performance based classification criterion for the existing systems is presented. After that, by analyzing the challenges of the underwater imaging systems, a hardware based approach and non-hardware based approach is introduced. In this thesis, we are concerned about the image processing based technologies, which are one of the non-hardware approaches, and take most recent methods to process the low quality underwater images.

As the different sonar imaging systems applied in much equipment, such as side-scan sonar, multi-beam sonar. The different sonar acquires different images with different characteristics. Side-scan sonar acquires high quality imagery of the seafloor with very high spatial resolution but poor locational accuracy. On the contrast, multi-beam sonar obtains high precision position and underwater depth in seafloor points. In order to fully utilize all information of these two types of sonars, it is necessary to fuse the two kinds of sonar data in Chapter 2. Considering the sonar image forming principle, for the low frequency curvelet coefficients, we use the maximum local energy method to calculate the energy of two sonar images. For the

high frequency curvelet coefficients, we take absolute maximum method as a measurement. The main attributes are: firstly, the multi-resolution analysis method is well adapted the cured-singularities and point-singularities. It is useful for sonar intensity image enhancement. Secondly, maximum local energy is well performing the intensity sonar images, which can achieve perfect fusion result [42].

In Chapter 3, as analyzed the underwater laser imaging system, a Bayesian Contourlet Estimator of Bessel K Form (BCE-BKF) based denoising algorithm is proposed. We take the BCE-BKF probability density function (PDF) to model neighborhood of contourlet coefficients. After that, according to the proposed PDF model, we design a maximum a posteriori (MAP) estimator, which relies on a Bayesian statistics representation of the contourlet coefficients of noisy images. The denoised laser images have better contrast than the others. There are three obvious virtues of the proposed method. Firstly, contourlet transform decomposition prior to curvelet transform and wavelet transform by using ellipse sampling grid. Secondly, BCE-BKF model is more effective in presentation of the noisy image contourlet coefficients. Thirdly, the BCE-BKF model takes full account of the correlation between coefficients [107].

In Chapter 4, we describe a novel method to enhance underwater images by dehazing. In underwater optical imaging, absorption, scattering, and color distortion are three major issues in underwater optical imaging. Light rays traveling through water are scattered and absorbed according to their wavelength. Scattering is caused by large suspended particles that degrade optical images captured underwater. Color distortion occurs because different wavelengths are attenuated to different degrees in water; consequently, images of ambient underwater environments are dominated by a bluish tone. Our key contribution is to propose a fast image and video dehazing algorithm, to compensate the attenuation discrepancy along the propagation path, and

to take the influence of the possible presence of an artificial lighting source into consideration [108].

In Chapter 5, we describe a novel method of enhancing underwater optical images or videos using guided multilayer filter and wavelength compensation. In certain circumstances, we need to immediately monitor the underwater environment by disaster recovery support robots or other underwater survey systems. However, due to the inherent optical properties and underwater complex environment, the captured images or videos are distorted seriously. Our key contributions proposed include a novel depth and wavelength based underwater imaging model to compensate for the attenuation discrepancy along the propagation path and a fast guided multilayer filtering enhancing algorithm. The enhanced images are characterized by a reduced noised level, better exposure of the dark regions, and improved global contrast where the finest details and edges are enhanced significantly [109].

The performance of the proposed approaches and the benefits are concluded in Chapter 6. Comprehensive experiments and extensive comparison with the existing related techniques demonstrate the accuracy and effect of our proposed methods.

Chapter 1

Introduction

1.1 Background

Seafloor exploration is an important activity that started thousands of years ago with human shallow diving [1]. In recent days, underwater surveys have numerous scientific applications in the field of geology [2], biology [3] and archeology [4].

Because of human limitations of extreme deep, during long periods of time, underwater surveys are mainly carried out by underwater vehicles (UVs). Generally, UVs can be mainly divided by equipment into two folds: one is Autonomous Underwater Vehicles (AUVs) [5] which are moved by set route, and the other is Remotely Operated Vehicles (ROVs) [6] which are manually controlled by a pilot. These vehicles are often equipped with advanced navigation sensors for monitoring the sea floor or seabed. Typical sensor suites may include an Ultra Short Base Line (USBL) [7], a Long Base Line (LBL) [8], a Doppler Velocity Log (DVL) [9], accelerometers, inclinometers, acoustic imaging sensors and optical imaging sensors, and other physical sensors and chemistry sensors.

Among the sensors listed above, acoustic imaging sensors and optical imaging sensors provide an important role in underwater vision. Underwater acoustics and optics may look like to be unrelated. However, many of available techniques show that acoustic and light is the very suitable ways to monitoring of the status of the underwater environment.

As we all known, sound is formatted as wave that propagates best in water than the others. Generally, in turbid ocean, many types of electromagnetic waves, like light, short radio waves, are used below to detect the underwater status after hundreds or thousands of meters, on the other hand, the sound can perform very well in ocean.

Animals (cetaceans, certain turtle et al.) have evolved high performance sonars to use the propagation characteristics of sound in water. On the 1490s, Leonardo da Vinci had built rudimentary passive sonar [10]. It has been proven that humans can easily learn to discriminate between different objects by using frequency transposed sound from dolphin mimicking sonars [11]. Therefore, it is not doubt that takes a more advanced technology, such as acoustic waves, which have been used for a variety of purposes, from passive usage in warfare to acoustic cameras that produce underwater pictures.

However, for short range imaging, people always need to use the optical imaging technologies. The manifest advantages of optical imaging are that, we usually taking the most developed sense, the visual perception. Compared with ocean acoustics, the colors, or shapes et al. in optical images are perceived in a common way, while the interpretation of acoustic images can sometimes be confusing and even distortion at sometimes [12]. In the next subsection, we introduce the history and development of underwater imaging systems.

1.2 Underwater Imaging Systems

1.2.1 Acoustic Imaging

As mentioned before, sound can be used to produce a map of reflected intensities, which is called sonogram. These sonar images are often similar to optical images, and the level of details higher than the traditional ways. However, if the deployed forms/types of the environment, the sonogram can be completely confused. So, people should take significant experience before interpret the information correctly [13].

Sonograms are made by the devices which emit beam pulses toward the bottom of the ocean. The sonar beams are narrow in one direction and wide in the other direction, emitted down from the transducer to the objects. The intensities of the acoustic reflection from the seafloor are called “fan-shaped”, which likes an image. As the beam is moved, the reflections will depict a series of image lines perpendicular to the direction of motion. When stitched together “along track”, the beam-lines will produced a single image of the seabed or objects [13].

It is necessary that the movement can be gained by rotation of the transducer array, just like in sector scanning sonars (SSS) for remotely operated vehicle (ROV), where they are used as navigational aids, such as conventional ship-radars. However, the equipment is towed on a cable behind the ship, and because of the lines imaged is perpendicular to the length axis of ship.

In the 1970s, the long range GLORIA side-scan sonar was developed. It was used to monitor the large oceanic areas, operated at low frequencies (6 kHz) and was used to produce images of continental shelves world-wide [14]. Recently, the 30 kHz Towed Ocean Bottom Instrument (TOBI) multisensor is used instead of it. To reach a higher resolution of the sonar image, it is possible to either increase the frequency or to increase the number of elements of the transducer array [15]. On the other hand, signal processing techniques are used for improving its performance.

About 50 years ago, there have been a lot of people who attempt to design an acoustic-optical camera. The first successful set was the EWATS system, which was created in the 1970s and had 200 lines of resolution and maximum of 10 meters range. In the 2000s, DIDSON [16], Echoscope [17], BlueView [18] or the other acoustic camera are designed for serving the underwater.

While the above mentioned acoustic imaging cameras perform well, they also have the challenges in the measurement of the seafloor or objects. In order to monitor and survey small-scale bed objects in the ocean, coastal, river, the issue of increase the accuracy and resolution of imaging sonars is also remaining. Another issue is to reduce the cost of multi-beam sonar (MBS), so as to facilitate a wider application of the technique.

1.2.2 Optical Imaging

Optical imaging sensors can provide much information updated at high speed and they are commonly used in many terrestrial and air robotic application. However, because of the interaction between electromagnetic waves and water, optical imaging systems and vision systems need to be specifically designed to be able to use in underwater

environment [19].

Underwater images have specific characteristics that should be considered during the gathering process and processing process. Light attenuation, scattering, non-uniform lighting, shadows, color filtering, suspended particles or abundance of marine life on top or surrounding the target of interest are frequently found in typical underwater scenes [103].

One effect of the inherent optical properties (IOP) of ocean is that it becomes darker and darker with the deepening water depth. As the water depth increases, the white light from the sun is absorbed and scattered. For example, in the clean ocean water, the euphotic depth is 200 meters or less [20]. In addition, the spectral composition of sunlight also changes with the water depth. Absorption is greater for long wavelengths (red color) than for short (green color); this is a prominent effect even at shallow depth with 10 meters. Therefore, most of underwater images taken in natural light (sunlight) will appear blue or green on images or videos. Thus, for all but the most deep-sea or turbidly water application, additional illumination is required. Figure 1-1 and Figure 1-2 show the light absorption process in water.

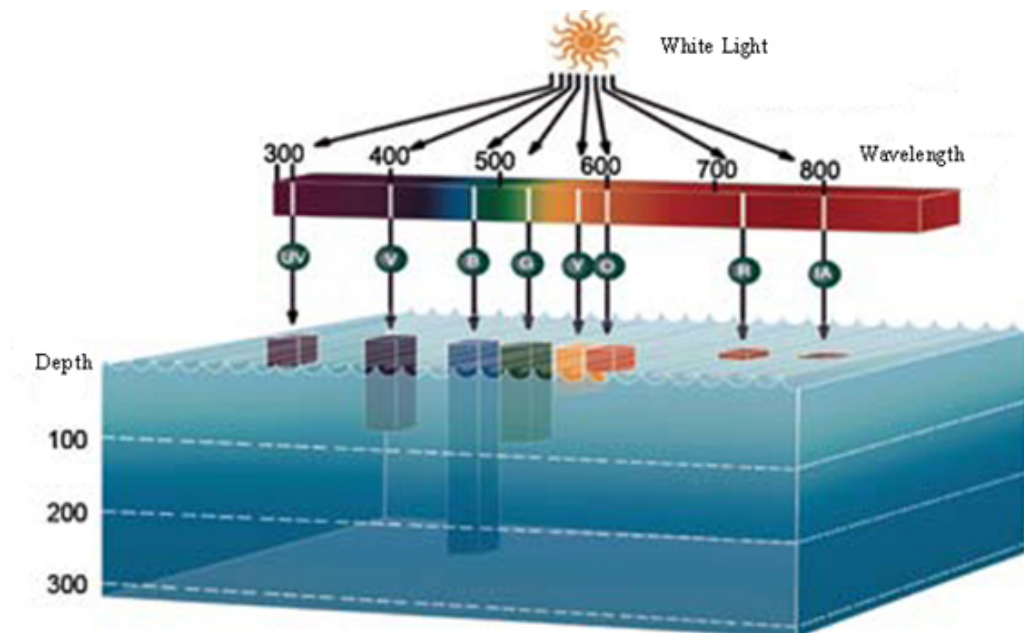


Figure 1-1: The diagram shows the depth that light will penetrate in clear ocean water.

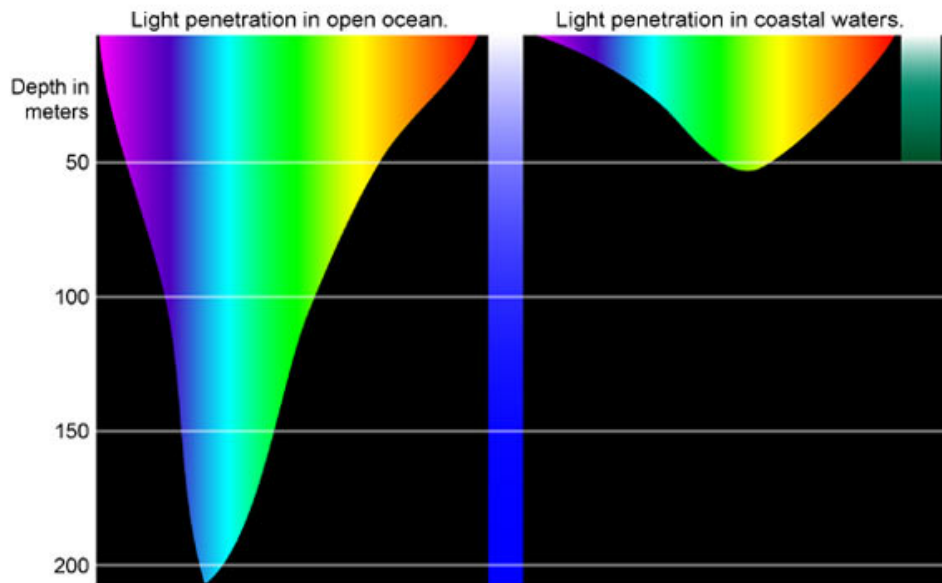


Figure 1-2: NOAA basic illustration of the depth at which different color of light penetrates ocean waters. Water absorbs warm colors like reds and oranges (known as long wavelength light) and scatters the cooler colors (known as short wavelength light).

The underwater imaging process is that, underwater optical cameras are usually equipped in watertight enclosures (also named as water housing) with a depth rated lens. Before reaching the scene of the underwater optical camera, the refraction is caused. The image is bent as the light rays coming the scene and they pass from water to glass and then from glass to air. The refraction changes the apparent shape and position of objects [21,103].

When the light (or a photon) hits a particle suspended in water, its original path is deflected by the water. According on the angle of impurities, the light ray is deviated; this phenomenon is called as forward scattering or backscattering. Forward scatter always occurred as the angle of deflection is small. Forward scatter results in image blurring and contrast reduction. Backscatter occurs when the light from the light source, which is reflected to the camera before reaching the object. Backscatter may cause bright points in the image usually known as marine snow [103]. The main issue of

backscatter also named as light veiling. It can highly reduce the image contrast, causing serious problems in underwater optical imaging systems. The referred effects of backscatter, forward scatter and refraction are illustrated in Figure 1-3.

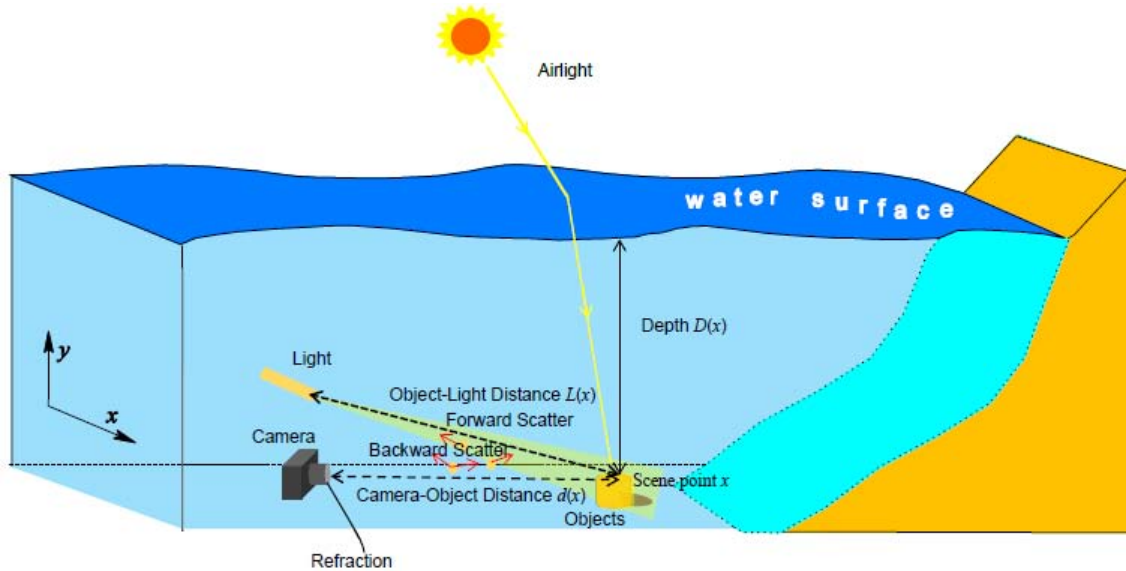


Figure 1-3: Example of backward scatter, forward scatter and refraction.

Both forward scatter and backward scatter are depending on the scope of illuminated water inside the camera's field of view. The absorption is caused by the electromagnetic waves traversing water to be quickly attenuated. Furthermore, the spectral components of light are absorbed quickly as traveling in the water. Therefore, long wavelength (red band light) is lost at first in clean water. However, in turbid water or in places with high concentration of plankton, red light may be better transmitted than blue light. Consequence, two problems are noticed that may be important problems for optical imaging and computer vision processing systems. Firstly, the usage of artificial light is needed in most cases and dramatically limits the distance at which objects are perceived. Secondly, the colors are distorted and the perception of the scene can be altered [103].

For underwater optical imaging system design, the better solution is to separate the illumination sources and the underwater optical camera. Consequence, the backscattered light must be separate from the observer as much as possible. In general, light source is separated from the camera as much as possible by other small underwater equipment

(about 3 to 5 meters). Another approach is to reduce the effect of backscatter by using gated viewing technology. In this way, it is used to emit a short pulse of light; meanwhile, the camera is opened only when the light pulse passes the desired viewing distance. Therefore, the backscatter effect from the turbidity is not showed on the image. The third approach is to increase visibility is to take polarized filters, cross polarized between the illumination and the underwater camera.

1.3 Challenges of Underwater Imaging Systems

As mentioned before, the main challenge working with the results of underwater imaging system from both rapid decay of signals of absorption, which leads to poor signal to noise feedbacks, and blurring caused by strong scattering by the water itself and constituents within, epically particulates. To properly address these issues, knowledge of underwater optical properties and their relationship to the image formation can be exploited in order to restore the imagery to the best possible level [22].

The processing of improving a degraded image to visibly look better is called image enhancement or image quality improvement [23]. It is explained that, due to the effects of optical or acoustic backscatter, the images in a scattering medium have low contrast. By improving the image contrast, it is expected to increase the visibility and discern more details. There are different definitions of measuring image contrast. One of the common definitions for image contrast c is the Michelson formula [24]:

$$c = \frac{I_{\max} - I_{\min}}{I_{\max} + I_{\min}}, \quad (1.1)$$

where I_{\max} and I_{\min} are for the maximum and minimum image intensity values respectively.

There are many different techniques to improve the contrast of the image. These techniques can be classified in to two approaches: hardware based methods and non-hardware base approach.

1.3.1 Hardware Based Approach

Hardware based approach requires special equipment; two common examples include polarization and range-gated imaging.

- **Polarization**

Light has three properties, that is, intensity, wavelength, and polarization. The human vision system and some animals can detect polarization and use it in many different ways such as enhancing visibility [25]. Natural light is initially unpolarized. However, light reaching to a camera often has biased polarization due to scattering and refraction. Light polarization conveys different information of the scene. Inspired by animal polarization vision, a polarization imaging technique has been developed. To collect light polarization data, polarization sensitive imaging and sensing systems are required [26].

Preliminary studies showed that the back-scatter light can be reduced by polarization. Some studies assume the reflected light from the object is significantly polarized rather than the back scatter and in some other studies the contrary is assumed. Also, in some studies active illumination, a polarized light source is used [27], whereas in other study passive illumination, ambient light is used for imaging. Polarization difference imaging (PDI) method process the intensity of two images obtained at two orthogonal polarizations. Schechner et al introduced a method which is based on the physical model of visibility degradations to recover underwater images using raw images through different states of polarizing filter. In this method visibility can be restored significantly, but remains some noise due to pixels falling on distant objects. A technique is developed to reduce the noise [28]. This method is developed to capture images faster, and as a result may be able to estimate a rough 3D scene structure [29].

- **Range-gated Imaging**

Range-gated or time-gated imaging is one of the hardware methods to improve the image quality and visibility in turbid conditions [30]. In range-gated underwater imaging system, the camera is adjacent to the light source, while the underwater target

is behind the scattering medium [31]. The operation of range-gated system is to select the reflected light from the object that arrives at the camera and to block the optical back-scatter light [32].

Range-gated system includes a broad-beam pulse as the illumination source, a high speed gated camera and a synchronization gate duration control [32]. Tan et al [31] presented a sample plot of the timing of range-gated imaging in their work. The authorized copy of the plot is shown in Figure 1-4.

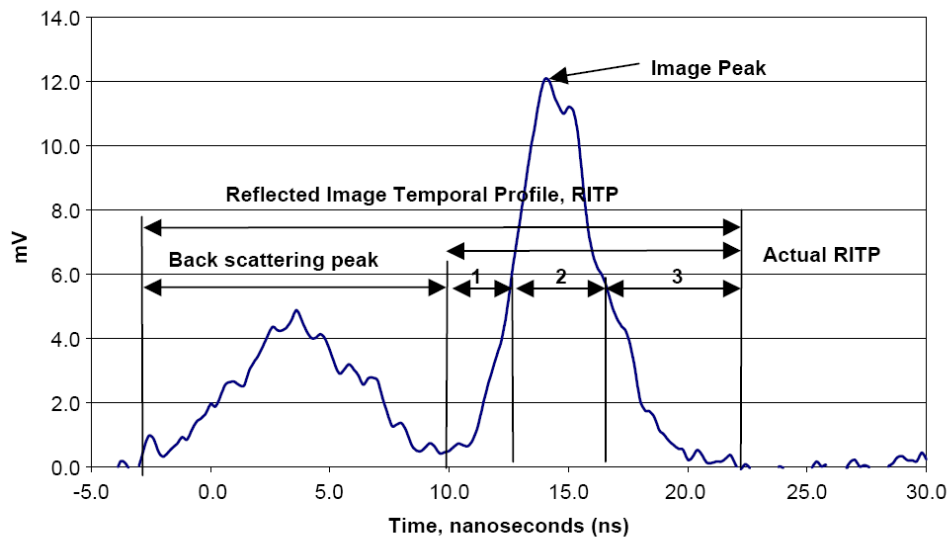


Figure 1-4: The authorized copy of the timing plot of range-gated imaging system from [31]. Reflected Image Temporal Profile (RITP) in time domain, for clear water condition with attenuation coefficient, $c=0.26/\text{m}$; absorption coefficient, $a=0.04/\text{m}$ 1. Front RITP, 2. Middle RITP, 3. Tail RITP.

A range-gated process starts when the laser sends a pulse onto the object. As the light travels, the camera gate is closed. Thus, back-scattered light will not be captured. The fast electronic shutter of the gated camera is time delayed and only opens for a very short period of time. When the laser pulse returns to the camera after hitting the object,

the camera gate opens. In this case, the camera is exposed only to the reflected light from the object. Once the laser pulse is over, the camera gate closes again. The opening or closing of the camera gate is based on the prior information about the object location [30].

1.3.2 Non-hardware Based Approach

In non-hardware based approach, no special imaging equipment is required and only digital image processing tools are utilized. Three common examples include histogram equalization, statistical modeling and unsharp masking.

● Histogram Equalization (HE)

Histogram equalization is the most common enhancement method for underwater image processing because of its simplicity and effectiveness. The operation of HE is to redistribute the probabilities of gray levels occurrences in such a way that the histogram of the output image to be close to the uniform distribution. Histogram equalization does not consider the content of an image, only the gray level distribution.

Different histogram equalization methods have been developed in recent years. These methods can be generally divided into two categories: global and local methods. Global histogram equalization processes the histogram of the whole image. Although it is effective, it has some limitations. Global HE stretches the contrast over the whole image, and sometimes this causes loss of information in dark regions. To overcome this limitation, a local HE technique was developed. Local HE uses a small window that slides sequentially through every pixel of the image. Only blocks of the image that fall in this window are processed for HE and the gray level mapping is done for the center pixel of that window. Local HE is more powerful, but requires more computation. Local HE sometimes causes over enhancement in some parts of the image, and also increases the image noise. Some methods are developed to speed up the computation, such as partially overlapped histogram equalization and block based binomial filter histogram equalization.

- **Statistical Modelling**

Oakley and Bu [33] introduce a statistical based algorithm, which using the standard deviation of the normalized brightness of an image to detect the presence of optical back scatter in a degraded image. It is assumed that the level of the optical back-scatter is constant throughout the image. This algorithm intends to find the minimum of a global cost function.

The proposed algorithm for optical backscatter estimation is to find the minimum value of a cost function that is a scaled version of the standard deviation of the normalized intensity. The key feature of this method is that it does not require any segmentation as it uses a global statistic rather than the sample standard deviation of small blocks.

The enhanced version of an image has the form:

$$\hat{I} = m(I - b) \quad (1.2)$$

where I is the degraded image, b is an estimate of the optical back-scatter contributed part of the image, \hat{I} is the modified image and m is the scaling parameter. The estimated value of optical back-scatter has been shown:

$$\arg \min \{S(b)\} \quad (1.3)$$

where

$$S(b) = \frac{1}{P} \sum_{p=1}^P \left(\frac{I_p - \bar{I}_p}{\bar{I}_p - b} \right)^2 GM \left\{ (\bar{I}_p - b) : p = 1, 2, \dots, P \right\} \quad (1.4)$$

p is the pixel position, P is the total number of pixels, I is the degraded image, \bar{I} is the smoothed image, which is calculated by reclusive Guassian filter.

- **Unsharp Masking (UM)**

Unsharp masking (UM) is the other common image enhancement method [34]. In this method the image is improved by emphasizing the high frequency components in the image [35].

The UM method is derived from an earlier photographic technique and involves subtracting the blurred version of an image from the image itself [35]. This is equivalent to adding a scaled high-pass filtered version of the image to itself [36] as shown in Eq. (1.5). The high pass filtering is usually done with a Laplacian operator [37].

$$y(m, n) = x(m, n) + \hat{\lambda}z(m, n) \quad (1.5)$$

where $x(m, n)$ is the original image, $\hat{\lambda}$ is a constant, greater than 0, that changes the grade of sharpness as desired and $z(m, n)$ is the high-pass filtered version of the original image.

Although this method is easy to implement, it is very sensitive to noise and also causes digitizing effects and blocking artifacts. Different methods of UM have been introduced to mitigate these problems. Non-linear filters, such as polynomial and quadratic filters are used instead of the high pass filter.

1.4 Outline of the Approaches

The underwater images that we are interested on may be suffered of some of the following issues: non-uniform lighting, limited range visibility, low contrast, blurring, bright artifacts, color diminished, noise et al. Therefore, application of standard or traditional computer vision techniques to improve the underwater images cannot resolve the above mentioned problems well.

The computer vision techniques can be divided by three different points of view: as an image restoration technique, as an image enhancement method [38], and as a hybrid image restoration or enhancement method.

- The image restoration method attempts to recover a degraded image by a degradation model. It is essentially known as an inverse problem. These methods

are strictly but they require a lot of model parameters (like attenuation and diffusion coefficients that characterize the water turbidity) which are only nearly known in tables and can be extremely variable. Another important parameter required is the depth estimation of a given object in the scene [19].

- Image enhancement method uses qualitative subjective criteria to produce a more pleasing image. These methods do not rely on any physical model of the image formation. These kinds of approaches are usually simpler and faster than restoration methods or restoration models. However, the processed results are not satisfied at sometimes [19].
- Combine the advantages of image restoration method and image enhancement method, we named as hybrid image restoration method. It takes the physical model to recover the scene, for recovered scene, we take the image enhancement techniques to enhance image display appearance.

In the follows we give these methods in details. Chapter 2 and Chapter 4 use image enhancement techniques. In Chapter 3 and Chapter 5, we introduce the hybrid image restoration techniques.

1.5 Contributions

The main contributions of this thesis can be summarized as follows:

- A statistical speckle suppression method for removing underwater laser image noise, based on the decomposed contourlet coefficients. This method utilizes Bayesian contourlet Estimator of Bessel K Form probability density function to model neighborhood contourlet coefficient. After that, according to the proposed PDF model, we design a maximum a posteriori estimator, which relies on a Bayesian statistics representation for the contourlet coefficients [39].
- A novel method to enhance underwater optical images by guided trigonometric bilateral filters and color correction is proposed. Our key contributions are proposed a new underwater model to compensate the attenuation discrepancy along the

propagation path, and to propose a fast guided trigonometric bilateral filtering enhancing algorithm and a novel fast automatic color enhancement algorithm [40].

- We introduce a signal frame-based vignette removal method. Given the fact that we are interested in the overall effect of light attenuation through the imaging system and not all of the image formation details, the multiscale circle gradient de-vignetting method are proposed [41].
- A novel system for removing underwater sonar image noise, enhancing the structure of sonar images, and fusing the underwater sensed images, based on the decomposed curvelet coefficients is proposed [42].
- A wavelength compensation based shallow water scene reconstruction method is proposed. Meanwhile, a novel underwater imaging model to compensate for the attenuation discrepancy along the propagation path and a fast guided multilayer filtering enhancing algorithm.

1.6 Thesis Structure

The thesis is divided into the following chapters:

Chapter 1 briefly reviews the characteristics and types of acoustic imaging and optical imaging technologies in the ocean. We also introduce the usually used underwater image formation model, and the problems of recent underwater imaging system.

Chapter 2 describes a novel system for removing underwater sonar image noise, enhancing the structure of sonar images, and fusing the underwater sensed images, based on the decomposed curvelet coefficients. Side-scan sonar acquires high quality imagery of the seafloor with very high spatial resolution but poor locational accuracy. However, multi-beam sonar obtains high precision position and underwater depth in seafloor points. In order to fully utilize all information of these two types of sonars, it is necessary to fuse the two kinds of sonar data. This paper gives curvelet transform for enhancing the signals or details in different scales separately. It also proposes a new intensity sonar image fusion method, which is based on curvelet transform. Considering

the sonar image forming principle, for the low frequency curvelet coefficients, we utilize the maximum local energy method to calculate the energy of two sonar images. For the high frequency curvelet coefficients, we take absolute maximum method as a measurement. The main attribute of this paper is: Firstly, the multi-resolution analysis method is well adapted the cured-singularities and point-singularities. It is useful for sonar intensity image enhancement. Secondly, maximum local energy is well performing the intensity sonar images, which can achieve perfect fusion result [42].

Chapter 3 describes a statistical speckle suppression method for removing underwater optical image noise, based on the decomposed contourlet coefficients. This method utilizes Bayesian Contourlet Estimator of Bessel K Form (BCE-BKF) probability density function (PDF) to model neighborhood contourlet coefficients. After that, according to the proposed PDF model, we design a maximum a posteriori (MAP) estimator, which relies on a Bayesian statistics representation for the contourlet coefficients of noisy images. There are three obvious virtues of this method. Firstly, contourlet transform decomposition prior to curvelet transform and wavelet transform by using ellipse sampling grid. Secondly, BCE-BKF model is more effective in presentation of the noisy image contourlet coefficients. Thirdly, the BCE-BKF model takes full account of the correlation between coefficients. Some comparisons with the best available results will be present in order to illustrate the effectiveness of the proposed method [107].

Chapter 4 presents to utilize the image processing technologies to determine the mineral location and to recognize the mineral actually within a little processing time. We firstly analysis the recent underwater imaging models, and propose a novel underwater optical imaging model, which is much closer to the light propagation model in the underwater environment. In our imaging system, we remove the electrical noise by dual-tree complex wavelet transform. Then, solving the non-uniform illumination of artificial lights by fast guided trilateral bilateral filter and recovering the image color through automatic color equalization. Finally, a shape-based mineral recognition algorithm is proposed for underwater objects detection [108].

Chapter 5 describes a novel method of enhancing underwater optical images or videos using guided multilayer filter and color correction. In certain circumstances, we need to immediately monitor the underwater environment by disaster recovery support robots. However, due to the inherent optical properties and underwater complex environment, the captured images or videos are distorted seriously. That is, absorption, scattering and color distortion are three major distortion issues for underwater optical imaging. Our key contributions proposed include a novel underwater imaging model to compensate for the attenuation discrepancy along the propagation path and a fast guided multilayer filtering enhancing algorithm.

Chapter 6 presents the conclusions of this work, summarizes the contributions and identifies some future research directions.

Chapter 2

Multi-Source Images Fusion

2.1 Background

Acoustic sensing is the imaging modality of choice for the analysis of deep-sea environments [43]. Acoustic waves propagate well in water, as opposed to electro-magnetic waves, which is used by optical cameras to reconstruct the real scene. The optical camera performs high resolution images and can exploit rich vision literature applied in air; however, it has the drawbacks of the limited range of light in water and may be having no-ideal conditions in the turbidity of the water. So, several acoustic sensors are routinely used to study the underwater environment, such as multi-beam sonar [44], side-scan sonar [45] et al.

Multi-beam sonar (MES) can obtain high precision position and ocean depth in seafloor. At the same time, it also can obtain low-resolution seabed images. To obtain images of the seafloor, side-scan sonar (SSS) are used. It can obtain low precision position and depth with high-resolution. To take full advantages of all the information, the digital information of MES and SSS can be fused for explaining and exploring seabed. The fused image is useful to make more comprehensive, quantitative and qualitative analysis, which is of great contribution to known seafloor topography, underwater target detection and so on.

Because the images of MES and SSS are not measured from the same sensor, their deformations are also not at the same. It is necessary or important to combine the two type sonar images in order to obtain the converted parameters of related pixels. T.P. Lebas et al [46] used Chamfer registration method to acquire MES sonar image and the SSS sonar image. It did not consider whole image, and may be caused the registration

parameters inconsistent in the part of image mosaic. K.P. Behrooz et al [47] proposed the seabed contour method to co-register images. The result was satisfactory, but the results must be obtained from the same sensor. In 1998, S. Daniel et al [48] suggested to use goals and shadows of the same place to register images. This method is only applicable to the slant range uncorrected SSS image. In the same year, Z.X. Zhang [49] adopted a fast automatic registration method for co-registration of remote sensing imagery. However, the method is not suitable for sonar image processing. In 2003, F.L. Yang et al [50] proposed the maximal correlate coefficient-based co-registering method. The method can fully consider useful information of MES and SSS sonars. In this chapter, we take this method as an image preprocessing method.

In Ref. [51], Y. Han et al proposed a wavelet transform based MES and SSS sonar image fusion method. It adapted dyadic wavelet transform for fusion. During some research, people found that the wavelet only can express point singularities very well. In 2 dimensional or higher dimensional signal, because of limited directional of filter banks, the wavelet is unsuitable to express the signal information. To this end, several theoretical papers have called attention to the benefits of beyond wavelets.

Curvelet [52], as a new multiscale analysis method in beyond wavelets, which is an extension and latest development of Wavelet and Ridgelet, is a kind of multiscale, multi-directional and anisotropic transform. This paper proposes curvelet transform in sonar image denoising, enhance the sonar image's global contrast in the low frequency sub-bands, and enhance the details of image at each scale in the high frequency. After that, an intensity-based curvelet transform fusion method is proposed.

2.2 Sonar Image Pre-processing

In this section, we will briefly recall the theory of ridgelet and curvelet transforms, which is used in this thesis [42, 54].

Definition: let $\psi : R \rightarrow R$ satisfy the following condition,

$$K_\psi = \int \frac{|\hat{\psi}(\xi)|^2}{|\xi|^d} d\xi < \infty. \quad (2.1)$$

where ψ is called an Admissible Neural Activation Function (ANAF). We will suppose that ψ is normalized so that $K_\psi = 1$.

For each $a > 0$, $b \in \mathbb{R}$ and $\theta \in [0, 2\pi]$ ridgelet basis functions are defined by

$$\psi_{a,b,\theta} = a^{-1/2} \psi \left(\frac{x_1 \cos \theta + x_2 \sin \theta - b}{a} \right) \quad (2.2)$$

We can see that ridgelet function is a constant in the direction of line: $x \cos \theta + x \sin \theta = C$. In the vertical direction of the line, it is a wavelet function. Given an integrable bivariate function $f(x_1, x_2)$, we define its ridgelet coefficients (*i.e.* Continuous Ridgelet Transform) by,

$$\text{CRT}_f(a, b, \theta) = \int_{-\infty}^{\infty} \int_{-\infty}^{\infty} \psi_{a,b,\theta}(x_1, x_2) f(x_1, x_2) dx_1 dx_2 \quad (2.3)$$

Then the exact reconstruction formula is

$$f(x_1, x_2) = \int_0^{2\pi} \int_{-\infty}^{\infty} \int_0^{\infty} \text{CRT}_f(a, b, \theta) \psi_{a,b,\theta}(x_1, x_2) \frac{da}{a^3} db \left(\frac{d\theta}{4\pi} \right) \quad (2.4)$$

where a and b are selected for the functions which are both integrable and square integrable. A basic tool for calculating ridgelet coefficients is to view ridgelet analysis as a form of wavelet analysis in the Radon domain. The Radon transform for function $f(x_1, x_2)$ is given by,

$$R_f(\theta, t) = \int_{-\infty}^{\infty} \int_{-\infty}^{\infty} f(x_1, x_2) \delta(x_1 \cos \theta + x_2 \sin \theta - t) dx_1 dx_2 \quad (2.5)$$

where δ is the Dirac function. The ridgelet coefficients $\text{CRT}_f(a, b, \theta)$ of function $f(x_1, x_2)$ are given by analysis of the Radon transform by

$$\text{CRT}_f(a, b, \theta) = \int_{-\infty}^{\infty} R_f(\theta, t) a^{-1/2} \psi[(t - b)/a] dt \quad (2.6)$$

Hence, we clearly see that the ridgelet transform is precisely the application of one-dimensional wavelet transform to the slices of the Radon transform where the angular variable θ is constant and t is varying. Through discrete Radon transform, we

can turn an array of $n \times n$ to that of $n \times 2n$. And then one-dimensional wavelet transform is done, and $2n \times 2n$ array discrete ridgelet transform is gotten [54]. The flowchart of ridgelet transform is presented in Figure 4-1.

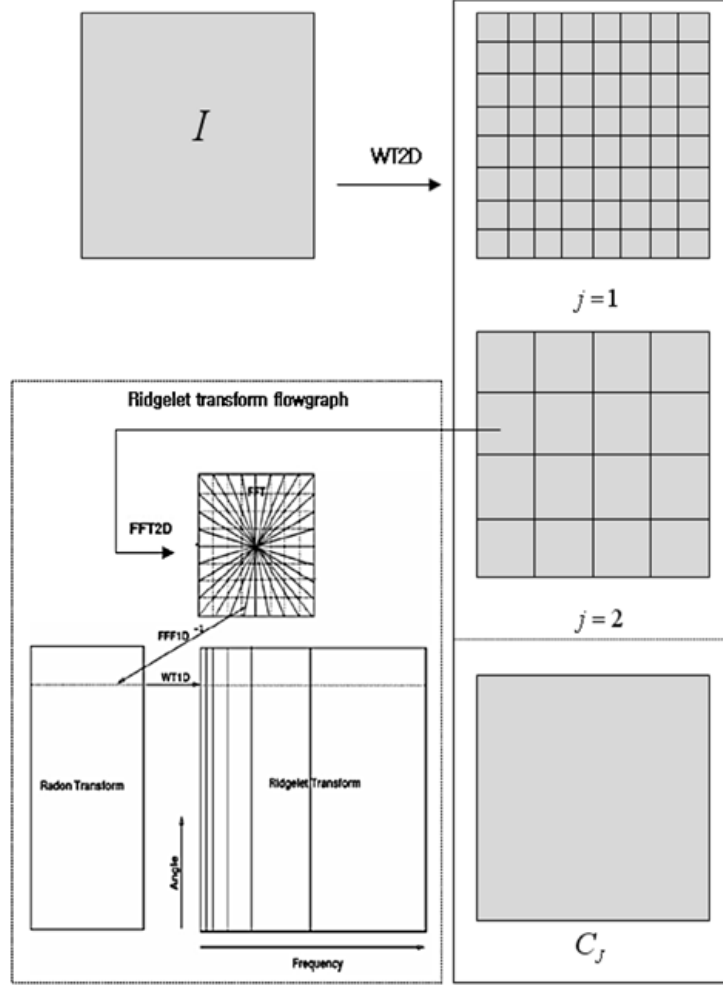


Figure 2-1: Curvelet transform flowchart.

Curvelet transform [53, 54] provides a sparse expression for image smoothing and edge section at the same time. Unlike the results in wavelet transform, the coefficient of the edge can be concentrated. Let Q_s be the collection of all dyadic squares of scale s and it can be defined by

$$Q_s = \left[\frac{k_1}{2^s}, \frac{k_1+1}{2^s} \right] \times \left[\frac{k_2}{2^s}, \frac{k_2+1}{2^s} \right] \quad (2.7)$$

where $k_1, k_2 \in \mathbb{Z}$. For $Q \in Q_s$, let w_Q be a window near to Q , obtained by dilation and translation of a single w , and is satisfied

$$\sum_{Q \in Q_s} w_Q^2(x_1, x_2) = 1 \quad (2.8)$$

After that, we have the reconstruction formula as

$$\begin{aligned} f(x_1, x_2) &= \sum_{Q \in Q_s} f(x_1, x_2) w_Q^2(x_1, x_2) \\ &= \sum_{Q \in Q_s} \int_0^{2\pi} \int_{-\infty}^{\infty} \int_0^{\infty} \langle f, w_Q T_Q \psi_{a,b,\theta} \rangle_{L^2(\mathbb{R}^2)} \\ &\quad \times w_Q(x_1, x_2) T_Q \psi_{a,b,\theta}(x_1, x_2) \frac{da}{a^3} db \frac{d\theta}{4\pi} \end{aligned} \quad (2.9)$$

We now briefly report the 2D Fast Discrete Curvelet Transform (2D FDCT) [55] as a soft thresholding sonar image denoising method in this paper. 2D FDCT via wrapping is simpler, faster, and less redundant. The 2D FDCT is expressed as

$$c^D(j, l, k) = \sum_{0 > t_1, t_2 < n} f[t_1, t_2] \bar{\varphi}_{j,l,k}^D[t_1, t_2] \quad (2.10)$$

where $f[t_1, t_2]$ is an input of Cartesian arrays with $t_1 \geq 0, t_2 < n$. $c^D(j, l, k)$ are curvelet coefficients and $\varphi_{j,l,k}^D$ are Riesz representers. $l = 0, 1, \dots, 2^j$, $k = (k_1, k_2)$, $k_1, k_2 \in \mathbb{Z}$ is a translation parameter. $j = 0, 1, 2, \dots$ is a scale parameter.

Since the 2D FDCT is not normpreserving, the variance of each curvelet coefficient depends on its index, Let C denote the 2D FDCT matrix and curvelet transform an image with noise distribution given by $N(0,1)$, then the outcome has noise distribution given by $N(0, CC^*)$. After that, use the Monte-Carlo simulation method to estimate the noise variance of each curvelet index. Suppose an image I with standard with noise, $N(0,1)$ is discrete curvelet transform. The variance, $\tilde{\sigma}_\lambda^2$ is estimated where λ indicates its index. The denoising algorithm by soft thresholding the curvelet coefficients c with

$$\tilde{c}_\lambda = \begin{cases} c_\lambda & |c_\lambda| \geq k\sigma_\lambda\sigma \\ 0 & |c_\lambda| < k\sigma_\lambda\sigma \end{cases} \quad (2.11)$$

where σ is estimation of the standard deviation of the noise of image I and k is subband dependent value, estimated by denoising few know images and letting k variate.

Because of the curvelet transform is well-adapted to represent images containing edges, it is good candidate for edge enhancement [56]. In Ref. [56], a non-linear image contrast enhancement method was proposed, which is based on modify the curvelet coefficients. This method needed c , p , s , and m , four parameters to determine Starck operator. It requires repeated adjustment parameters in practice experience. In this chapter, we introduce a new enhancement method. The curvelet coefficients at scale j and location l are multiplied by y , where y is defined by:

$$\begin{aligned} y(x) &= x_{j,l} - (G-1)\delta & \text{if } x_{j,l} < -\delta \\ y(x) &= Gx_{j,l} & \text{if } |x_{j,l}| \leq \delta \\ y(x) &= x_{j,l} + (G-1)\delta & \text{if } x_{j,l} > \delta \end{aligned} \quad (2.12)$$

where, the threshold $\delta = \max(|x_{j,l}|) \frac{e^{-j}}{1+e^{-j}}$. Gain factor $G = \frac{c}{1+e^{-j}}$, which can be adapted by c . This method only uses one parameter to determine the coefficients c .

2.3 Local Energy Fusion

2.3.1 Energy of Image

As we all know, after Fourier Transform into the frequency domain, there are high frequency and low frequency of sub-bands. Most of the energy of image concentrated in low frequency coefficients. It is greatest impact the image quality. So, how to choose the low frequency coefficients is the key to improve the image quality.

All kinds of beyond wavelet transforms are based on the geometric features of image analysis method, to achieve multi-scale and multi-directional image decomposition. This is suitable for the line singular analysis. But because these transforms contain down sampling, it is not translation invariance, leading to pseudo-Gibbs effects. In other

side, as the incomplete of the multi-scale decomposition, some details of the image are still remaining in the low frequency components. This phenomenon is obviously when the decomposition levels are less. Because of this, someone suggested that use edge-based fusion method in low frequency. Using 3 directional filtering operator, extract the edge information with spatial filters for low frequency. And then take a larger value of edge information as the fusion criterion in order to better extract the low frequency components in the direction of the information.

This thesis uses the average edge energy as a measurement for the edge region, using the edge of the criteria to select the maximum energy. Because of human visual perception characteristics of locality, the decision of fusion should consider the neighborhood.

2.3.2 Principle of Local Energy

First of all, we have an image with the size of $N \times N$. Using a widow to deal with it, the size of the window is 3×3 , as shown in Figure 2-2 [55].



Figure 2-2: Maximum Energy in 3×3 window.

We set the pixel is $(x-1, y-1)$, $(x, y-1)$, $(x+1, y-1)$, $(x-1, y)$, (x, y) , $(x+1, y)$, $(x+1, y+1)$, $(x-1, y+1)$, $(x, y+1)$, 9 pixels. The red part is (x, y) . After that, we through Local energy, and get the energy of each pixels, $E(x-1, y-1)$, $E(x, y-1)$, $E(x+1, y-1)$, $E(x-1, y)$, $E(x, y)$, $E(x+1, y)$, $E(x+1, y+1)$, $E(x-1, y+1)$, $E(x, y+1)$.

Then, we calculate the max energy by,

output = max{ $E(x-1,y-1)$, $E(x,y-1)$, $E(x+1,y-1)$, $E(x-1,y)$, $E(x,y)$, $E(x+1,y)$, $E(x+1,y+1)$, $E(x-1,y+1)$, $E(x,y+1)$ }.

And the window move ahead as the Figure 2-3.

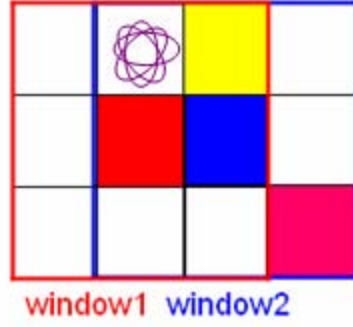


Figure 2-3: Selected maximum energy in two images.

We get $E'(x-1,y-1)$, $E'(x,y-1)$, $E'(x+1,y-1)$, $E'(x-1,y)$, $E'(x,y)$, $E'(x+1,y)$, $E'(x+1,y+1)$, $E'(x-1,y+1)$, $E'(x,y+1)$

here,

$$E'(x-1,y-1)=E(x-1,y),$$

$$E'(x,y-1)=E(x,y),$$

$$E'(x+1,y-1)=E(x+1,y),$$

$$E'(x-1,y)=E(x,y),$$

$$E'(x,y)=E(x+1,y),$$

$$E'(x,y+1)=E(x+1,y+1).$$

If the max energy is one of $E'(x+1,y+1)$, $E'(x-1,y+1)$, $E'(x,y+1)$, then output the value. Otherwise, output the max energy is one of $E'(x-1,y-1)$, $E'(x,y-1)$, $E'(x+1,y-1)$, $E'(x-1,y)$, $E'(x,y)$, $E'(x+1,y)$. Until search all pixels of the image.

2.3.3 Maximum Local Energy

Back to review the sonar camera imagery principle, the sonar or acoustic camera emits acoustic beams and returns two sets of data, the intensity of the return from a point, and the distance from the camera. Based on intensity (or energy) of receiver and imaging principle, the intensity-distance information can be imaged as gray level image.

Consider the energy distribution of the gray image. This thesis takes the maximum local energy (MLE) [57] as a measurement to fuse MES and SSS sonar images. In image multiscale analysis, due to the incompleteness of multi-scale decomposition, image details are still retained in the low frequency. Therefore, people proposed edge filters to get a good result. But because of the edge filter coefficients distribute as non-Gaussian distribution. Consequence, combine with local energy, can solve this problem very well. Select the maximum energy of two images as output. Due to the partial human visual perception characteristics and the relationship of decomposition about local correlation coefficients, the statistical characteristics of neighbor should be considered. Therefore, the statistic algorithm is based on the 3×3 sliding window [42]. The algorithm is described as follows:

$$LE_{\xi}(i, j) = \sum_{i' \in M, j' \in N} p(i+i', j+j') \bullet f_{\xi}^{(0)2}(i+i', j+j') \quad (2.13)$$

where p is the local filtering operator. M, N is the scope of local window. $\xi \in A$ or B (A, B is the window for scanning two images). $f_{\xi}^{(0)}(i, j)$ is low frequency coefficients.

Maximum Local Curvelet Energy is

$$LCE_{\xi}^{l,k}(i, j) = E_1 * f_{\xi}^{(0)2}(i, j) + E_2 * f_{\xi}^{(0)2}(i, j) + \dots + E_K * f_{\xi}^{(0)2}(i, j). \quad (2.14)$$

where E_1, E_2, \dots, E_{K-1} and E_K are the filter operators in K different directions. l is the scale layer.

$$E_1 = \begin{bmatrix} -1 & -1 & -1 \\ 2 & 2 & 2 \\ -1 & -1 & -1 \end{bmatrix}, E_2 = \begin{bmatrix} -1 & 2 & -1 \\ -1 & 2 & -1 \\ -1 & 2 & -1 \end{bmatrix}, E_3 = \begin{bmatrix} -1 & 0 & -1 \\ 0 & 4 & 0 \\ -1 & 0 & -1 \end{bmatrix} \quad (2.15)$$

$LCE_{\xi}(i,j)$ reflects the intensity information of horizontal, vertical and diagonal direction.

The principle of the Maximum Local Energy (MLE) method can be elaborated by Figure 2-4. The scale J matrix in curvelet transform domain, use Eq. (2.14) to convert the coefficients values to energy values. A sliding matrix or window, with 3 directions, is scanning through the energy matrix, and output the maximum coefficient as the fused coefficients [42].

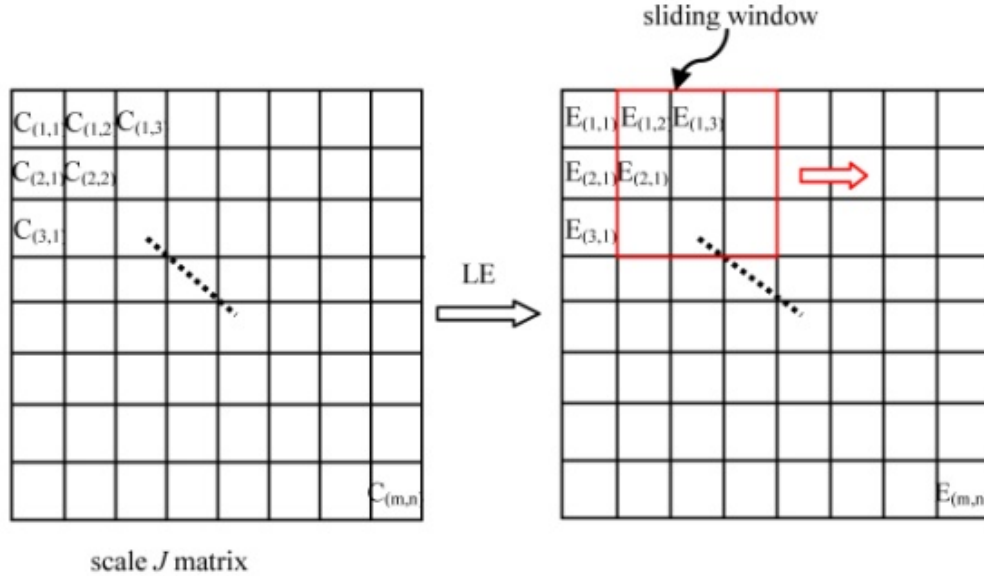


Figure 2-4: The principle of Maximum Local Energy rule.

Suppose $I_A^{l,k}(i,j)$, $I_B^{l,k}(i,j)$ and $I_F^{l,k}(i,j)$ denote the coefficients of source images and fused images. It is well represent the image details information. Define the average local energy of image A and B is

$$ALCE_{AB} = \frac{LCE_A(i,j) + LCE_B(i,j)}{2} \quad (2.16)$$

The Correlation Coefficient (CC) of the two source image is R_{AB} . Suppose the Probability Distribution Function (PDF) of $ALCE_{AB}$ is α , which is calculated by the proportion of edge pixels. If $R_{AB} < \alpha$, the low coefficient c_{low} as output. Otherwise output

the weighted coefficient $wC_{low}+(1-w)C_{high}$. The weighting factor w is set by hand. For the high frequency coefficients, we take the absolute maximum method.

2.4 Experiments and Discussions

The following data are obtained from the offshore of the *East China Sea*. MES and SSS sonar systems are both used. Figure 2-5(a) is the intensity-based seafloor terrain obtained by MES, and Figure 2-5(b) is the same area intensity-based terrain obtained by SSS. The maximal depth is 100.8 meter, and the minimal depth is 27.3 meter. The data have been preprocessing. Figure 2-6(a) is the curvelet transform-based MES image denoising and Figure 2-6(b) is the curvelet transform-based SSS image denoising. Figure 2-7(a) is the curvelet transform-based MES image contrast enhancement, and Figure 2-7(b) is the curvelet transform-based SSS image contrast enhancement. The PSNR of MES and SSS is 38.697 dB, 40.6898 dB, respectively. From this figure, the edge details are more clearly. Figure 2-8 reports the comparison of wavelet transform-based fusion and curvelet transform-base fusion. Except of the visual analysis, we also compare the results by some mathematical indexes. The quantitative analysis result is shown in Table 2-1. We use the evaluation functions in [58, 59] to measure the results. From Table 2-1, we also confirm that the curvelet transform based fusion method is obviously better than wavelet transform based fusion method.

The quality assessment of fused images is a difficult task. Fidelity assessment to the reference requires computation of several indexes. These indexes are on spectral consistency, spatial consistency or on the both together. We did some quantitative analysis, mainly from the perspective of mathematical statistics aspect and the image's statistical parameters are calculated, which include Peak Signal to Noise Ratio (PSNR), mean squared error (MSE), fusion quality index (Q), weighted fusion quality index (Q_w), edge-dependent fusion quality index (Q_E) [57].

Let x_i and y_i be the i -th pixel in the original image \mathbf{x} and the distorted image \mathbf{y} , respectively. The *MSE* and *PSNR* between the two images are given by

$$MSE = \frac{1}{N} \sum_{i=1}^N (x_i - y_i)^2 \quad (2.17)$$

$$PSNR = 10 \log_{10} \left(\frac{L^2}{MSE} \right) \quad (2.18)$$

The authors in [60] used a sliding window, from the top-left of the two images A, B . The sliding window is with a fixed size. For each window w , the local quality index $Q_0(A, B | w)$ is computed for the values $A(i, j)$ and $B(i, j)$, where pixels (i, j) lies in the sliding window w .

$$Q_0(A, B) = \frac{1}{|W|} \sum_{w \in W} Q_0(A, B | w) \quad (2.19)$$

where W is the family of all windows and $|W|$ is the cardinality of W . In practice, the Q_0 index also defined as

$$Q_0(A, B) = \frac{\sigma_{AB}}{\sigma_A \cdot \sigma_B} \cdot \frac{2\bar{A} \cdot \bar{B}}{(\bar{A})^2 + (\bar{B})^2} \cdot \frac{2\sigma_A \cdot \sigma_B}{(\sigma_A^2 + \sigma_B^2)} \quad (2.20)$$

where, σ_{AB} denotes the covariance between A and B , \bar{A} and \bar{B} are the means, σ_A^2 and σ_B^2 are the variances of A and B , respectively.

Piella et al. [60] redefined the useful quality index Q_0 as $Q(A, B, F)$ for image fusion assessment. Here A, B are two input images and F is the fused image. They denoted by $s(A|w)$ some saliency of image A in window w . This index may depend on contrast, sharpness, or entropy. The local weight $\lambda(w)$ is defined as

$$\lambda(w) = \frac{s(A | w)}{s(A | w) + s(B | w)} \quad (2.21)$$

where $s(A|w)$ and $s(B|w)$ are the local saliencies of input images A and B , $\lambda \in [0, 1]$. The fusion quality index $Q(A, B, F)$ as

$$Q(A, B, F) = \frac{1}{|W|} \sum_{w \in W} (\lambda(w) Q_0(A, F | w) + (1 - \lambda(w)) Q_0(B, F | w)) \quad (2.22)$$

They also defined the overall saliency of a window as $C(w) = \max(s(A|w), s(B|w))$. The weighted fusion quality index is then defined as

$$Q_W(A, B, F) = \sum_{w \in W} c(w) (\lambda(w) Q_0(A, F | w) + (1 - \lambda(w)) Q_0(B, F | w)) \quad (2.23)$$

where $c(w) = C(w) / (\sum_{w' \in W} C(w'))$. Using edge images A', B', F' inside of original images A, B , and F , and combine $Q_W(A, B, F)$ and $Q_W(A', B', F')$ into an edge-dependent fusion quality index by

$$Q_E(A, B, F) = Q_W(A, B, F) \cdot Q_W(A', B', F')^\alpha \quad (2.24)$$

where α is a parameter that expresses the contribution of the edge images compared to the original images.

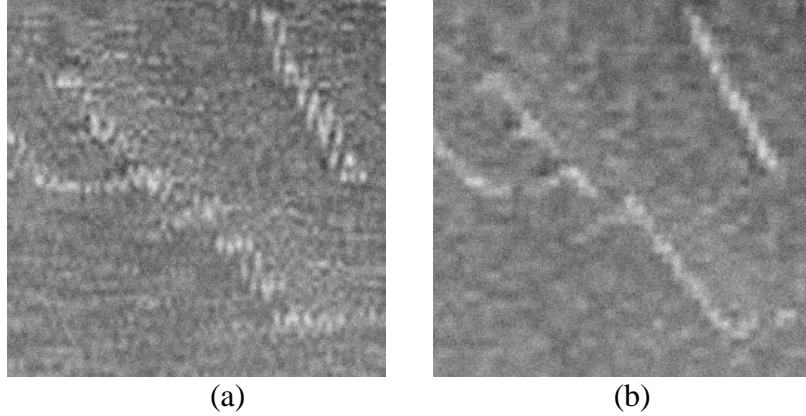


Figure 2-5: Intensity-based images. (a) MES intensity sonar image. (b) SSS intensity sonar image.

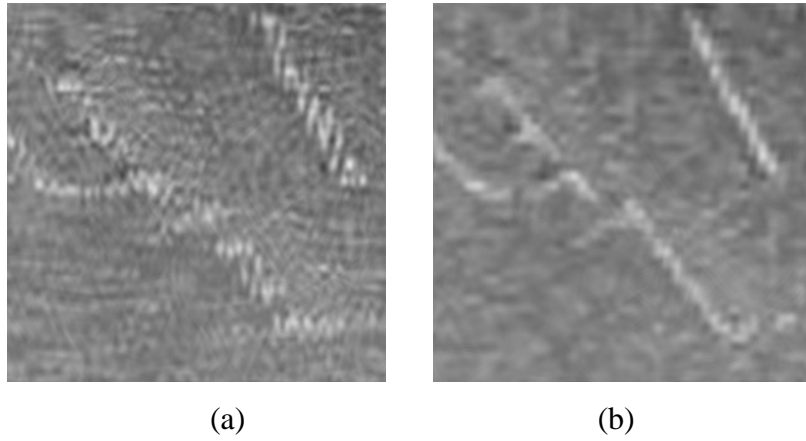


Figure 2-6: Curvelet-based image denoising. (a) MES sonar image denoising. (b) SSS sonar image denoising.

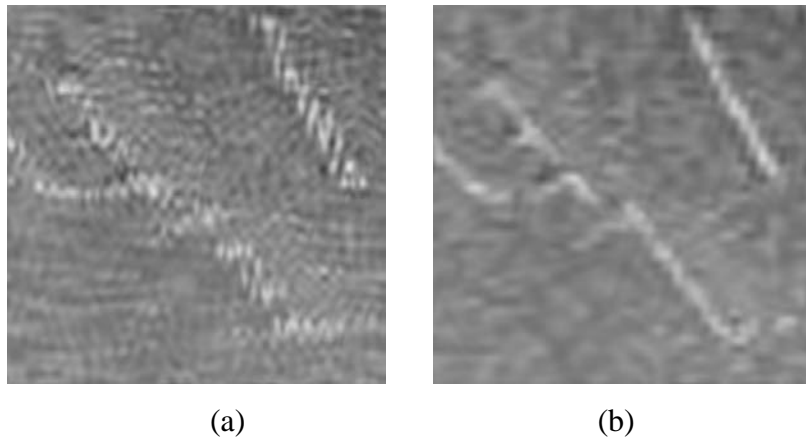


Figure 2-7: Curvelet-based image contrast enhancement. (a) MES sonar image enhancement. (b) SSS sonar image enhancement.

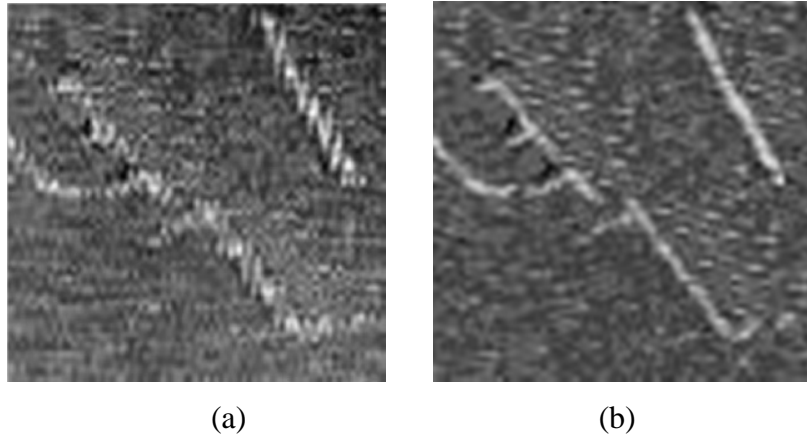


Figure 2-8: The fused images of MES and SSS. (a) wavelet transform-based fusion. (b) curvelet transform-based fusion.

Table 2-1: Fusion quality assessment of MES and SSS sonar intensity images.

	Wavelet Transform	Curvelet Transform
PSNR [dB]	28.697	30.699
Q	0.8797	0.9012
Q_w	0.9565	0.9697
Q_E	0.8399	0.9012

2.5 Conclusion

This Chapter proposed a method that combines the multi-beam water depth data (MES) and side-scan image (SSS) information, based on curvelet transform. It is firstly considered the maximum local energy method and curvelet transform for MES and SSS sensor image fusion. During the results using human visual system (HVS) and some well-defined mathematical frameworks, the proposed methods have perfect preformation on solving sonar data. The methods can be used not only in the flat seafloor that has different intensities, but also in the isotropy seabed that has an uneven terrain.

Chapter 3

Laser Images Denoising

Underwater vision or visualization is an important task for ocean engineering. Different from common images, underwater laser images are usually suffered from poor visibility because of the medium scattering and color distortion. Firstly, underwater imaging is very difficult, mostly because of the attenuation, which is caused by light that is reflected from a surface and is deflected and scattered by particles, and absorption substantially reduces the light energy [109]. In contrast to common photographs, underwater optical images suffer from poor visibility owing to the medium, which causes scattering, color distortion, and absorption. Large suspended particles cause scattering similar to the scattering of light in fog or turbid water that contain many suspended particles. Color distortion occurs because different wavelengths are attenuated to different degrees in water; consequently, images of ambient underwater environments are dominated by a bluish tone, because higher wavelengths are attenuated more quickly. Absorption of light in water substantially reduces its intensity. The random attenuation of light causes a hazy appearance as the light backscattered by water along the line of sight considerably degrades image contrast. In particular, objects at a distance of more than 10 meters from the observation point are almost indistinguishable because colors are faded as characteristic wavelengths are filtered according to the distance traveled by light in water [104].

In fact, the above drawbacks can be solved by image denoising methods in some degree. The image denoising process is one of the important approaches in image quality retrieval. Generally, the image denoising methods are roughly divided in two parts: spatial domain methods and transform domain methods. Spatial domain denoising is with the classical assumption, that is, the input noisy images are piecewise constant,

and the neighbor pixels are highly correlated. So, the spatial domain denoising is to filter the nearby pixels. The state-of-the-art methods are Gaussian Smoothing, Local Adaptive Smoothing, and Bilateral Filtering et al. On the other hand, the transform domain methods transfer the image from the spatial domain into a different domain (e.g., frequency domain, wavelet domain, ridgelet domain) and suppress noise in the transform domain. Transform domain denoising methods generally include Wiener Filtering, Shape-adaptive Discrete Cosine Transform Denoising, Wavelet Transform Denoising et al. In this chapter, we have no intention to provide a survey of the-state-of-the-art methods. Instead, we intend to concentrate a new approach on the transform domain towards the image denoising problem.

Some researches had addressed the development of statistical models of wavelet coefficients of images in recent years [61-63]. However, the major drawback for wavelets in two-dimensions or higher is their limitation of capturing directional information. To overcome this deficiency, some researchers have recently considered multiscale and directional representations that can capture the geometrical structures very well, such as, wedgelets [64], bandelets [65], curvelets [66, 67] and contourlets [68]. Using curvelet transform for decomposition, blocks must be overlapped together to avoid the boundary effect. Therefore, redundancy is higher in this implementation algorithm. In depth, the curvelet transform is based on ridgelet transform, which must use the Cartesian to polar conversion. However, the Cartesian-Polar conversion is very difficult in practice. Luckily, the contourlet transform is one of a “true” two-dimensional transform that can capture the intrinsic geometrical structure. Contourlet transform better represents the salient features of the image such as, edges, lines, curves, and contours, than wavelet transform because of its anisotropy and directionality [39].

In this Chapter, we propose a novel anisotropic multivariate shrinkage for digital image denoising. There are three obvious virtues of this method to solve the drawbacks of state-of-art methods. Firstly, contourlet transform decomposition prior to wavelet transform and curvelet transform by using more effective directional filter banks. Secondly, anisotropic multivariate shrinkage model is more consorts in considering the

relationship of contourlet coefficients. Thirdly, the proposed can remove non-Gaussian noise very well by using multivariate shrinkage method, which fully considering the coefficients relationship.

3.1 Background

3.1.1 Soft-thresholding Denoising

We now briefly report the 2D Fast Discrete Curvelet Transform (2D FDCT) as a soft thresholding sonar image denoising method in this subsection. 2D FDCT via wrapping is simpler, faster, and less redundant [67]. The 2D FDCT is expressed as

$$c^D(j, l, k) = \sum_{0 < t_1, t_2 < n} f[t_1, t_2] \bar{\varphi}_{j,l,k}^D[t_1, t_2] \quad (3.1)$$

where $f[t_1, t_2]$ is an input of Cartesian arrays with $t_1 \geq 0, t_2 < n$. $c^D(j, l, k)$ are curvelet coefficients and $\varphi_{j,l,k}^D$ are Riesz representers. $l = 0, 1, \dots, 2^j$, $k = (k_1, k_2)$, $k_1, k_2 \in \mathbb{Z}$ is a translation parameter. $j = 0, 1, 2, \dots$ is a scale parameter.

3.1.2 Generalized Spherically Contoured Exponential

In Ref. [67], the authors proposed a generalized spherically contoured exponential (GSCE) model for natural image denoising in curvelet domain. Compare with the K-Sigma shrinkage method, this method has a good performance obviously. It takes MAP parameters estimator for estimate the 8 neighbors of the coefficient, instead of using the individual coefficient magnitude. The proposed probability density function (PDF) of the GSCE is

$$p_c(c) = \alpha \cdot \exp\left(-\frac{\beta}{\sigma_c} \|c\|\right), \quad (3.2)$$

where σ_c is the standard deviation of the noise-free coefficients, α, β are the adaptive parameters. So, combine with the MAP method, the noise-free curvelet coefficient c_i was estimated by

$$\hat{c}_i = \frac{\left(\|y\| - \frac{\beta\sigma_n^2}{\sigma}\right)_+}{\|y\|} \cdot y_i, \quad (3.3)$$

where, $\|y\|$ is the neighbor coefficients, σ_n is the noise variance, and σ is the noise image variance.

Obviously, the above mentioned shrinkage function is an incomplete one. It does not consider the relationship of the coefficient and its parent value. In many cases, the probability density of sparse decomposition is obeying non-Gaussian distribution; the authors do not consider it. Furthermore, in our previous work, we found that the curvelet transform use the slant stack method for Cartesian-to-Polar conversion, which makes higher computation redundancy. Contourlet transform uses the piecewise quadratic continuous curve, which has different scales and multi directions, to gain the image coefficients. So, the contourlet decomposition is prior than curvelet transform. In next section, we propose a non-Gaussian multivariate shrinkage method for image denoising based on contourlet transform.

3.2 Bayesian Contourlet Estimator of BKF

In this section, we propose a new model for non-Gaussian image denoising, which based on Bayesian MAP estimator rule.

Let g equally spaced samples of a real-valued image. n is i.i.d. normal random variables. The image with noise x can be expressed as

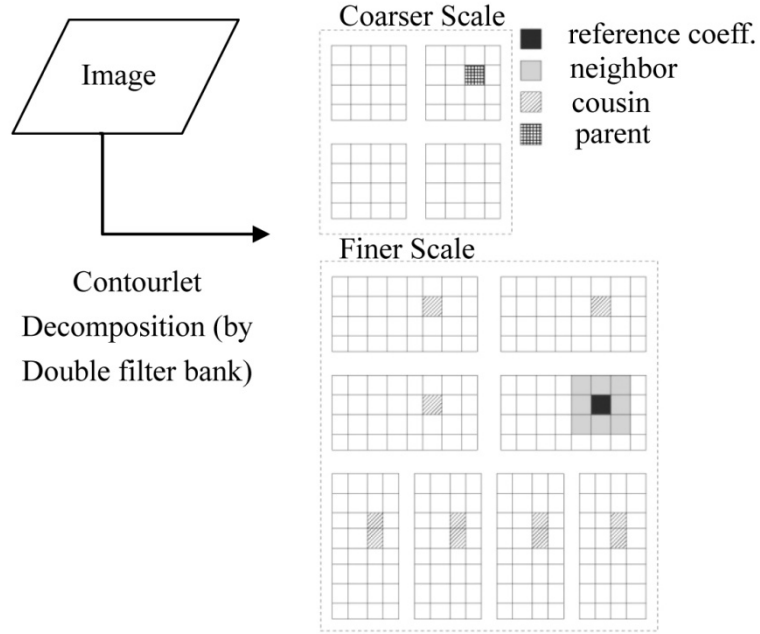


Figure 3-1: Contourlet coefficient relationships in different scales.

$$x = g + n \quad (3.4)$$

In the contourlet domain, the problem can be formulated as

$$\mathbf{y} = \mathbf{s} + \mathbf{n} \quad (3.5)$$

where $\mathbf{y} = (y_1, y_2, \dots, y_M)$ is the noise contourlet coefficient, $\mathbf{s} = (s_1, s_2, \dots, s_M)$ is the true coefficient, and $\mathbf{n} = (n_1, n_2, \dots, n_M)$ is the independent noise. The standard MAP estimator for (3.5) is

$$\hat{\mathbf{s}}(\mathbf{y}) = \arg \max_{\mathbf{s}} p_{\mathbf{s}|\mathbf{y}}(\mathbf{s} | \mathbf{y}). \quad (3.6)$$

Using the Bayes rule, the Eq.(3.6) is equivalent to

$$\begin{aligned} \hat{\mathbf{s}}(\mathbf{y}) &= \arg \max_{\mathbf{s}} [p_{\mathbf{y}|\mathbf{s}}(\mathbf{y} | \mathbf{s}) p_{\mathbf{s}}(\mathbf{s})] \\ &= \arg \max_{\mathbf{s}} p_{\mathbf{n}}(\mathbf{y} - \mathbf{s}) p_{\mathbf{s}}(\mathbf{s}) \end{aligned} \quad (3.7)$$

The Eq.(3.7) is equivalent to

$$\hat{\mathbf{s}}(\mathbf{y}) = \arg \max_{\mathbf{s}} [\log(p_{\mathbf{n}}(\mathbf{y} - \mathbf{s})) + \log(p_{\mathbf{s}}(\mathbf{s}))] \quad (3.8)$$

The spherically-contoured zero-mean d -dimensional BKF density is

$$p_s(\mathbf{s}) = \frac{2}{(2\pi c)^{d/2} \Gamma(p)} \left(\frac{\sqrt{2c}}{\|\mathbf{s}\|} \right)^{d/2-p} K_{1-p} \left(\sqrt{\frac{2}{c}} \|\mathbf{s}\| \right) \quad (3.9)$$

where, $K_{1-p}(u)$ is the modified Bessel function. c and p are the scale parameter and shape parameter. Γ is the generalized incomplete Gamma function. Here, we propose a simple non-Gaussian multivariate PDF to model the noise-free coefficients, considering the relationship between coefficients, neighbors; cousins and parent (see Figure 3-1). The input image decomposed by multiscale filters and directional filters. Then, to coarser scale and finer scale, we consider the relationships of the reference coefficients like Figure 3-1. The noise-free coefficient is obtained by

$$p_Y(\mathbf{y}) = \frac{\exp\left(\frac{\sigma_n^2}{c}\right)}{(2\pi c)\Gamma(p)} \times \sum_{j=0}^{\infty} \left(-\frac{\sigma_n^2}{c}\right)^j \frac{(p-1)_j}{j!} \Gamma\left(p - \frac{d}{2} - j, \frac{\sigma_n^2}{c}, \frac{\|\mathbf{y}\|^2}{2c}\right) \quad (3.10)$$

with j factor in both the numerator and denominator of the fraction. σ_n is the standard deviation of the noise coefficients. In Ref. [67], the variables $\mathbf{y} = \text{sqrt}(\|y_i\|^2 + \|y_i^{[p]}\|^2 + \|y_i^{[c]}\|^2)$, y_i and $y_i^{[p]}$ are dependent to each other, but the neighbors and cousins are independent to parent. Let us use the MAP estimator for this model. Maximizing the Eq. (3.8) for each component, we can get

$$y_i = \hat{\mathbf{s}}_i - \sigma_n^2 \frac{d \log p_s(\mathbf{s})}{d\hat{\mathbf{s}}_i} \quad (3.11)$$

where, $i \in [1, d]$. By the way, the property of the modified Bessel function of the second kind $K_\lambda(u)$ is

$$\frac{d}{du} \log K_\lambda(u) = \frac{\lambda}{u} - \frac{K_{\lambda+1}(u)}{K_\lambda(u)} \quad (3.12)$$

Then, the second term of Eq. (3.11) can be computed as

$$\frac{d}{d\hat{s}_i} \log p_s(s) = -\frac{\hat{s}_i}{\|\hat{s}\|} \sqrt{\frac{2}{c}} \frac{K_{d/2-p+1}(\sqrt{2/c} \|\hat{s}\|)}{K_{d/2-p}(\sqrt{2/c} \|\hat{s}\|)} \quad (3.13)$$

Though the above Eqs., the MAP estimator can be formulated using Eq.(3.10) and Eq.(3.12), it gives

$$y_i = \hat{s}_i \left[1 + \frac{\sigma_n^2}{\|\hat{s}\|} \sqrt{\frac{2}{c}} \frac{K_{d/2-p+1}(\sqrt{2/c} \|\hat{s}\|)}{K_{d/2-p}(\sqrt{2/c} \|\hat{s}\|)} \right] \quad (3.14)$$

Then, we approximate the $\|\hat{s}\|$ as $\|\mathbf{y}\|$. The multivariate shrinkage function can be written as

$$\hat{s}_i \approx \frac{\mathbf{y}_i}{\left[1 + \frac{\sigma_n^2}{\|\mathbf{y}\|} \sqrt{\frac{2}{c}} \frac{K_{d/2-p+1}(\sqrt{2/c} \|\mathbf{y}\|)}{K_{d/2-p}(\sqrt{2/c} \|\mathbf{y}\|)} \right]} \quad (3.15)$$

where $\sigma_n = \text{Median}(y_i)/0.6748$, $p = 3/(\text{Kurt}(X)-3)$, $c = \text{Var}(X)/p$. X is the HH subband. $\text{Var}(X)$ and $\text{Kurt}(X)$ are the variance and kurtosis.

The entire flowchart of our processing is: First, the input noisy image is decomposed to contourlet subbands. To local neighborhood pixels (e.g., parent, cousins and neighbors) are estimated by BKF-Baysian estimation rule. Then, the new coefficient of reference pixel is gotten. Through the contourlet transform reconstruction, we get the “clean” contourlet subbands. Finally, the denoised image is acquired.

3.3 Quality Metrics

Let x_i and y_i be the i -th pixel in the original image \mathbf{x} and the distorted image \mathbf{y} , respectively. The MSE and $PSNR$ between the two images are given by [57],

$$MSE = \frac{1}{N} \sum_{i=1}^N (x_i - y_i)^2, \quad (3.16)$$

$$PSNR = 10 \log_{10} \left(\frac{L^2}{MSE} \right) \quad (3.17)$$

In Ref. [57, 69], a multi-scale SSIM method for image quality assessment is proposed.

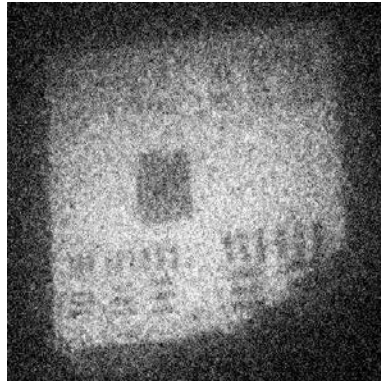
Input to signal A and B , let μ_A , σ_A and σ_{AB} respectively as the mean of A , the variance of A , the covariance of A and B . The parameters of relative importance α , β , γ are equal to 1. The SSIM is given as follow:

$$SSIM(x, y) = \frac{(2\mu_A\mu_B + C_1)(2\sigma_{AB} + C_2)}{(\mu_A^2 + \mu_B^2 + C_1)(\mu_A^2 + \mu_B^2 + C_2)} \quad (3.18)$$

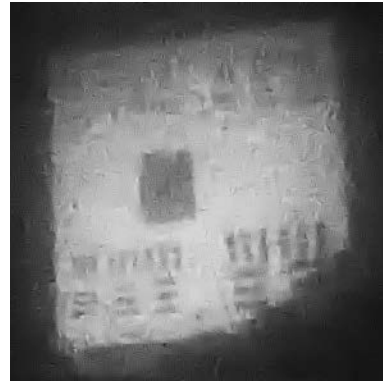
3.4 Experiments and Discussions

In this section, we show some examples of image denoising using the proposed models described in the previous section. We use the Windows XP, Intel Core Duo2, 2.0GHz, 1 GB RAM memory computer for computing. In the next three sets image denoising experiments, we compare with the proposed method to the-state-of-the-art methods in details.

The proposed denoising method is applied on underwater laser images, and outdoor image processing in practice. The results are shown in Figure 3-2. The test image is gotten by [70]. This gated image token by range gated underwater camera “TURN LLC 2003” at 7.0 meter distance. We test 100 LLS images, the average PSNR is nearly $2dB$ improved than the state-of-the-art models (see Table 3-1).



(a)



(b)

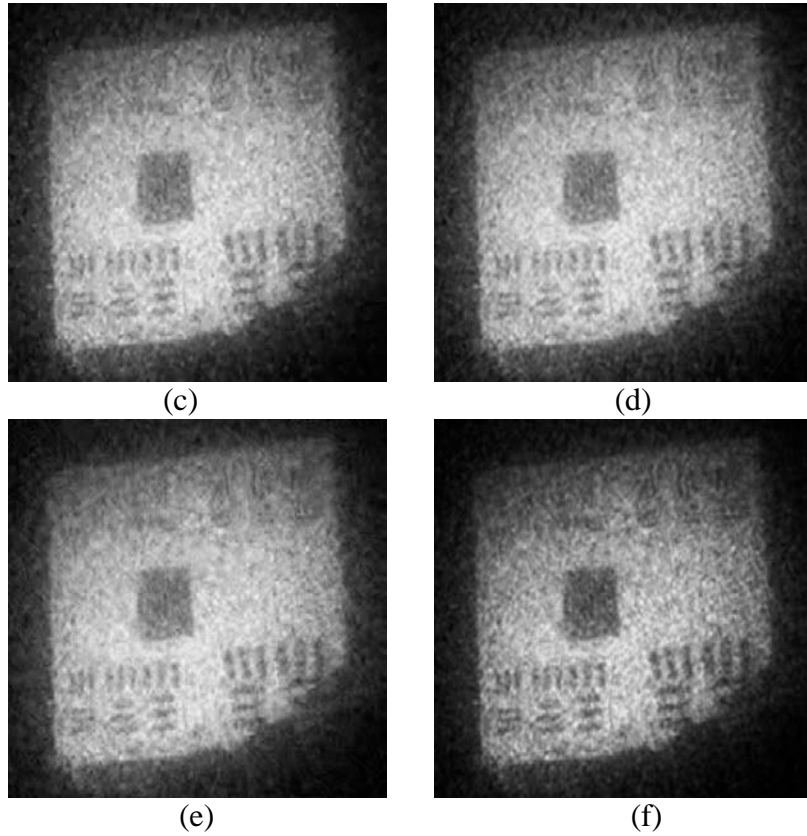


Figure 3-2: Denoised images from the LLS dataset. (a) Original noisy image. (b) Wavelet hard thresholding. (c) BLS-GSM. (d) Curvelet K-sigma. (e) ContourletHMT. (f) denoised with the proposed method.

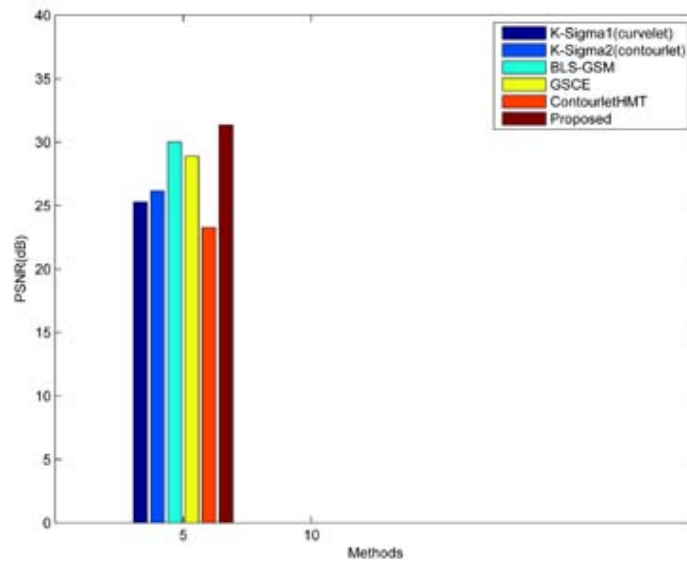


Figure 3-3: After denoising PSNR values of different methods in 100 samples, PSNR(K-Sigma1)=25.28 dB, PSNR(K-Sigma2)=26.16 dB, PSNR(BLS-GSM)=30.01 dB, PSNR(GSCE)=28.89 dB, PSNR(ContourletHMT)=23.28 dB,

PSNR(Proposed)=31.36 dB.

In Figure 3-3, we test 100 LLS images, the average PSNR is nearly 2dB improved than the state-of-the-art models.

TABLE 3-1: PSNR and SSIM values of denoised images for LLS image with different methods

Method	PSNR [dB]	SSIM
Wavelet Hard thresholding	18.69	0.6485
BLS-GSM	37.28	0.8832
Curvelet K-sigma	36.36	0.9097
Curvelet GSCE	35.82	0.8963
ContourletHMT	32.12	0.8839
The proposed	36.74	0.9167

From the above analysis, we can find that our proposed method performs well than the other methods both in visual assessment and qualities analysis. Actually, the underwater viewing system can acquire clearer image by using other image processing approaches, such as image enhancement, image fusion [71], and underwater image dehazing [72].

3.5 Conclusion

This Chapter presents an effective and useful non-Gaussian multivariate shrinkage (NGMS) model for image denoising, which is based on the MAP estimation and the contourlet transform. We fully consider the dependencies between the center coefficient and its parent, cousins, neighbors in the NGMS model. In order to show the effectiveness of the NGMS estimator, three set examples are presented and compared with them in human visual system (HVS) and some well-defined mathematical frameworks. Experimental results demonstrate that the proposed NGMS method outperforms the state-of-the-art methods.

Chapter 4

Optical Image Dehazing

4.1 Background

Ocean exploration of the seafloor is used for various scientific reasons, for example, assessing the biological environment, mineral exploration, and taking population census. The problem of mitigating sea mines is challenging and difficult. Ocean mines may be located on the seabed, in the water column, or on the sea surface [73]. Recently, two deficiencies in mine counter measures are mentioned by researchers. First, the problem of mine hunting is one of the most important and difficult problems. Second, the key technologies for mine and mine-like objects recognition are not solving very well. To this end, in recent decades, most unmanned systems were developed for supporting underwater mining. The goal to develop an automation device for underwater mine detection is automatically determine the mine location and recognize the mine-like objects instead of the human. There are two stages of mine hunting operations. One is search-classify-map (SCM), which is intended to locate all sufficiently mine-like objects in a given operational area. The other is reacquire-and-identify (RI), which is to distinguish the mines or non-mines and prosecutes them accordingly.

Under recent concept of operations, automatics underwater vehicles (AUVs) based systems hosting low-frequency sonars are first used to search-classify-map relatively large areas at a high search rate. Abundant sonar systems were developed in the last two decades, such as side-looking sonar [74], volumetric sonar [75], and EO [76]. SCM is fast but not exactly determine the mines. So, the Reacquire-and-Identify are used to test and verify final classification by reacquiring the target, at a close range, with magnetic,

acoustic or electro-optic sensors. This paper will concentrate solely on the optical imaging sensors onboard the underwater mining system.

Although the underwater objects detection technology makes a great progress, the recognition of underwater objects also remains a major issue in recent days. Challenges associated with obtaining visibility of objects have been difficult to overcome due to the physical properties of the medium. Different from the natural images, because of the medium scattering and light distortion, underwater images suffer from poor visibility. The main issues for underwater imaging are that, first of all, capturing images underwater is difficult, mostly due to attenuation caused by light that is reflected from a surface and is deflected and scattered by particles, and absorption substantially reduces the light energy. Another reason is that the random attenuation of the light caused the haze appearance while the fraction of the light scattered back from the water along with the sight considerable degrades the scene contrast. In particular, the objects at a distance of more than 10 meters are almost indistinguishable with the colors are faded due to the characteristic wavelengths are cut according to the water depth [105]. Furthermore, as the artificial light is employed, there usually leave a distinctive footprint of the light beam on the seafloor.

Luckily, there have been many techniques to restore and enhance the underwater images [105]. Y.Y. Schechner et al [77] exploited the polarization dehazing method to compensate for visibility degradation. Ancuti et al [78] used image fusion method in turbid medium for reconstruct a clear image, and combining point spread function and a modulation transfer function to reduce the blurring effect by Hou et al [79]. B. Ouyang et al [70] proposed a bilateral filtering based image deconvolution method. Although the aforementioned approaches can enhance the image contrast, these methods have demonstrated several drawbacks that reduce their practical applicability. First, the equipment of imaging is difficult in practice (e.g. range-gated laser imaging system, which is hardly applied in practice). Second, multiple input images are required, which is difficult to capture by hardware. Third, they cannot solve the color distortion very well [105].

In this Chapter, we introduce a novel approach that is able to enhance underwater images based on single image to overcome the drawbacks of the above methods. We propose a new guided trigonometric filter instead of the matting Laplacian to solve the alpha mattes more efficiently. In short summary, our technical contributions are in threefold: first, the proposed guided trigonometric guided filter can perform as an edge-preserving smoothing operator like the popular bilateral filter, but has better behavior near the edges. Second, the novel guided filter has a fast and non-approximate constant-time algorithm, whose computational complexity is independent of the filtering kernel size. Third, the proposed α ACE is effectively in underwater image enhancement [110].

4.2 Bilateral filter and trigonometric bilateral filter

4.2.1 Bilateral Filter

Tomasi et al. [80] proposed the bilateral filtering in 1998. The bilateral filtering smooths images while preserving edges, by means of a nonlinear combination of nearby image values. The bilateral filtering is non-iterative, local, and simple. The traditional bilateral filter simultaneously weights pixels based on spatial distance from the center pixel as well as the distance in tone. The domain filter weights pixels based on their distance from the center is,

$$\nu(x - y) = \frac{1}{2} e^{-\frac{(x-y)(x-y)}{2\sigma_D^2}} \quad (4.1)$$

where x and y denote pixel spatial positions. The spatial scale is set by σ_D , The range filter weights pixels based on the photometric difference,

$$w(f(x) - f(y)) = \frac{1}{2} e^{-\frac{(f(x)-f(y))(f(x)-f(y))}{2\sigma_R^2}} \quad (4.2)$$

where $f(\bullet)$ is image tonal values. The degree of tonal filter is set by σ_R . The bilateral filter can be written as

$$B = \frac{\int_{R^d} f(y) \nu(x-y) w(f(x)-f(y)) dy}{\int_{R^d} \nu(x-y) w(f(x)-f(y)) dy} \quad (4.3)$$

Note that kernels other than Gaussian kernels are not excluded.

4.2.2 Box Filter

The box image filter [81] is that each pixel in the resulting image has a value equal to the average value of its neighboring pixels in the source image. It is a form of low-pass filter and is a convolution. Due to its property of using equal weights, it can be implemented using a much simpler accumulation algorithm which is significantly faster than using a sliding window algorithm.

In the frequency domain, the box filter has zeros and negative components. That is, a sine wave in a period equal to the size of the box which will be blurred away entirely and wavelengths shorter than the size of the box may be phase reversed, as seen when two bokeh circles touch to form a bright spot where there would be a dark spot between two bright spots in the original image.

4.2.3 Trigonometric Bilateral Filter

The computational complex of traditional bilateral filters with $O(N^2)$, we apply an exact bilateral filter whose computational complexity is linear in both input size and dimensionality. This trigonometric bilateral filter is $O(1)$. It is more efficient than the state-of-the-art bilateral filtering methods [82].

The standard Gaussian bilateral filter is given by

$$\tilde{f}(x) = \frac{1}{\eta(x)} \int_{\Omega} G_{\sigma_s}(y) G_{\sigma_r}(f(x-y) - f(x)) f(x-y) dy \quad (4.4)$$

where

$$\eta(x) = \int_{\Omega} G_{\sigma_s}(y) G_{\sigma_r}(f(x-y) - f(x)) dy$$

where G_{σ_s} is the Gaussian spatial kernel and G_{σ_r} is the one-dimensional Gaussian range kernel. η is the normalization coefficient.

Assuming the intensity values $f(x)$ to be restricted to the interval $[-T, T]$. G_{σ_r} is approximate by raised cosine kernels. This is motivated by observation that, for all $-T \leq s \leq T$,

$$\lim_{N \rightarrow \infty} \left[\cos\left(\frac{\gamma s}{\sqrt{N}}\right) \right]^N = \exp\left(-\frac{\gamma^2 s^2}{2\rho^2}\right) \quad (4.5)$$

where $\gamma = \pi/2T$ and $\rho = \gamma\sigma_r$ are used to control the variance of the target Gaussian on the right, and to ensure that the raised cosines on the left are non-negative and unimodal on $[-T, T]$ for every N .

The trigonometric function based bilateral filter [80] allows to express the otherwise non-linear transform in Eq.(4.4) as the superposition of Gaussian convolutions, applied on simple point-wise transforms of the image with a series of spatial filtering,

$$(F_0 * G_{\sigma_r})(x), (F_1 * G_{\sigma_r})(x), \dots, (F_N * G_{\sigma_r})(x) \quad (4.6)$$

where the image stack $F_0(x), F_1(x), \dots, F_N(x)$ are obtained from point-wise transform of $f(x)$. Each of these Gaussian filtering are computed using $O(1)$ algorithm. And the overall algorithm has $O(1)$ complexity.

4.3 GTBF for Dehazing

In the optical model, the acquired image can be modeled as being composed of two components. One is the direct transmission of light from the object, and the other is the transmission due to scattering by the particles of the medium (*e.g.* airlight) [96,109]. Mathematically, it can be written as,

$$I(x) = J(X)t(X) + (1 - t(X))A \quad (4.7)$$

where I is the achieved image. J is the scene radiance or haze-free image, t is the transmission along the cone of vision, and $t(x) = e^{-\beta d(x)}$, β is the attenuation coefficient of the medium, $d(x)$ is the distance between the camera and the object, A is the veiling color constant and $x = (x, y)$ is a pixel. The optical model assumes linear correlation between the reflected light and the distance between the object and observer.

Light propagation model is slightly different underwater environment. In the underwater optical imaging model, absorption plays an important role in image degrading. Furthermore, unlike scattering, the absorption coefficient is different for each colour channel, being the highest for red and lowest for blue in seawater. These leads to achieve the following simplified hazy image formation model:

$$I(x) = J(x)e^{-(\beta_s + \beta_a)d(x)} + (1 - e^{-\beta_s d(x)})A \quad (4.8)$$

where β_s is the scattering coefficient and β_a is the absorption coefficient of light. The effects of haze are highly correlated with the range of the underwater scene. In this paper, we simplify the situation as at a certain water depth, the transmission t is defined only by the distance between camera and scene (see Figure 4-1).

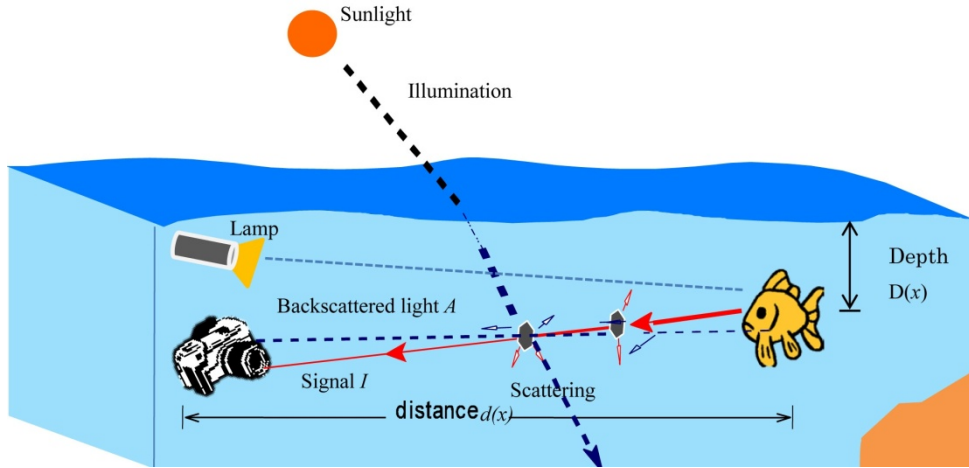


Figure 4-1: Underwater optical imaging haze model.

According to recent researches, we found that the red color channel is attenuated at a much higher rate than the green or blue channel. We further assume that the transmission in the water is constant. We denote the patch's transmission as $\tilde{t}(x)$. Take the maximum intensity of the red color channel to compare with the maximum intensity of the green and blue color channels. We define the dark channel $J_{\text{dark}}(x)$ for the

underwater image $J(x)$ as,

$$J_{dark}(x) = \min_{c \in \{r, g, b\}} (\min_{y \in \Omega(x)} J_c(x)) \quad (4.9)$$

where $J_c(x)$ refers to a pixel x in color channel $c \in \{r\}$ in the observed image, and Ω refers to a patch in the image. The dark channel is mainly caused by three factors, shadows, colorful objects or surfaces and dark objects or surfaces.

Here, take the min operation in the local patch on the haze imaging function (4.9), we assume the transmission as,

$$\min(I_c(x)) = \tilde{t}_c(x) \min_{y \in \Omega(x)} (J_c(x)) + (1 - \tilde{t}_c(x)) A_c \quad (4.10)$$

Since A_c is the homogeneous background light and the above equation and the above equation perform one more min operation among all three color channels as follows:

$$\min_c \min_{y \in \Omega(x)} \left(\frac{I_c(x)}{A_c} \right) = \tilde{t}_c(x) \min_c \left(\min_{y \in \Omega(x)} \left(\frac{J_c(x)}{A_c} \right) \right) + (1 - \tilde{t}_c(x)) \quad (4.11)$$

As Ref. [83], let us set $V(x) = A_c(1 - t(x))$ as the transmission veil, $W = \min_c(I_c(x))$ is the min color components of $I(x)$. We have $0 \leq V(x) \leq W(x)$. For grayscale image, $W = I$. Utilize the guided trigonometric bilateral filter (GTBF), we compute the $T(x) = \text{median}(x) - GTBF_{\Omega}(|W - \text{median}(x)|)$. And then, we can acquire the by $V(x) = \max\{\min[wT(x), W(x)], 0\}$, here w is the parameter in $(0,1)$. Finally, the transmission of each patch can be written as,

$$\tilde{t}(x) = 1 - \frac{V(x)}{A_c} \quad (4.12)$$

The background A_c is usually assumed to be the pixel intensity with the highest brightness value in an image. However, in practice, this simple assumption often renders erroneous results due to the presence of self-luminous organisms. So, in this chapter, we compute the brightest pixel value among all local min corresponds to the background light A_c as follows:

$$A_c = \max_{x \in I} \min_{y \in \Omega(x)} I_c(y) \quad (4.13)$$

where $I_c(y)$ is the local color components of $I(x)$ in each patch.

4.3.1 Guided Trigonometric Bilateral Filtering

In this subsection, we proposed guided trigonometric bilateral filter (GTBF) to overcome the gradient reversal artifacts occurring. The filtering process of GTBF is firstly done under the guidance of the image G that can be another or the input image I itself. Let I_p and G_p be the intensity value at pixel p of the minimum channel image and guided input image, w_k be the kernel window centered at pixel k , to be consistent with bilateral filter. GTBF [96, 109] is then formulated by

$$GBTF(I)_p = \frac{1}{\sum_{q \in w_k} W_{GBTF_{pq}}(G)} \sum_{q \in w_k} W_{GBTF_{pq}}(G) I_q \quad (4.14)$$

where the kernel weights function $W_{GBTF_{pq}}(G)$ can be written by

$$W_{GBTF_{pq}}(G) = \frac{1}{|w|^2} \sum_{k: (p,q) \in w_k} \left(1 + \frac{(G_p - \mu_k)(G_q - \mu_k)}{\sigma_k^2 + \varepsilon} \right) \quad (4.15)$$

where μ_k and σ_k^2 are the mean and variance of guided image G in local window w_k , $|w|$ is the number of pixels in this window. When both G_p and G_q are concurrently on the same side of an edge, the weight assigned to pixel q is large. When G_p and G_q are on different sides, a small weight will be assigned to pixel q . In this paper, we take trigonometric bilateral filter to accelerate the computational complex.

4.3.2 Recovering the Scene Radiance

With the transmission depth map, we can recover the scene radiance according to Eq. (4.7). We restrict the transmission $t(x)$ to a lower bound t_0 , which means that a small certain amount of haze are preserved in very dense haze regions. The final scene radiance $J(x)$ is written as,

$$J(\mathcal{X}) = \frac{I_c(\mathcal{X}) - A_c}{\max(t(\mathcal{X}), t_0)} + A_c \quad (4.16)$$

Typically, we choose $t_0=0.1$. The recovered image may be too dark. Here, we take α ACE for contrast enhancement in next subsection.

We apply the α ACE to correct the underwater distorted images. In this research, we set $\alpha=5$, the polynomial t is equal to

$$5.64305564j - 28.94026159j^3 + 74.52401661j^5 - 83.54012582j^7 + 33.39343065j^9.$$

Figure 4-2 shows the 9th degree approximation and approximation error.

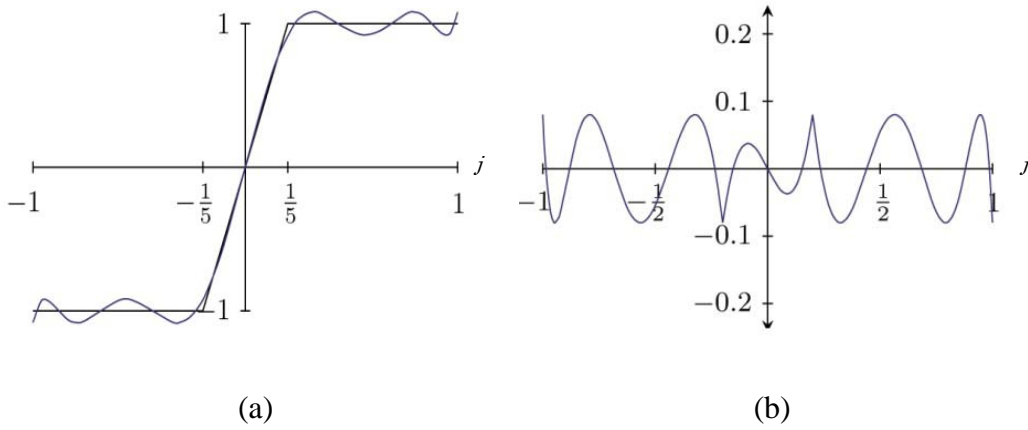


Figure 4-2: (a) s_α and its degree approximation; (b) approximation error.

4.4 Artificial Light Inhomogeneities Correction

In the deep sea, we must use artificial light for imaging. However, it will cause the vignetting effect. In Ref.[84], K. Sooknanan et al. proposed a multi-frame vignetting correction model for removing the vignetting phenomenon which involves estimating the light source footprint on the seafloor (see Figure 4-3).

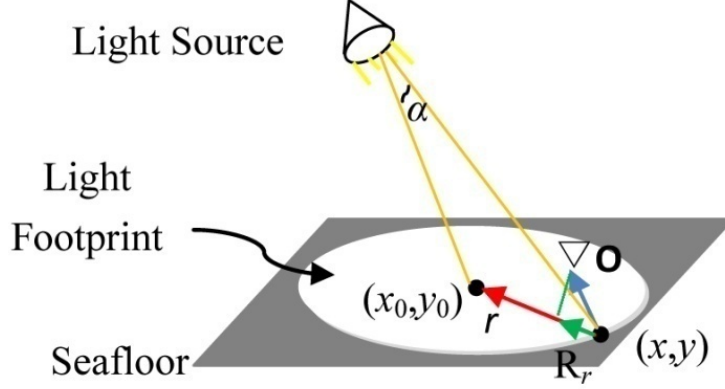


Figure 4-3: Underwater imaging vignetting model.

This artificial light correction can well done, however, it cost large time for computing. So, in this paper, we intend to introduce a signal frame-based vignette removal method [106]. Given the fact that we are interested in the overall effect of light attenuation through the system and not all of the image formation details, we have derived an effective degradation model, $Z(r, \theta)$ as follows,

$$Z(r, \theta) = O(r, \theta)V(r) \quad (4.18)$$

where Z is the image with vignetting, O is the vignetting-free image, and V is the vignetting function. Our goal is to find the optimal vignetting function V that minimizes asymmetry of the radial gradient distribution. By taking the log of Eq.(4.18), we get

$$\ln(Z(r, \theta)) = \ln O(r, \theta) + \ln V(r) \quad (4.19)$$

Let $\mathbf{Z} = \ln Z$, $\mathbf{O} = \ln O$, and $\mathbf{V} = \ln V$. We denote the radial gradients of \mathbf{Z} , \mathbf{O} , and \mathbf{V} for each pixel (r, θ) by $R_r^Z(r, \theta)$, $R_r^O(r, \theta)$, $R_r^V(r, \theta)$. Then,

$$R_r^Z(r, \theta) = R_r^O(r, \theta) + R_r^V(r, \theta) \quad (4.20)$$

Given an image \mathbf{Z} with vignetting, we find a maximum a posterior (MAP) solution to \mathbf{V} . Taking Bayes rule, we get,

$$\mathbf{V} = \arg \max_{\mathbf{V}} P(\mathbf{V} | \mathbf{Z}) \propto \arg \max_{\mathbf{V}} P(\mathbf{Z} | \mathbf{V})P(\mathbf{V}) \quad (4.21)$$

Considering the vignetting function at discrete, evenly sampled radii: $(\mathbf{V}(r_i), r_i \in S_r)$,

where $S_r = \{ r_0, r_1, \dots, r_{n-1} \}$. Each pixel (r, θ) is associated with the sector in it resides, and sector width is δr . The vignetting function is in general smooth, therefore, we obtain,

$$P(\mathbf{V}) = e^{-\lambda_s \sum_{r_i \in S_r} \mathbf{V}''(r_i)^2} \quad (4.22)$$

where λ_s is chosen to compensate for the noise level in the image, and $\mathbf{V}''(r_i)$ is approximated as

$$\mathbf{V}''(r_i) = \frac{\mathbf{V}(r_{i-1}) - 2\mathbf{V}(r_i) + \mathbf{V}(r_{i+1}))}{(\delta r)^2} \quad (4.23)$$

Using the sparsity prior method on the vignetting-free image \mathbf{O} ,

$$P(\mathbf{Z} | \mathbf{V}) = P(R_r^{\mathbf{O}}) = e^{-|R_r^{\mathbf{O}}|^\alpha}, \quad \alpha < 1 \quad (4.24)$$

Substituting Eq.(4.23) and Eq.(4.20), we have

$$P(\mathbf{Z} | \mathbf{V}) = e^{-\sum_{(r, \theta)} |\mathbf{R}_r^{\mathbf{Z}}(r, \theta) - \mathbf{R}_r^{\mathbf{V}}(r)|^\alpha} \quad (4.25)$$

The overall energy function $P(\mathbf{Z} | \mathbf{V})P(\mathbf{V})$ can be written as

$$E = \sum_{(r, \theta)} |\mathbf{R}_r^{\mathbf{Z}}(r, \theta) - \mathbf{R}_r^{\mathbf{V}}(r)|^\alpha + \lambda_s \sum_{r_i \in S_r} \mathbf{V}''(r_i)^2 \quad (4.26)$$

Through minimize E , we can estimate the $\mathbf{V}(r_i)$. Then, we use the IRLS technique for estimating the vignetting function.

4.5 Experiments and Discussions

The performance of the proposed system is evaluated both objectively and subjectively by utilizing ground-truth color patches. We also compare the proposed method with the state of the art methods. Both results demonstrate superior haze removing and color balancing capabilities of the proposed method over the others [109].

In the first experiment, we elaborate the flowchart of our system. Here, we select patch radius $r = 8$, $\varepsilon = 0.2 \times 0.2$ in Windows XP, Intel Core 2 (2.0GHz) with 1 GB RAM. From Figure 4-4, we firstly utilize holomorphic filter to correct the non-uniform

illumination roughly each color channel. Then, the DTC-wavelet transform is used to remove the noise. After that, through the artificial light selection policy, we directly use guided trigonometric bilateral filter-based dehazing method for haze or suspended solids removal. Finally, the underwater scene is reconstructed by α ACE color correction. We can found that the processed image is easier to see.

In the second experiment, we compare our method with most recent methods (such as Fattal, He and Xiao's work et al). Figure 4-5 and Figure 4-6 have shown the comparison results of different methods. Figure 4-7 shows the results using different de-scattering methods. Schechner's work produces blurring effects in the processed image. While Bazeille's pre-processing is serious distortion. The drawback of Fattal's method is that it needs to manually determine the background and foreground in the image. It is hard to use in practical application. Nicholas's Graph-cut based method cost a lot of processing time, while the processed image is also blurred. In comparison with He's method, our approach performs better, and as visible mosaic artifacts are observed in He's approach owing to the use of soft matting. Some of the regions are too dark (e.g. the right corner of the coral reefs), and haze is not removed elsewhere (e.g. the center of the image). In addition, there are also some unresolved scatters around the coral reefs in Ancuti's model. How to select the parameters for fusion is a hard work. Moreover, Chiang's work is distorted in colors. Meanwhile, the selection of parameters is also difficult. In our model, we just need 2 parameters to dehazing. Its CPU processing is less than 1 second. There are also some halos around the coral reefs in Xiao's model [85]. Our approach not only works well in haze removal, but also cost little computational complex. We can see the refined transmission depth map to compare these methods clearly in Fig 4-5.

In the third experiment, we simulate the mine detection system in the darkroom of our laboratory (see Figure 4-8). The distance between the mine-like objects to the underwater camera is 2 meters. We take the artificial light as an auxiliary light source. As a fixed light source, it caused uneven distribution of light. Because the light is absorbed in water, the imaging array of the camera captured a distorted video frame, see Figure 4-4 (a). Figure 4-4 (b) shows the denoised image, electrical noise and additional

noise are removed. After estimation, we use single frame vignetting method to remove artificial light. And the dehazing method is proposed to eliminate the haze in the image. After that, the contrast of Figure 4-4 (d) is obviously than Figure 4-4 (c). The obtained image is also too dark. So, αACE is used to enhancement the image. And finally, the sharp-based recognition method is used to distinguish the objects.

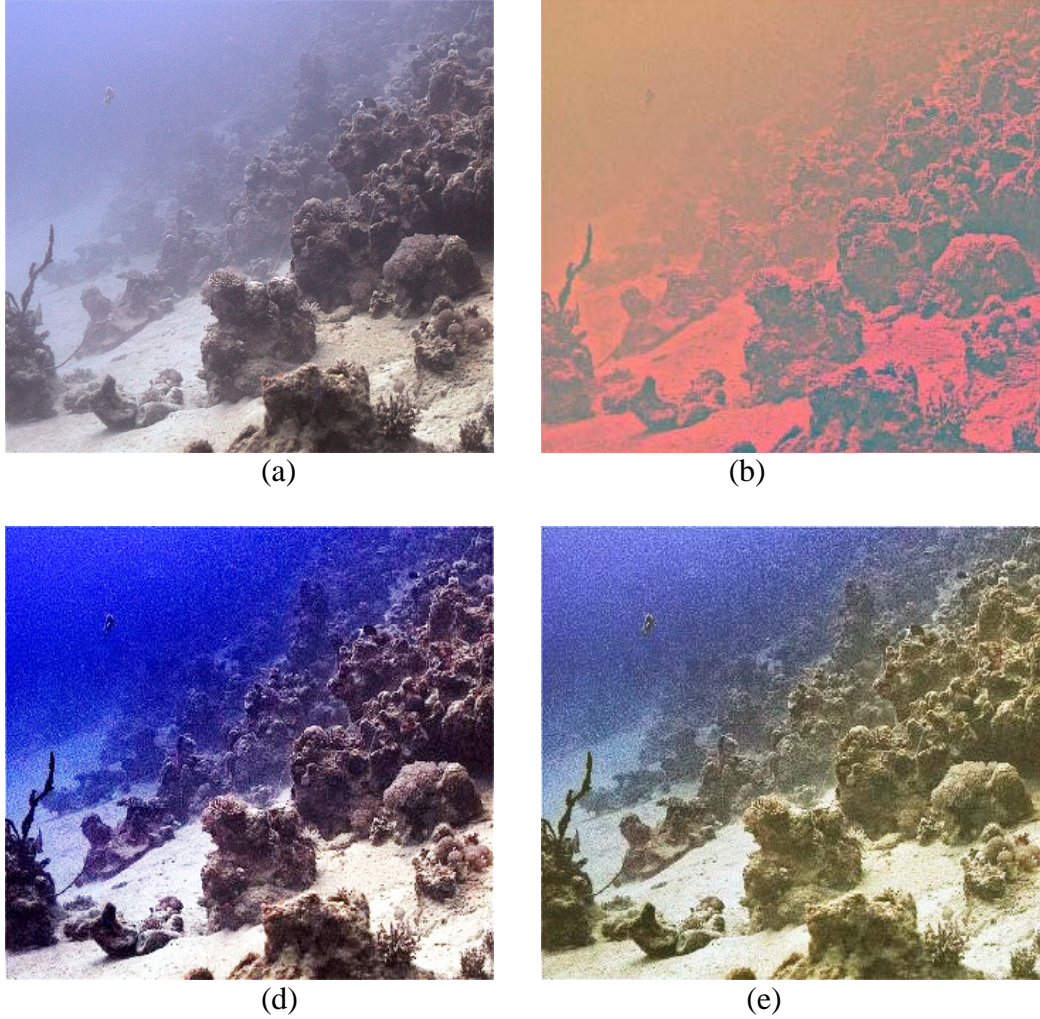
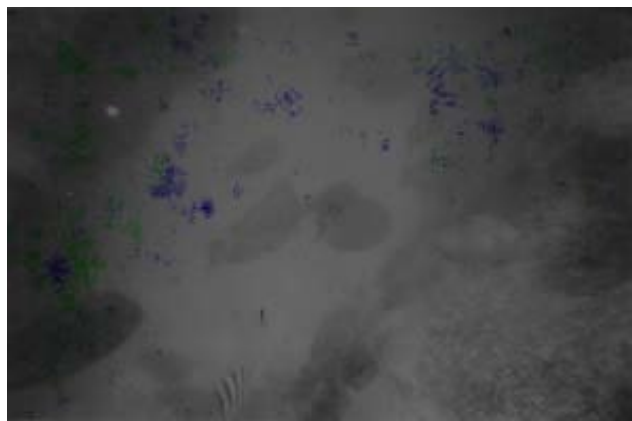


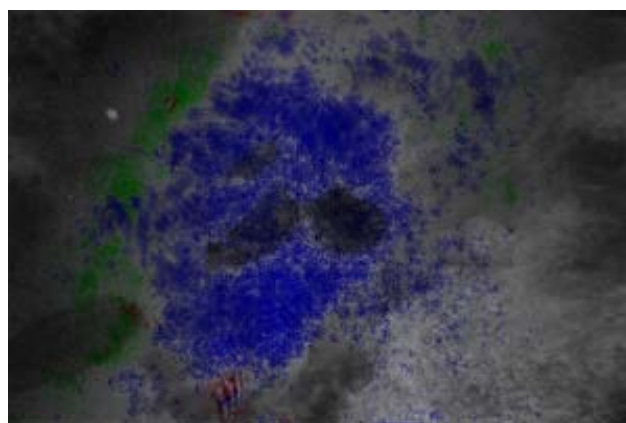
Figure 4-4: illumination of our proposed system.(a) Captured video frame; (b) After Homomorphic filtering; (c) GTB Filter Dehazing; (d) After αACE Color Enhancement.

This merit also can be confirmed by experiments in Figure 4-5. The size of the images is 397×264 pixels. Figure 4-5 shows the depth map of underwater fishes, and then estimated by HDR-VDP2-IQA index. We see that our method only contains the

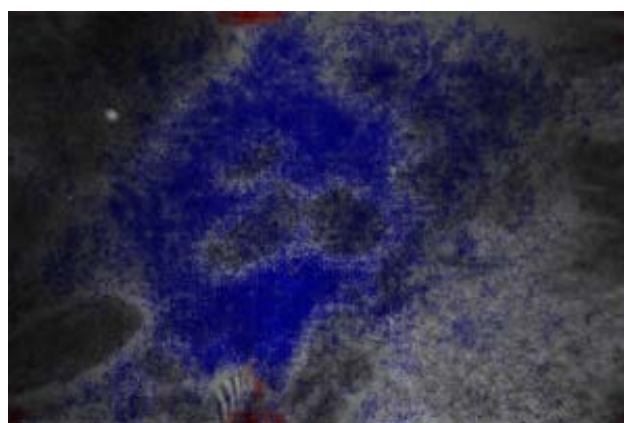
component of amplify of contrast (blue), nearly without the exhibit reverse (red) and losses of contrast (green).



(a)

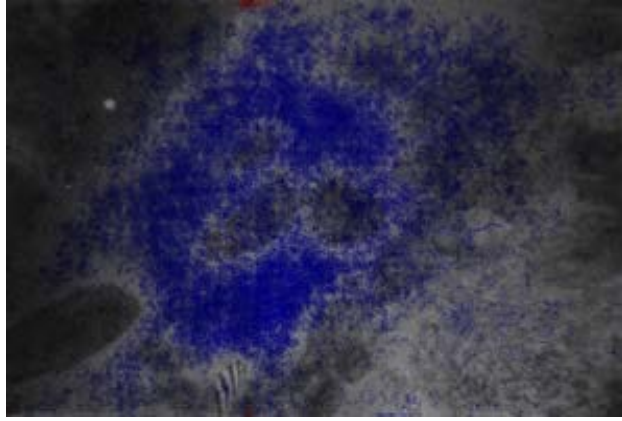


(b)



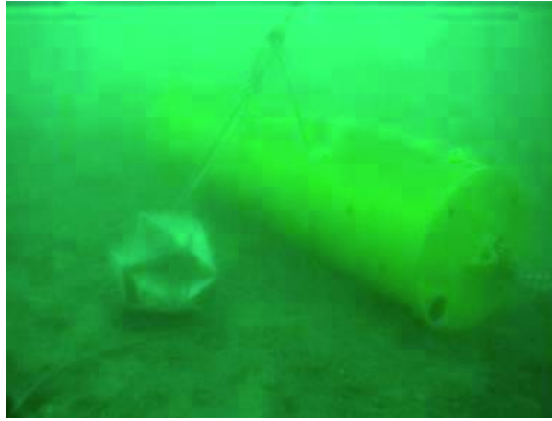
(c)

Figure 4-5: Probability of detection map of underwater fish. (a) Fattal's model. (b) He's model. (c) Xiao's model. (d) Our proposed model.



(d)

Figure 4-5: Probability of detection map of underwater fish. (a) Fattal's model. (b) He's model. (c) Xiao's model. (d) Our proposed model. (*Cont.*)



(a)



(b)



(c)

Figure 4-6: Enhanced underwater tank images. (a) Fattal's model. (b) He's model. (c) Xiao's model. (d) Our proposed model.



(d)

Figure 4-6: Enhanced underwater tank images. (a) Fattal's model. (b) He's model. (c) Xiao's model. (d) Our proposed model. (*Cont.*)

Table 4-1: CPU time of dehazed images in processing Figure 3-5 and Figure 3-6.

CPU time [s]	fish	tank
Fattal (2008)	17.14	14.40
He <i>et al</i> (2010)	32.20	34.54
Xiao <i>et al</i> (2012)	12.59	10.93
Our proposed	6.42	6.75

Figure 4-7 shows the underwater tank image with the size of 380×287 pixels. We can see that, the Fattal's model cannot achieve well in underwater image processing. The image is almost blurring. He's model performs well, but the iron chain on the lower right corner of the image is hardly to see. To Xiao's model, we can find that the image also contains a lot of suspended solids; the quality of image is bad. In our processed image, we can clearly watch the cable, iron chain et al, small objects very well. The processing speed of our proposed method is the fastest in the Table 4-2. That is because the proposed joint trilateral filter can be efficient computed with $O(N)$. These conclude that our model for underwater image or video processing better than the-state-of-the-art models.

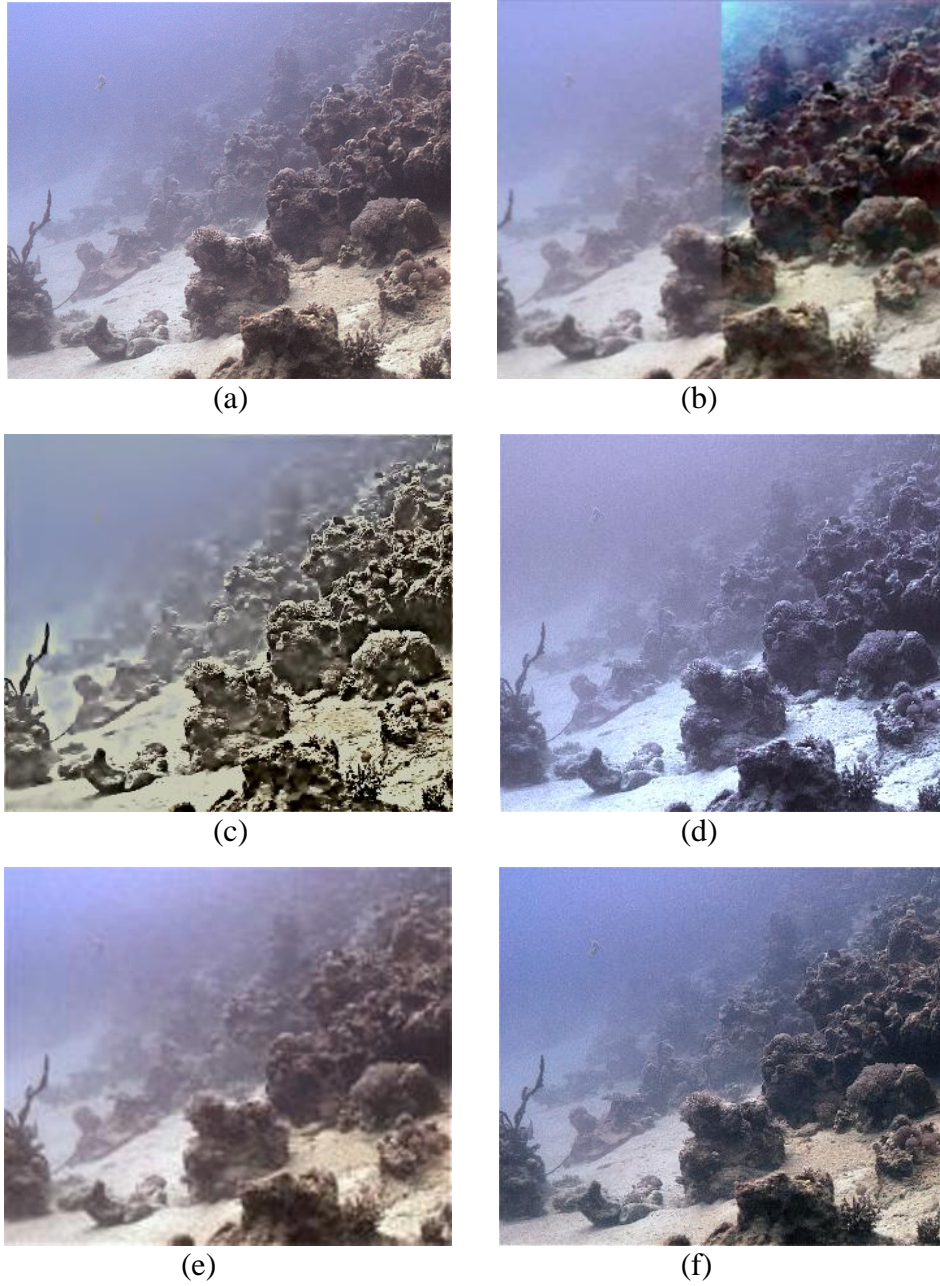


Figure 4-7: Different models for underwater image dehazing. (a) Captured video frame; (b) Schechner; (c)Bazeille; (d) Fattal; (e) Nicholas; (f) He; (g) Ancuti; (h) Chiang; (i) Xiao; (j) GTB Filter Dehazing.



(g)



(h)



(i)



(j)

Figure 4-7: Different models for underwater image dehazing. (a) Captured video frame; (b) Schechner; (c)Bazeille; (d) Fattal; (e) Nicholas; (f) He; (g) Ancuti; (h) Chiang; (i) Xiao; (j) GTB Filter Dehazing. (*Cont.*)

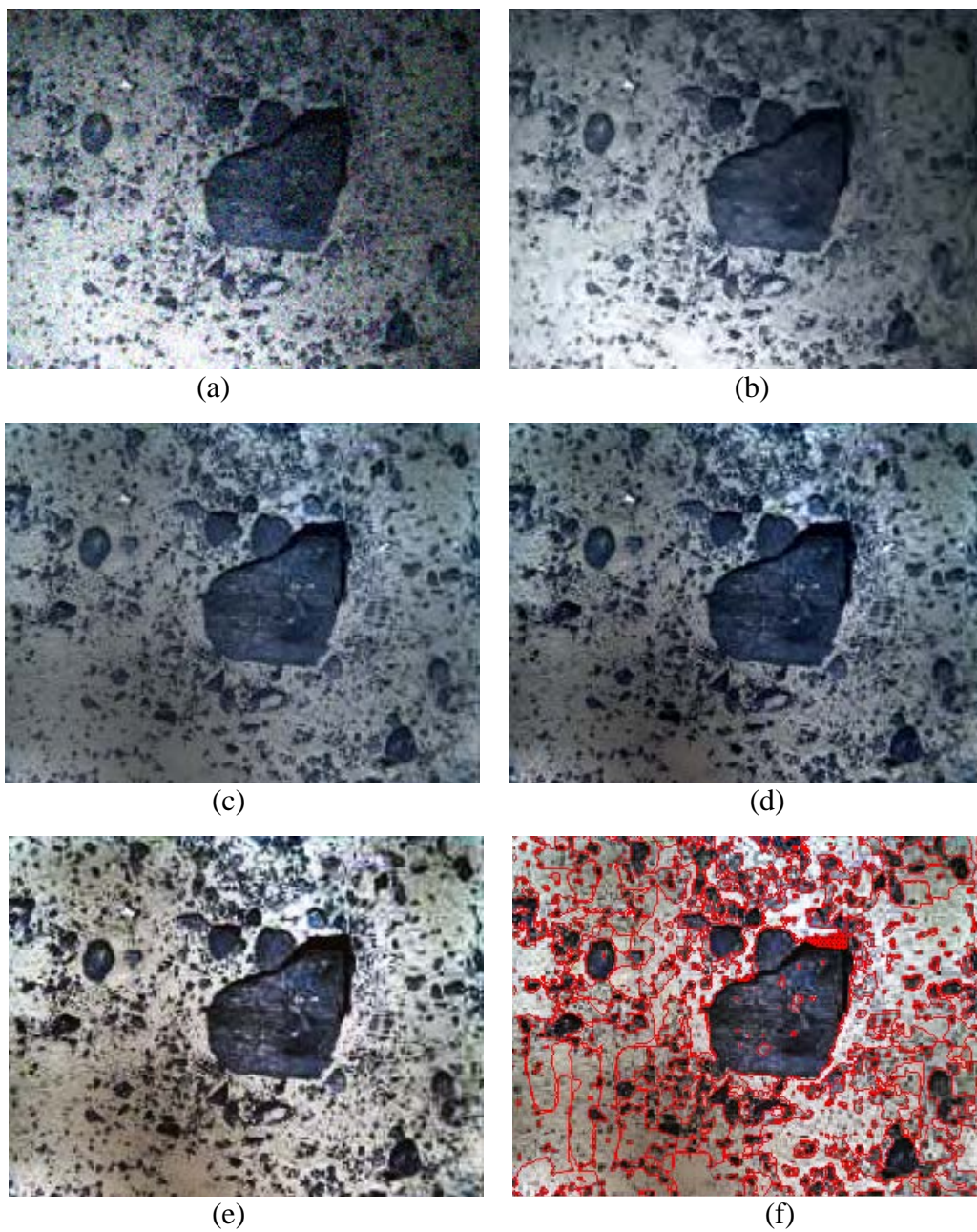
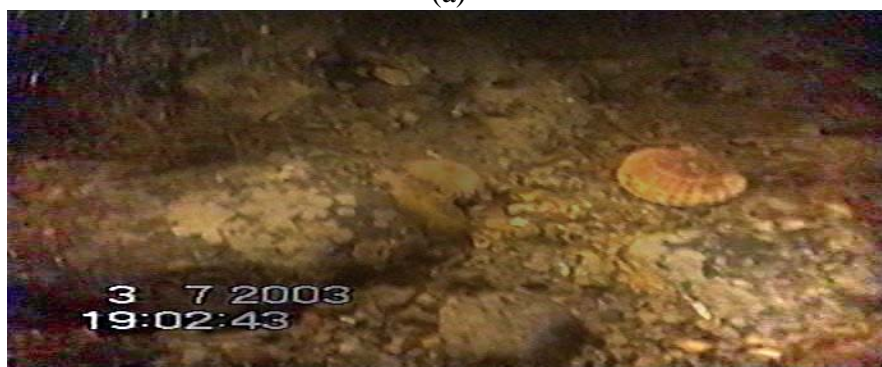


Figure 4-8: Simulations of Mine Detection in our Laboratory. (a) Captured video frame; (b) Denoised by Homomorphic filter and DTC-wavelet transform; (c) Vignetting correction; (d) GTB Filter Dehazing; (e) α ACE Color Enhancement; (f) Segmentation.



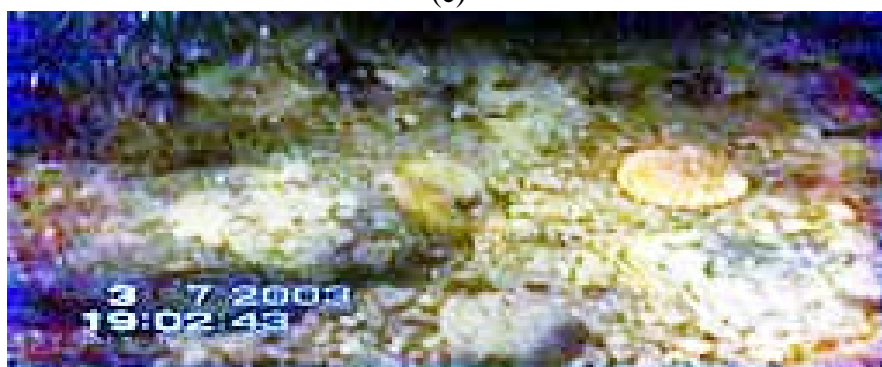
(a)



(b)



(c)



(d)

Figure 4-9: (a) Original degraded image; (b) Our result of artificial light correction; (c) Our result of GTBF dehazing; (d) Result of histogram correction.

We also test our system in real underwater coral reefs scene in Figure 4-9. Compared with the histogram equation (HE) method, it achieved a better image. The visibility of overall image is much better than the HE method [86].

The visual assessment demonstrates that our proposed method performs well. In addition to the visual analysis of these figures, we conducted quantitative analysis, mainly from the perspective of mathematical statistics and the statistical parameters of the images. These include High-Dynamic Range Visual Difference Predictor2 (HDR-VDP2) [87], and CPU time. HDR-VDP-2 is a very recent metric that uses a fairly advanced model of human perception to predict both visibility of artefacts and overall quality in images. The Q-MOS value is between 0 (best) to 100 (worst). Table 4-1 displays the Q-MOS of the pixels that have been filtered by applying HDR-VDP2-IQA, CPU computing time measure on several images.

Table 4-2: Quantitative Analysis

Methods	Indexes		
	HDR-VDP2-IQA (%)	Q-MOS	CPU time [s]
Fattal	1.8 _(Ampl.) , 16.7 _(Loss)	91.9044	20.05
He et al.	5.9 _(Ampl.) , 24.3 _(Loss)	65.1439	30.85
Xiao et al.	10.6 _(Ampl.) , 30.8 _(Loss)	54.5730	14.64
Our	35.4 _(Ampl.) , 1.8 _(Loss)	44.2046	4.42

4.6 Conclusion

This work has shown that it is possible to enhance degraded video sequences from seabed surveys using the image processing ideas. The proposed algorithm is automatic and requires little parameters adjustment. Total computing time of our system is about 1 minute. This algorithm is fast and can be improved with a translation C language and FPGA platform. We proposed a simple prior based on the difference in attenuation among the different color channels, which inspire us to estimate the transmission map. Another contribution is to compensate the transmission by guided trigonometric

bilateral filters, which not only has the benefits of edge-preserving and noise removing, but also speed up the computational cost.

Meanwhile, the proposed α ACE-based underwater image colorization method can color the underwater distorted images well than the state-of-the-art methods, also with little computation time. The artificial light correction method can eliminate the non-uniform illumination very well, and faster than the multiframe based vignetting correction methods.

Chapter 5

Shallow Water De-scattering

5.1 Background

With the development of autonomous underwater vehicles are usually used for underwater objects exploration. However, the recognition rate of underwater objects remains a major issue. For example, in order to immediately confirm the Fukushima Daiichi Nuclear Power Station, which was severely damaged during the Great East Japan Earthquake of March 11, 2011, the scientists remotely controlled the Disaster Recovery Support Robots (DRSR) for monitoring from safe areas [88-90, 98]. Although the underwater camera of DRSR took the videos for human decision, the video frame quality is poor (see Figure 5-1). To this end, take a suitable underwater image processing methods is important.

Contrast to common natural image, underwater optical image suffers from poor visibility by the medium degrading, which causing mainly scatters and color distortion. Large suspended particles cause scattering, just like in fog or turbid water that contains abundant particles. Encounter different degrees of attenuation in the water, color is distorted at different wavelengths, which causing ambient underwater environments to be dominated by a bluish tone.

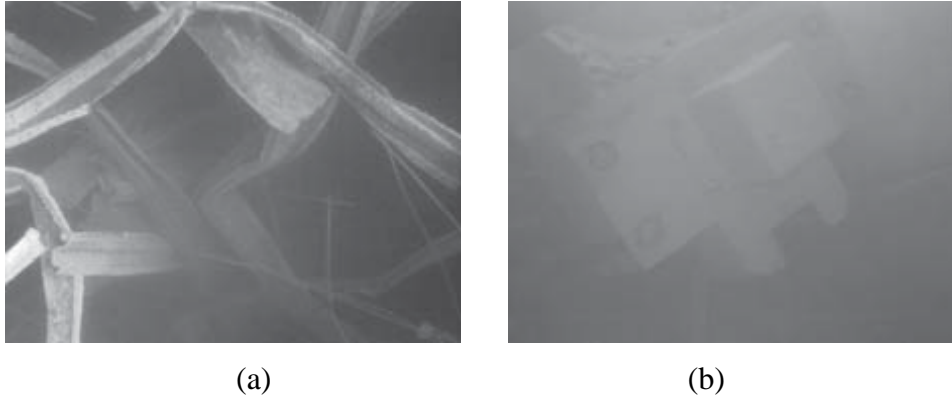


Figure 5-1: Views of situation in spent fuel pool at No.3 nuclear reactor of Fukushima Daiichi Nuclear Power Station. (a) Rubble near the water surface. (b) Part view of the fuel switch. (Courtesy by Tokyo Electric Power Company, Japan)

In addition, absorption greatly reduces the light energy. The random attenuation of sunlight primarily causes a hazy appearance, while the fraction of light scattered feedback from the water along with the line of sight considerably degrades the image contrast. In particular, objects at a distance of more than 10 meters are almost indistinguishable, because the colors are faded owing to the characteristic wavelengths that are filtered according to the water depth. Moreover, a distinctive footprint of the light beam is left on the seafloor when an artificial light source is employed [78].

Many researchers have developed techniques to restore and enhance underwater images. Y.Y. Schechner et al. exploited a polarization filter to compensate for visibility degradation [91], while Bazeille et al. proposed an image pre-processing pipeline for enhancing the turbidly underwater images [92]. Fattal designed a graphic theory based independent component analysis model to estimate the synthetic transmission and shading to recover the clean image [93]. He et al. estimated the dark prior channel through the images laws of nature, then used soft matting to refine the depth map and got the final clearly image. Nicholas et al. improved the dark prior channel, and took the graph-cut method instead of soft matting to refine the depth map [94]. Hou et al. combined a point spread function and modulation transfer function to reduce the effects of blurring [79]. Ouyang proposed bilateral filtering based on an image deconvolution

method [70]. Ancuti et al. used an exposed fusion method in a turbid medium to reconstruct a clear image [78]. Chiang et al considered the wavelength effects on underwater imaging, and the reconstructed image is obtained by dark prior channel model [72]. Although the aforementioned approaches can enhance the image contrast, these methods have demonstrated several drawbacks that reduce their practical applicability. First, the equipment for imaging is difficult to use in practice (e.g., a range-gated laser imaging system, which is rarely applied in practice). Second, multiple input images are required. Third, the dark prior channel may not suitable for underwater images. Fourth, manual operation is needed in processing, which leads to lack of intelligence [105].

Instead of multiple input images, we concerned the enhancement methods using a single image as input. Fattal estimated the scene radiance and derived the transmission image with a single image. However, this method cannot sufficiently process images with heavy haze. It also needs manual operation, which limits the application scope. He et al. analyzed abundant natural sky images, found that it contains a dark channel in color images, and proposed a scene depth information-based dark channel prior dehazing algorithm. However, this algorithm requires significant computation time and the processed images may be having artificial halos. To overcome this disadvantage, they also proposed a new guided image filter with the foggy image used as a reference image. However, this method leads to incomplete haze removal and cannot yet meet the requirements for real-time processing. Ancuti et al considered the Laplacian contrast, contrast, saliency and exposedness features between the white balanced image and color corrected image. Then, utilized the exposed fusion method for obtain the final image. However, this method has the two main disadvantages: obtained images with dark corner and parameters for processing are difficult to set. That is, the used exposed blending algorithm is sensitive in setting the parameters. In our previous work, we proposed guided trigonometric bilateral filter to refine the depth map of dark prior channel. The optimization algorithm can fully achieve better results with 2dB improved of PSNR value than the traditional methods. However, this method did not take the wavelength in to account.

Inspired by Chiang’s work [72], in this paper, we propose a novel shallow ocean optical imaging model and an enhancing algorithm. We firstly estimate the depth map through dark channels, then considering the positions of lighting lamp, camera and imaging plane, propose a rationally image model. Removing the scattering by taking weighted guided normalized convolution domain filter. Finally, the color corrected image is obtained by using wavelength compensation. The performance of the proposed method is evaluated both objectively and subjectively. The experiments show that the PSNR is improved by at least about 3dB than the state-of-the-art-methods, SSIM is improved about 0.015. The edges and details of the processed image are also improved significantly.

5.2 Underwater Imaging Model

Artificial light and atmospheric light traveling through the water is the source of illumination in a shallow ocean environment. Figure 5-2 shows an overview of the proposed underwater imaging model.

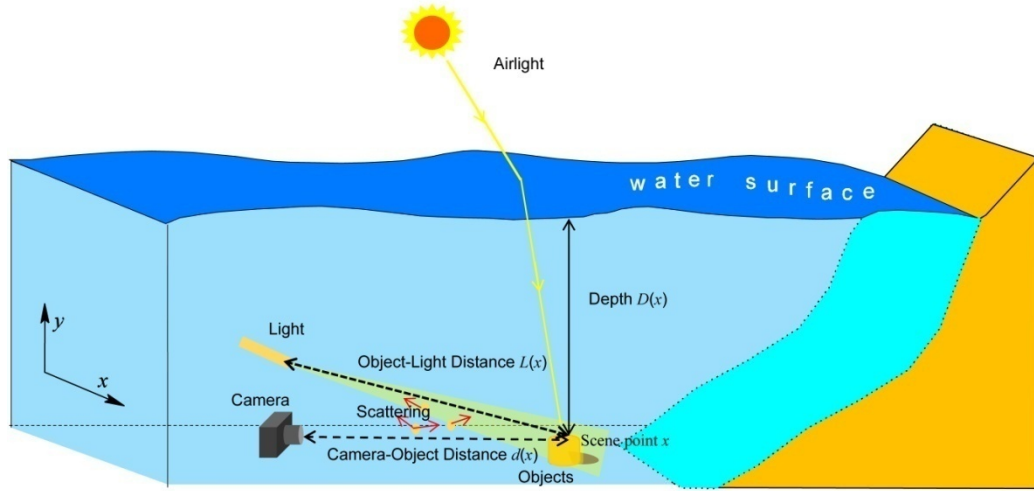


Figure 5-2: Underwater Optical Imaging Model.

Let suppose the amount of radiation light $W(x)$ formed after wavelength attenuation can be formulated according to the energy attenuation model as follows:

$$E_{\lambda}^W(x) = E_{\lambda}^A(x) \cdot Nrer(\lambda)^{D(x)} + E_{\lambda}^I(x) \cdot Nrer(\lambda)^{L(x)},$$

$$\lambda \in \{r, g, b\}$$
(5.1)

At the scene point x , the artificial light reflected again travels distance $L(x)$ to the camera forming pixel $I_{\lambda}(x)$, $\lambda \in \{r, g, b\}$. $D(x)$ is the scene depth underwater. The color distortion (absorption) and scattering are occurred in this process. We suppose the absorption and scattering rate is $\rho_{\lambda}(x)$, artificial light $J_{\lambda}(x)$ emanated from point x is equal to the amount of illuminating ambient light $E_{\lambda}^W(x)$ reflected,

$$E_{\lambda}^W(x) = \left(E_{\lambda}^A(x) \cdot Nrer(\lambda)^{D(x)} + E_{\lambda}^I(x) \cdot Nrer(\lambda)^{L(x)} \right) \cdot \rho(x),$$

$$\lambda \in \{r, g, b\}$$
(5.2)

By following the Nayar-Narasimhan hazing model, the image $I_{\lambda}(x)$ formed at the camera can be formulated as follows:

$$I_{\lambda}(x) = \left[\left(E_{\lambda}^A(x) \cdot Nrer(\lambda)^{D(x)} + E_{\lambda}^I(x) \cdot Nrer(\lambda)^{L(x)} \right) \cdot \rho_{\lambda}(x) \right] \cdot t_{\lambda}(x)$$

$$+ (1 - t_{\lambda}(x)) \cdot B_{\lambda}, \quad \lambda \in \{r, g, b\}$$
(5.3)

where the background B_{λ} represents the part of the object reflected light J_{λ} and ambient light E_{λ}^W scattered toward the camera by particles in the water. The residual energy ratio $t_{\lambda}(x)$ can be represented alternatively as the energy of a light beam with wavelength λ before and after traveling distance $d(x)$ within the water $E_{\lambda}^{residual}(x)$ and $E_{\lambda}^{initial}(x)$, respectively, as follows:

$$t_{\lambda}(x) = \frac{E_{\lambda}^{residual}(x)}{E_{\lambda}^{initial}(x)} = 10^{-\beta(\lambda)d(x)} = Nrer(\lambda)^{d(x)}$$
(5.4)

where $Nrer$ is the normalized residual energy ratio [14], in the Ocean Type I, it follows:

$$N_{rer}(\lambda) = \begin{cases} 0.8 \sim 0.85 & \text{if } \lambda = 650 \sim 750 \mu m (red) \\ 0.93 \sim 0.97 & \text{if } \lambda = 490 \sim 550 \mu m (green) \\ 0.95 \sim 0.99 & \text{if } \lambda = 400 \sim 490 \mu m (blue) \end{cases}$$
(5.5)

Consequently, subscribing the Eq. (5.3) and eq. (5.4), we can obtain:

$$I_{\lambda}(x) = \left[\left(E_{\lambda}^A(x) \cdot Nrer(\lambda)^{D(x)} + E_{\lambda}^I(x) \cdot Nrer(\lambda)^{L(x)} \right) \cdot \rho_{\lambda}(x) \right] \cdot Nrer(\lambda)^{d(x)} + \left(1 - Nrer(\lambda)^{d(x)} \right) \cdot B_{\lambda}, \quad \lambda \in \{r, g, b\} \quad (5.6)$$

The above equation incorporates light scattering during the course of propagation from object to the camera $d(x)$, and the wavelength attenuation along both the light-object path $L(x)$, scene depth $D(x)$ and object-camera path $d(x)$. Once the light-object distance $L(x)$, scene depth $D(x)$ and object-camera distance $d(x)$ is known, the final clean image will be recovered.

5.3 De-Scattering

5.3.1 Camera-object Distance $d(x)$ Estimation

In Ref. [72], the author found the red color channel is the dark channel of underwater images. During our experiments, we found that the lowest channel of RGB channels in turbidly water is not always the red color channel; the blue color channel is very significant. The reason is that we usually take the artificial light in imaging. Although the red wavelength absorbed easily through traveling in water, the distance between the camera and object is not enough to absorb the red wavelength significantly (See Figure 5-3). The blue channel may be the lowest. Consequently, in this work, we take the minimum pixel value as the rough depth map.



Figure 5-3: RGB histogram of Underwater Images.

As mentioned in Eq. (5.6), light $J_{\lambda}(x)$ reflected from point x is

$$J_{\lambda}(x) = \left(E_{\lambda}^A(x) \cdot Nrer(\lambda)^{D(x)} + E_{\lambda}^I(x) \cdot Nrer(\lambda)^{L(x)} \right) \cdot \rho_{\lambda}(x),$$

$$\lambda \in \{r, g, b\} \quad (5.7)$$

We define the minimum pixel channel $J_{dark}(x)$ for the underwater image $J_{\lambda}(x)$ as

$$J_{dark}(x) = \min_{\lambda} \min_{y \in \Omega(x)} J_{\lambda}(y), \lambda \in \{r, g, b\} \quad (5.8)$$

If point x belongs to a part of the foreground object, the value of the minimum pixel channel is very small. Taking the min operation in the local patch $\Omega(x)$ on the hazy image $I_{\lambda}(x)$ in Eq. (5.6), we have

$$\min_{y \in \Omega(x)} (I_{\lambda}(y)) = \min_{y \in \Omega(x)} \left\{ J_{\lambda}(y) \cdot Nrer(\lambda)^{d(y)} + (1 - Nrer(\lambda)^{d(y)}) \cdot B_{\lambda} \right\},$$

$$\lambda \in \{r, g, b\} \quad (5.9)$$

Since B_{λ} is the homogeneous background light and the residual energy ratio $Nrer(\lambda)^{d(y)}$ on the small local patch $\Omega(x)$ surrounding point x is essentially a constant $Nrer(\lambda)^{d(x)}$, the min value on the second term of (5.9) can be subsequently removed as

$$\min_{y \in \Omega(x)} (I_{\lambda}(y)) = \min_{y \in \Omega(x)} \left\{ J_{\lambda}(y) \cdot Nrer(\lambda)^{d(x)} + (1 - Nrer(\lambda)^{d(x)}) \cdot B_{\lambda} \right\},$$

$$\lambda \in \{r, g, b\} \quad (5.10)$$

We rearrange the above equation and perform on more min operation among all RGB color channels as follows:

$$\min_{\lambda} \left\{ \frac{\min_{y \in \Omega(x)} (I_{\lambda}(y))}{B_{\lambda}} \right\} = \min_{\lambda} \left\{ \frac{\min_{y \in \Omega(x)} J_{\lambda}(y)}{B_{\lambda}} \cdot Nrer(\lambda)^{d(x)} \right\}$$

$$+ \min_{\lambda} (1 - Nrer(\lambda)^{d(x)}), \quad (5.11)$$

$$\lambda \in \{r, g, b\}$$

Therefore, the second term of the above equation is dark channel equal to 0. Consequently, the estimated depth map is

$$\min_{\lambda} (Nrer(\lambda)^{d(x)}) = 1 - \min_{\lambda} \left\{ \frac{\min_{y \in \Omega(x)} (I_{\lambda}(y))}{B_{\lambda}} \right\}, \lambda \in \{r, g, b\} \quad (5.12)$$

$$d(x) = \ln \left(1 - \min_{\lambda} \left\{ \frac{\min_{y \in \Omega(x)} (I_{\lambda}(y))}{B_{\lambda}} \right\} \right) / \ln Nrer(\lambda) \quad (5.13)$$

5.3.2 Depth Map Refinement by Guided Multilayer Filter

In this subsection, we roughly estimated the camera-object distance $d(x)$. This distance depth contains mosaic effects and produces less accurately. Consequently, we need to use the proposed weighted guided normalized convolution domain filter to reduce the mosaicking. In this section, we introduce our constant time algorithm for weighted guided normalized convolution domain filter.

The traditional median filter has been considered as an effective way of removing “outliers”. The traditional median filter usually leads to morphological artifacts like rounding sharp corners. To address this problem, the weighted median filter has been proposed. The weighted median filter is defined as

$$h(\mathbf{x}, i) = \sum_{\mathbf{y} \in N(\mathbf{x})} W(\mathbf{x}, \mathbf{y}) \delta(V(\mathbf{y}) - i) \quad (5.14)$$

where $W(\mathbf{x}, \mathbf{y})$ corresponds to the weight assigned to a pixel \mathbf{y} inside a local region centered at pixel x , the weight $W(\mathbf{x}, \mathbf{y})$ depends on the image d that can be different from V . $N(\mathbf{x})$ is a local window near pixel \mathbf{x} . i is the discrete bin index, and δ is the Kronecker delta function, δ is 1 when the argument is 0, and is 0 otherwise.

Then the compute the refined depth map by weighted median filter with 2D normalized convolution domain transform filtering in the spatial domain as:

$$h(\mathbf{x}, i) = \sum_{\mathbf{y} \in N(\mathbf{x})} NC(\mathbf{x}, \mathbf{y}) \delta(V(\mathbf{y}) - i) \quad (5.15)$$

where $NC(\mathbf{x}, \mathbf{y})$ is the 1D normalized convolution domain filter, which is defined as:

$$NC(\mathbf{x}) = (1 / K_{\mathbf{x}}) \sum_{\mathbf{y} \in D(\Omega)} I_{NC}(\mathbf{y}) H(t(\hat{\mathbf{x}}), t(\hat{\mathbf{y}})) \quad (5.16)$$

where $K_{\mathbf{x}} = \sum_{\mathbf{y} \in D(\Omega)} H(t(\hat{\mathbf{x}}), t(\hat{\mathbf{y}}))$ is a normalization factor for \mathbf{x} , and $t(\hat{\mathbf{x}}) = t(x, ct(x))$.

Taking the efficient moving-average approach to perform NC with a box filter, the box

kernel is

$$H(t(\hat{\mathbf{x}}), t(\hat{\mathbf{y}})) = \delta_B\{|t(\hat{\mathbf{x}}) - t(\hat{\mathbf{y}})| \leq r\} \quad (5.17)$$

where $r = \sigma_H \sqrt{3}$ is the filter radius, and δ_B is a Boolean function that return 1 when its argument is true, and otherwise 0. σ_H is the standard deviation. The final refined depth map is produced by (see Figure 5-4):

$$h(\tilde{d}(x), i) = \sum_{y \in N(x)} NC(d(x), I) \delta(V(I) - i) \quad (5.18)$$

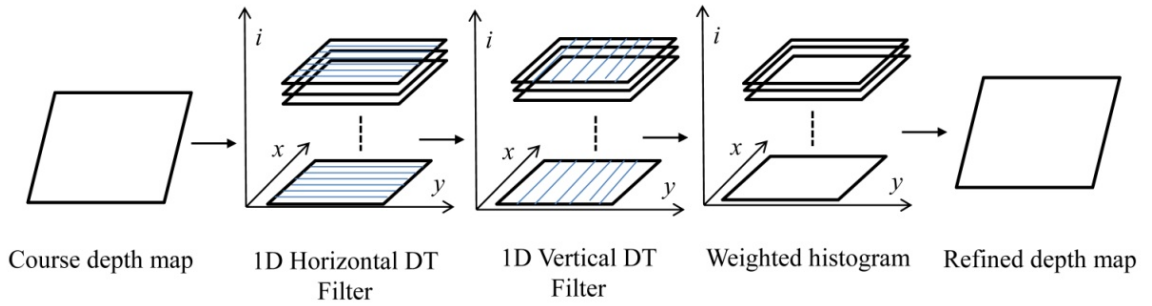


Figure 5-4: Weighted normalized convolution domain filtering.

Figure 5-4 shows the pipeline of weighted normalized convolution domain filter. This filters images, preserving edges and filters noise based on a dimensionality reduction strategy, having high quality results, while achieving significant speedups over existing techniques, such as bilateral filter [80], guided filter [95], trilateral filter [96] and weighted bilateral median filter [97]. The refined depth image is shown in Figure 5-5.

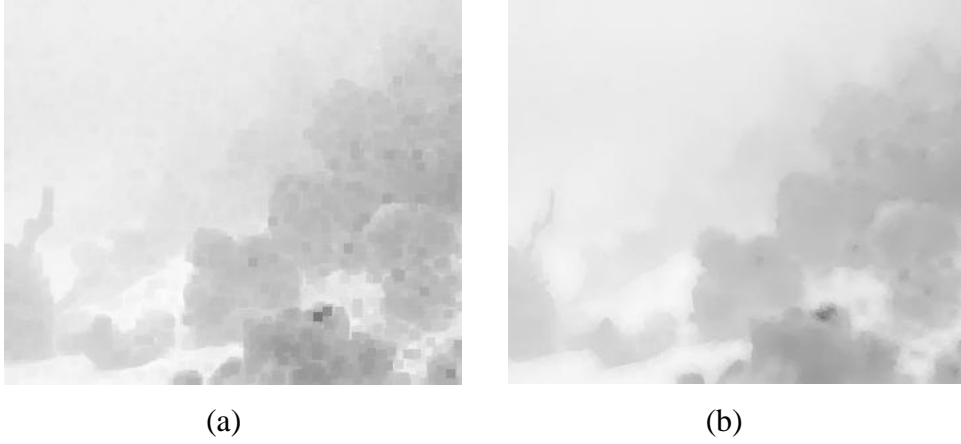


Figure 5-5: Depth map refinement by weighted normalized convolution domain filter.
(a) Input course depth image. (b) Refined depth image.

5.3.3 De-scattering

From above subsection, we obtained the refined depth map $d(x)$. In order to remove the scatter, we also need to solve the reflectivity $\rho_\lambda(x)$. We take the least squares solution for achieving this by

$$\begin{aligned} \rho_\lambda(x) = & \left(J_\lambda(x)^T \cdot J_\lambda(x) \right)^{-1} \cdot J_\lambda(x)^T \\ & \cdot \left(E_\lambda^A(x) \cdot Nrer(\lambda)^{D(x)} + E_\lambda^I(x) \cdot Nrer(\lambda)^{L(x)} \right), \end{aligned} \quad (5.19)$$

$$\lambda \in \{r, g, b\}$$

After removing the artificial light, the Eq. (5.6) can be written as

$$\begin{aligned} I_\lambda(x) = & E_\lambda^A(x) \cdot Nrer(\lambda)^{D(x)} \cdot \rho_\lambda(x) \cdot Nrer(\lambda)^{d(x)} \\ & + \left(1 - Nrer(\lambda)^{d(x)} \right) \cdot B_\lambda, \quad \lambda \in \{r, g, b\} \end{aligned} \quad (5.20)$$

According to Nayar-Narasimhan hazing model, we can obtain the descattered image by

$$\begin{aligned} \tilde{J}_\lambda(x) = & \frac{I_\lambda(x) - \left(1 - Nrer(\lambda)^{d(x)} \right) \cdot B_\lambda}{Nrer(\lambda)^{d(x)}} \\ = & E_\lambda^A(x) \cdot Nrer(\lambda)^{D(x)} \cdot \rho_\lambda(x) \cdot Nrer(\lambda)^{d(x)}, \end{aligned} \quad (5.21)$$

$$\lambda \in \{r, g, b\}$$

5.4 Experiments

The performance of the proposed algorithm is evaluated both objectively and subjectively, utilizing ground-truth color patches. We also compare the proposed method with the state-of-the-art methods. Both results demonstrate superior haze removal and color balancing capabilities of the proposed method over the others.

In the first experiment, we compare our method with the state-of-the-art methods with the underwater images offered by Dr. Y.Y. Schechner. The computer used is equipped with Windows XP and an Intel Core 2 (2.0 GHz) with 2 GB RAM. The size of the images is 345×292 pixels.

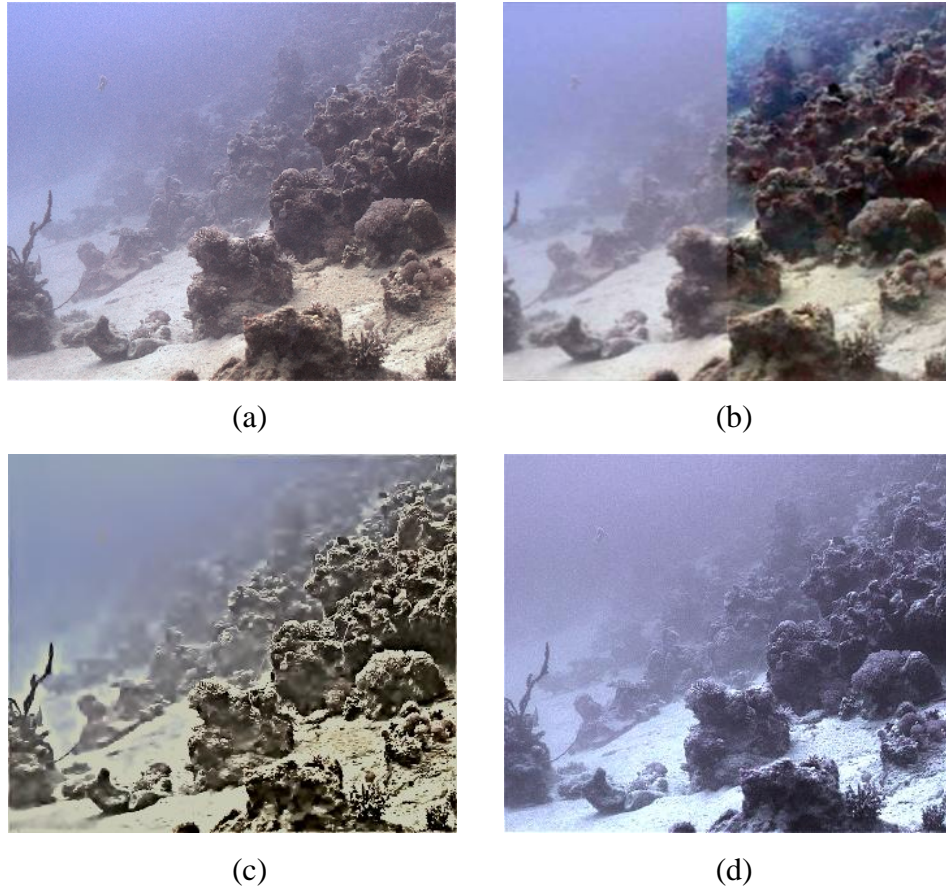


Figure 5-6: Results of different De-scattering methods. (a) Input Image; (b) De-scattered by Schechner; (c) De-scattered by Bazeille; (d) De-scattered by Fattal; (e) De-scattered by Nicholas; (f) De-scattered by He; (g) De-scattered by Ancuti; (h) De-scattered by Chiang; (i) De-scattered by Lu13; (j) De-scattered by Lu14.



(e)



(f)



(g)



(h)



(i)

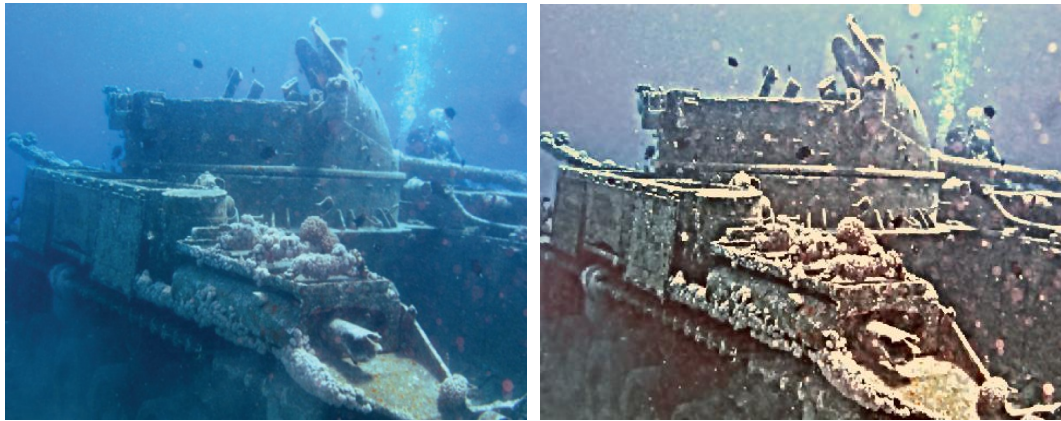


(j)

Figure 5-6: Results of different De-scattering methods. (a) Input Image; (b) De-scattered by Schechner; (c) De-scattered by Bazeille; (d) De-scattered by Fattal; (e) De-scattered by Nicholas; (f) De-scattered by He; (g) De-scattered by Ancuti; (h) De-scattered by Chiang; (i) De-scattered by Lu13; (j) De-scattered by Lu14. (*Cont.*)

Figure 5-6 shows the results using different de-scattering methods. Schechner's work produces blurring effects in the processed image. While Bazeille's pre-processing is serious distortion. The drawback of Fattal's method is that it needs to manually determine the background and foreground in the image. It is hard to use in practical application. Nicholas's Graph-cut based method cost a lot of processing time, while the processed image is also blurred. In comparison with He's method, our approach performs better, and as visible mosaic artifacts are observed in He's approach owing to the use of soft matting. Some of the regions are too dark (e.g. the right corner of the coral reefs), and haze is not removed elsewhere (e.g. the center of the image). In addition, there are also some unresolved scatters around the coral reefs in Ancuti's model. How to select the parameters for fusion is a hard work. Moreover, Chiang's work [72] is distorted in colors. Our previous work (Lu et al [96]) is performs well in descattering, however it cost a lot of time. Meanwhile, the selection of parameters is also difficult. In our model, we just need 2 parameters and CPU time is less than 1 sec.

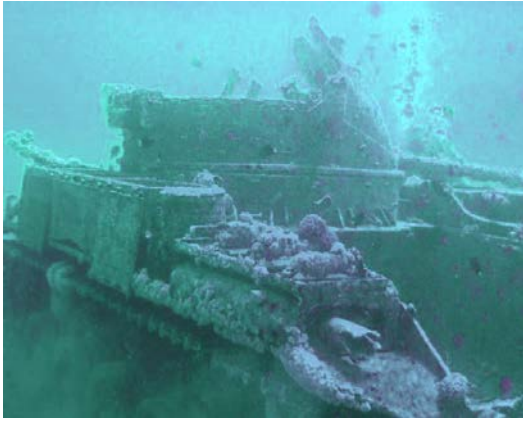
In the second experiment, we compare the different method with a large amount of images. Through the visual analysis, we can see that our proposed methods perform well than the others. Others have the color distortion largely.



(a)

(b)

Figure 5-7: Boat image de-scattering results. (a) Input image. (b) Bazeille's result. (c) Fattal's result. (d) He's result. (e) Ancuti's result. (f) Nicholas's result. (g) Lu13's result. (h) Lu14's result.



(c)



(d)



(e)



(f)



(g)



(h)

Figure 5-7: Boat image de-scattering results. (a) Input image. (b) Bazeille's result. (c) Fattal's result. (d) He's result. (e) Ancuti's result. (f) Nicholas's result. (g) Lu13's result. (h) Lu14's result. (*Cont.*)



(a)



(b)



(c)



(d)



(e)



(f)

Figure 5-8: Fish image de-scattering results. (a) Input image. (b) Bazeille's result. (c) Fattal's result. (d) He's result. (e) Ancuti's result. (f) Nicholas's result. (g) Lu13's result. (h) Lu14's result.



Figure 5-8: Fish image de-scattering results. (a) Input image. (b) Bazeille's result. (c) Fattal's result. (d) He's result. (e) Ancuti's result. (f) Nicholas's result. (g) Lu13's result. (h) Lu14's result. (*Cont.*)

Table 5-1: Comparative Analysis of Different De-scattering Methods (Figure 5-6).

Methods	PSNR [dB]	Q-MOS	SSIM
Schechner '05	15.7184	40.8985	0.3362
Bazeille '06	18.4609	49.8972	0.6157
Fattal '08	28.1155	91.9044	0.8328
Nicholas '10	24.8454	78.0455	0.6184
He '11	21.4759	92.5893	0.8191
Ancuti '12	21.7877	82.1602	0.7937
Chiang '12	25.3353	90.3737	0.8258
Lu '13	26.2918	92.3127	0.8293
Lu '14	28.4134	93.2458	0.8378

In addition to the visual analysis mentioned above, we conducted quantitative analysis, mainly from the perspective of mathematical statistics and the statistical parameters for the images (see Table 5-1). This analysis includes High-Dynamic Range Visual Difference Predictor2 (HDR-VDP2), PSNR, and SSIM. The Q-MOS value is between 0 (best) to 100(worst). Table 5-1 displays the Q-MOS of the pixels that have been filtered by applying HDR-VDP2-IQA. The results indicate that our approach not

only works well for haze removal, but also results in lower computation time.

We also test our algorithm by simulation. Figure 5-9 shows the results, and Table 5-1 shows the quantitative analysis results.

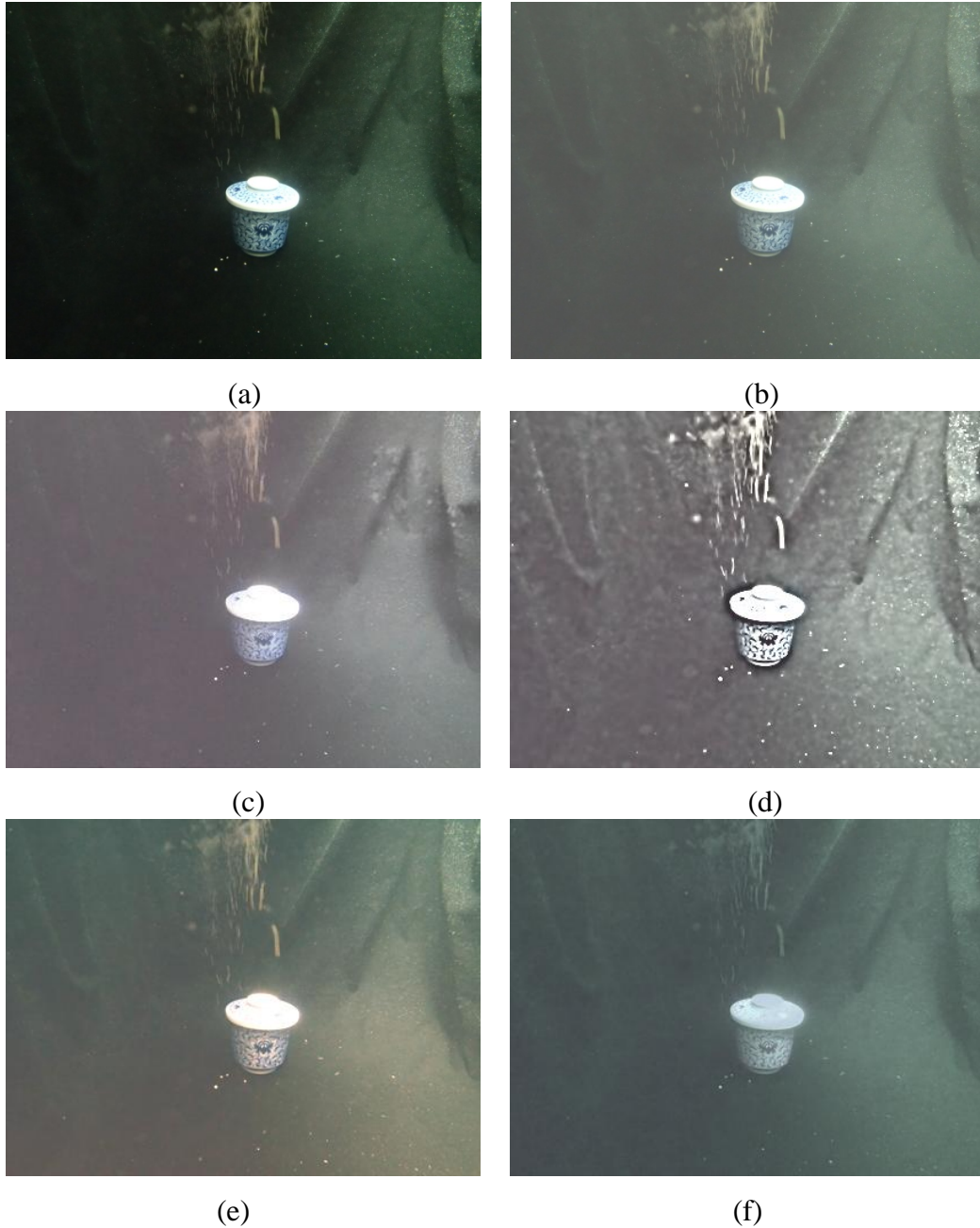


Figure 5-9: Simulation results by different descattering algorithms. (a) Noise-free image. (b) Noisy image. (c) Ancuti's result. (d) Bazeille's result. (e) Chiang's result. (f) Fattal's result. (g) He's result. (h) Nicholas's result. (i) Xiao's result. (j) Lu13's result. (k) Lu14's result.



(g)



(h)



(i)



(j)



(k)

Figure 5-9: Simulation results by different descattering algorithms. (a) Noise-free image. (b) Noisy image. (c) Ancuti's result. (d) Bazeille's result. (e) Chiang's result. (f) Fattal's result. (g) He's result. (h) Nicholas's result. (i) Xiao's result. (j) Lu13's result. (k) Lu14's result. (*Cont.*)

Table 5-2: Comparative Analysis of Different De-scattering Methods (Figure 5-9).

Methods	PSNR [dB]	MSE	SSIM
Ancuti	10.7715	5.4442e+003	0.5530
Bazeille	9.5787	7.1649e+003	0.4330
Chiang	11.7472	4.3487e+003	0.5198
Fattal	13.9595	2.6129e+003	0.6338
He	14.3188	2.4005e+003	0.6653
Nicholas	12.4260	3.7195e+003	0.5859
Xiao	13.0430	3.2269e+003	0.6307
Lu '13	27.0520	128.1966	0.9266
Lu '14	27.9921	103.2464	0.9367

5.5 Conclusion

In this study, we have explored and successfully implemented novel image enhancement techniques for underwater optical image processing. We have proposed a simple prior based on the difference in attenuation among the different color channels, which inspired us to estimate the transmission depth map. Another contribution compensated the transmission by weighted guided normalized convolution domain filtering, which has the benefits of edge-preserving, noise removing, and a reduction in the computation time. Moreover, the proposed underwater image colorization method successfully created colorful underwater distorted images that are better than the state-of-the-art methods with lower computation time. Furthermore, our proposed method solved the limitations due to the influence of possible artificial light sources.

Our experiments showed that the proposed methods are suitable for underwater imaging and solved the major problem of underwater optical imaging. In the future, we will consider developing a new deep-sea underwater imaging model to eliminate the haze problem based on recent oceanic technologies [99-103].

Chapter 6

Conclusions

This chapter summarizes the contents and contributions of the thesis, and suggests several directions for future work based on the current stage of the research thus far carried out.

6.1 Summary

In this thesis a full approach for underwater image restoration and enhancement have been proposed. The presented pipeline extends the common image restoration and enhancement techniques to the more complex and challenging underwater medium. The aim is the generation of clear images allowing the broad scale monitoring of seafloor extensions for geological, biological and environmental purposes.

Deep-sea or shallow ocean imaging suffers from specific problems that require the application of specific solutions. The contributions of this thesis concern all the imaging techniques (sonar imaging, laser imaging, and optical camera imaging) that can significantly improve the final image quality and visual pleasantness.

Chapter 2 describes a novel system for removing underwater sonar image noise, enhancing the structure of sonar images, and fusing the underwater sensed images, based on the decomposed curvelet coefficients. Side-scan sonar acquires high quality imagery of the seafloor with very high spatial resolution but poor locational accuracy. However, multi-beam sonar obtains high precision position and underwater depth in seafloor points. In order to fully utilize all information of these two types of sonars, it is necessary to fuse the two kinds of sonar data. This paper gives curvelet transform for enhancing the signals or details in different scales separately. It also proposes a new intensity sonar image fusion method, which is based on curvelet transform. Considering the sonar image forming principle, for the low frequency curvelet coefficients, we

utilize the maximum local energy method to calculate the energy of two sonar images. For the high frequency curvelet coefficients, we take absolute maximum method as a measurement. The main attribute of this paper is: Firstly, the multi-resolution analysis method is well adapted the cured-singularities and point-singularities. It is useful for sonar intensity image enhancement. Secondly, maximum local energy is well performing the intensity sonar images, which can achieve perfect fusion result. The experimental results show that the method can be used in the flat seafloor or the isotropic seabed. Compared with wavelet transform method, this method can get better performance [42].

Chapter 3 describes a statistical speckle suppression method for removing underwater image noise, based on the decomposed contourlet coefficients. This method utilizes Bayesian Contourlet Estimator of Bessel K Form (BCE-BKF) probability density function (PDF) to model neighborhood contourlet coefficients. After that, according to the proposed PDF model, we design a maximum a posteriori (MAP) estimator, which relies on a Bayesian statistics representation for the contourlet coefficients of noisy images. There are three obvious virtues of this method. Firstly, contourlet transform decomposition prior to curvelet transform and wavelet transform by using ellipse sampling grid. Secondly, BCE-BKF model is more effective in presentation of the noisy image contourlet coefficients. Thirdly, the BCE-BKF model takes full account of the correlation between coefficients. Some comparisons with the best available results will be present in order to illustrate the effectiveness of the proposed method [107].

Chapter 4 utilizes the image processing technologies to determine the mineral location and to recognize the mineral actually within a little processing time. We firstly analysis the recent underwater imaging models, and propose a novel underwater optical imaging model, which is much closer to the light propagation model in the underwater environment. In our imaging system, we remove the electrical noise by dual-tree complex wavelet transform. Then, solving the non-uniform illumination of artificial lights by fast guided trilateral bilateral filter and recovering the image color through automatic color equalization. Finally, a shape-based mineral recognition algorithm is proposed for underwater objects detection. These methods are designed for real-time

execution on limited-memory platforms, and are suitable for detecting underwater objects in practice. The initial results are presented and experiments demonstrate the effectiveness of the proposed imaging system [108].

Chapter 5 describes a novel method of enhancing underwater optical images or videos using guided multilayer filter and color correction. In certain circumstances, we need to immediately monitor the underwater environment by disaster recovery support robots. However, due to the inherent optical properties and underwater complex environment, the captured images or videos are distorted seriously. That is, absorption, scattering and color distortion are three major distortion issues for underwater optical imaging. Our key contributions proposed include a novel underwater imaging model to compensate for the attenuation discrepancy along the propagation path and a fast guided multilayer filtering enhancing algorithm. The enhanced images are characterized by a reduced noised level, better exposure of the dark regions, and improved global contrast where the finest details and edges are enhanced significantly. Consequently, our enhancement method achieves higher quality than other state-of-the-art methods [109].

6.2 Contributions

The present works led to some contributions to the state-of-the-art methods and are listed as follows:

- A novel system for removing underwater sonar image noise, enhancing the structure of sonar images, and fusing the underwater sensed images, based on the decomposed curvelet coefficients is proposed.
- A statistical speckle suppression method for removing underwater laser image noise, based on the decomposed contourlet coefficients. This method utilizes Bayesian contourlet Estimator of Bessel K Form probability density function to model neighborhood contourlet coefficient. After that, according to the proposed PDF model, we design a maximum a posteriori estimator, which relies on a Bayesian statistics representation for the contourlet coefficients.
- A novel method to enhance underwater optical images by guided trigonometric

bilateral filters and color correction is proposed. Our key contributions are proposed a new underwater model to compensate the attenuation discrepancy along the propagation path, and to propose a fast guided trigonometric bilateral filtering enhancing algorithm and a novel fast automatic color enhancement algorithm.

- A signal frame-based vignette removal method. Given the fact that we are interested in the overall effect of light attenuation through the imaging system and not all of the image formation details, the multiscale circle gradient de-vignetting are proposed.
- A wavelength compensation based shallow water scene reconstruction method is proposed. Meanwhile, a novel underwater imaging model to compensate for the attenuation discrepancy along the propagation path and a fast guided multilayer filtering enhancing algorithm.

6.3 Future Work

The proposed algorithms attempt to solve the underwater surveying vision problems by AUVs or Deep-sea Mining Systems (DMS). The field of underwater imaging is very young and much remains to be explored. Several long-term results would make a difference. Regarding future work, there are still several open problems which will require the development of new techniques.

On the one hand, the underwater imaging model may be unsuitable for turbidity water environment. Consequently, it is a challenge for pursuing a novel underwater optical imaging model.

On the other hand, for underwater image quality improvement model, new image processing technologies and automation technologies may be used for underwater image processing.

Furthermore, for the underwater illumination system we envision a LED-based continuous illumination version for videos. We would also like to see it integrated with methods coping with water turbidity. In addition, our correction method can be

integrated with 3D reconstruction techniques for color correcting highly three-dimensional objects.

Finally, AUV or DMS navigation underwater remains an open topic. We require our AUV or DMS to perform significant autonomous navigation tasks with the aid of acoustic and optical beacons. The potential of existing techniques localization and mapping techniques (e.g., SLAM) can be explored in this unique environment.

Bibliography

- [1] L.H. Somers, History of diving: Selected events, August 2002.
- [2] Z. Zhu, E. Riseman, A. Hanson, and H. Schultz, “An efficient method for geo-referenced video mosaicing for environmental monitoring”, *Machine Vision and Applications*, vol.16, no.4, pp.203-216, 2005.
- [3] O. Pizarro, and H. Singh, “Toward large-area mosaicking for underwater scientific applications”, *IEEE Journal of Oceanic Engineering*, vol.28, no.4, pp.651-672, 2003.
- [4] R. Eustice, H. Singh, J.J. Leonard, and M.R. Walter, “Visually mapping the RMS Titanic: Conservative covariance estimates for slam information filters”, *The International Journal of Robotics Research*, vol.25, no.12, pp.1223-1242, 2006.
- [5] http://en.wikipedia.org/wiki/Autonomous_underwater_vehicle
- [6] http://en.wikipedia.org/wiki/Remotely_operated_underwater_vehicle
- [7] http://en.wikipedia.org/wiki/Ultra-short_baseline
- [8] http://en.wikipedia.org/wiki/Long_baseline_acoustic_positioning_system
- [9] http://en.wikipedia.org/wiki/Acoustic_Doppler_Current_Profiler
- [10] H. Curtis, and N.S. Barnes, Biology, 5th Ed., Worth Publishers, New York, 1989.
- [11] J.F. Fish, C.S. Johnson, D.K. Ljungblad, “Sonar target discrimination by instrumented human divers”, *Journal of the Acoustical Society of America*, vol.59, no.3, pp.602-606, 1976.

- [12]D.M. Kocak, F.M. Caimi, “The current art of underwater imaging with a glimpse on the past”, *Marine Technology Society Journal*, vol.39, no.3, pp.5-26, 2005.
- [13]J.P. Fish, Sound underwater images: a guide to the generation and interpretation of side scan sonar data, 2nd Ed., Lower Cape Publishing, Oreleans, MA, 1991.
- [14]J.S.M. Rusby, J. Revie, “Long-range mapping of the continental shelf”, *Marine Geology*, vol.19, no.4, pp.M41-M49, 1975.
- [15]P. Blondel, and B.J. Murton, Handbook of seafloor sonar imagery, Wiley-Praxis Series in remote sensing, Edited by: D. Sloggett, John Wiley & Sons, Chichester, 1997.
- [16]E. Belcher, W. Hanot, J. Burch, “Dual-frequency identification sonar”, in: *Proc. of the 2002 International Symposium on Underwater Technology*, pp.187-192, 2002.
- [17]A. Davis, A. Lugsdin, “High speed underwater inspection for port and harbor security using Coda Echoscope 3D sonar”, in: *Proc. of MTS/IEEE OCEANS 2005*, vol.3, no.1-6, 2005.
- [18]BlueView Technologies, <http://www.blueviewtech.com>, last access: 14 December 2013.
- [19]R. Schettini, and S. Corchs, “Underwater image processing: state of the art of restoration and image enhancement methods”, *EURASIP Journal on Advances in Signal Processing*, vol.2010, ID 746051, pp.1-14, 2010.
- [20]Ocean Optics, www.oceanopticsbook.info
- [21]F. Bonin, A. Burguera, and G. Oliver, “Imaging systems for advanced underwater vehicles”, *Journal of Maritime Research*, vol. VIII, no.1, pp.65-86, 2011.
- [22]D.M. Kocak, F.R. Dalgleish, F.M. Caimi, Y.Y. Schechner, “A focus on recent developments and trends in underwater imaging”, *Marine Technology Society Journal*, vol.42, no.1, pp.52-67, 2008.

- [23]R.W. Preisendorfer, Hydrologic Optics, PMEL, NOAA, 1976.
- [24]E. Peli, “Contrast in complex images”, *Journal of Optical Society of America*, vol.7, no.10, pp.2032-2040, 1990.
- [25]M. Petrou, P. Bosdogianni, Image Processing, The fundamentals, Wiley Press, 1999.
- [26]K.M. Yemelyanov, S.S. Lin, E.N. Pugh, N. Engheta, “Adaptive algorithms for two-channel polarization sensing under various polarization statistics with nonuniform distributions”, *Applied Optics*, vol.45, no.22, pp.5504-5520, 2006.
- [27]S.S. Lin, K.M. Yemelyanov, E.N.P. Engheta, “Polarization enhanced visual surveillance techniques”, in: *Proc. of the 2004 IEEE International Conference on Networking Sensing and Control*, pp.216-221, Taiwan, 2004.
- [28]T. Treibitz, Y.Y. Schechner, “Instant 3descatter”, in: *Proc. of IEEE Conference on Computer Vision and Pattern Recognition*, pp.1861-1868, New York, U.S.A, 2006.
- [29]Y.Y. Schechner, Y. Averbuch, “Regularized image recovery in scattering media”, *IEEE Transactions on Pattern Analysis and Machine Intelligence*, vol.29, no.9, pp.1655-1660, 2007.
- [30]T. Treibitz, Y.Y. Schechner, “Active polarization descattering”, *IEEE Transactions on Pattern Analysis and Machine Intelligence*, vol.31, no.3, pp.385-399, 2009.
- [31]C.S. Tan, A.L. Sluzek, T.Y. Jiang, “Range gated imaging system for underwater robotic vehicle”, in: *Proc. of IEEE International Symposium on the Applications of Ferroelectrics*, pp.1-6, 2007.
- [32]C. Tan, G. Sluzek, D.M. He, “A novel application of range-gated underwater laser imaging system (ulis) in near target turbid medium”, *Optics and Laser in Engineering*, vol.43, pp.995-1009, 2005.

- [33]H. Li, X. Wang, T. Bai, W. Jin, Y. Huang, K. Ding, “Speckle noise suppression of range gated underwater imaging system”, *Applied Optics*, vol.38, no.18, pp.3937-3944, 2009.
- [34]J. Oakley, H. Bu, “Correction of simple contrast loss in color images”, *IEEE Transactions on Image Processing*, vol.16, no.2, pp.511-522, 2007.
- [35]F. Gasparini, S. Corchs, R. Schettini, “Low quality image enhancement using visual attention”, *Optical Engineering*, vol.46, no.4, pp.0405021-3, 2007.
- [36]R.C. Gonzalez, R.E. Woods, Digital Image Processing, 3rd Edn, Pearson Prentice Hall, U.S.A., 2008.
- [37]Y. Tao, H. Lin, H. Bao, F. Dong, G. Clapworthy, “Feature enhancement by volumetric unsharp masking”, *The Visual Computer*, vol.25, no.5-7, pp.581-588, 2009.
- [38]P. Jonsson, I. Sillitoe, B. Dushaw, J. Nystuen, J. Heltne, “Observing using sound and light- a short review of underwater acoustic and video-based methods”, *Ocean Science Discussions*, vol.6, pp.819-870, 2009.
- [39]H. Lu, S. Nakashima, Y. Li, L. Zhang, Y. Li, S. Serikawa, “Underwater Laser Images Denoising Using Bayesian Contourlet Estimator of Bessel K Form”, *Innovative Computing, Information and Control Express Letters, Part B: Applications*, vol.4, no.3, pp.533-539, 2013.
- [40]H. Lu, Y.Li, L. Zhang, S. Serikawa, “Enhancing Underwater Image by Dehazing and Colorization”, *International Review on Computers and Software*, vol.7, no.7, pp.3470-3474, 2012.
- [41]H. Lu, Y. Li, S. Serikawa, “Real-time Underwater Imaging System for Mineral Source Location and Concentration”, in: *Proc. of ECOS2013 – The 26th International Conference on Efficiency, Cost, Optimization, Simulation and Environmental Impact of Energy Systems*, G001, pp.1-15, 2013.

- [42]H. Lu, A. Yamawaki, S. Serikawa, “Curvelet Approach for Deep-sea Sonar Image Denoising, Contrast Enhancement and Fusion”, *Journal of International Council on Electrical Engineering*, vol.3, no.3, pp.250-256, 2013.
- [43]D.R. Yoerger, M. Jakuba, A.M. Bradley, B. Bingham, “Techniques for deep sea near bottom survey using an autonomous underwater vehicle, *Journal of Robotics Research*, vol.26, no.1, p41-54, 2007.
- [44]M. Soria, P.Freon, F. Gerlotto, “Analysis of Vessel Influence on Spatial Behavior of Fish Schools Using a Multi-beam Sonar and Consequences for Biomass Estimates by Echo-sounder”, *ICES Journal of Marine Science*, vol.53, pp.453-458, 1996.
- [45]P. Gervenka, C. de Moustier, “Post-processing and corrections of bathymetry derived from sides-can sonar systems: application with SeaMARC II”, *IEEE Journal of Oceanic Engineering*, vol.19, no.4, pp.619-629, 1994.
- [46]T.P. Le Bas, “An analytical correlation and comparison of high resolution side-scan sonar imagery and multi-beam bathymetry”, in: *Proc. of IEE Colloquium on Recent Development in Raider and Sonar Imaging System*, vol.6, pp.1-7, 1995.
- [47]B. Kamgar-Parsi, J.L. Jones, A. Rosenfeld, “Registration of Multiple Overlapping Range Images: Scenes without Distinctive Features”, *IEEE Transactions on Pattern Analysis and Machine Intelligence*, vol.13, no.9, p282-290, 1991.
- [48]S. Daniel, F. Le Leannec, C. Roux, B. Soliman, E.P. Mailard, “Side-scan sonar image matching”, *IEEE Journal of Oceanic Engineering*, vol.23, no.3, pp.245-259, 1998.
- [49]Z.X. Zhang, J.Q. Zhang, M.S. Liao, L. Zhang, “Automatic precision registration of multi-resolution remote sensing imagery”, *Journal of Wuhan Technical University of Surveying and Mapping*, vol.23, no.4, pp.320-323, 1998.

- [50]F.L. Yang, J.N. Liu, J.H. Zhao, “Multi-beam sonar and side-scan image co-registering and fusing”, *Marine Science Bulletin*, vol.5, no.1, pp.16-23, 2003.
- [51]Y. Hao, Q. Han, “Data Fusion of Multi-beam Sonar and Side-scan Sonar base on Feature Contour Registration”, in: *Proc. of IEEE Consumer Electronics Communications and Networks*, pp.174-177, 2011.
- [52]E.J. Candes, D.L.Donoho, *Curvelets: a surprisingly effective non-adaptive representation for object with edges*, Vanderbilt University Press, 1999.
- [53]H. Lu, Y.J. Li, Y. Kitazono, L.F. Zhang, S.Y. Yang, S. Serikawa, “Local energy based multi-focus image fusion method on curvelet transforms”, in: *Proc. of IEEE Symposium on Communications and Information Technologies*, pp.1154-1157, 2010.
- [54]M. Choi, R.Y. Kim, M.R. Nam, H.O. Kim, “The curvelet transform for image fusion”, in: *Proc. Of International Society for Photogrammetry and remote sensing*, pp.931-937, 2004.
- [55]H. Lu, X.L. Hu, L.F. Zhang, S.Y. Yang, S. Serikawa, “Local energy based image fusion in sharp frequency localized contourlet transform”, *Journal of Computational Information Systems*, vol.6, no.12, pp.3997-4005, 2010.
- [56]J.L. Starck, E. J. Candes, D.L. Donoho, “The curvelet transform for image denoising”, *IEEE Transactions on Image Processing*, vol.11, no.6, pp.670-684, 2002.
- [57]H. Lu, L. Zhang, S. Serikawa, “Maximum local energy: an effective approach for image fusion in beyond wavelet transform domain”, *Computers & Mathematics with Applications* (Elsevier), vol.64, no.5, pp.997-1004, 2012. (September 1, 2012).
- [58]Z. Wang, Q. Li, “Information content weighting for perceptual image quality assessment”, *IEEE Transactions on Image Processing*, vol.20, no.5, pp.1185-1198, 2011.

- [59]Z. Wang Q. Li, “A Universal Image Quality Index”, *IEEE Transactions on Signal Processing Letters*, vol.9, no.3, p81-84, 2002.
- [60]G. Piella, H. Heijmans, “A New Quality Metric for Image Fusion”, in: *IEEE International Conference on Image Processing*, pp. 173-176, 2003.
- [61]S.G. Chang, B. Yu, M. Vetterli, “Adaptive wavelet thresholding for image denoising and compression”, *IEEE Transactions on Image Processing*, vol.9, no.9, pp.1532-1546, 2000.
- [62]L. Sendur, I. W. Selesnick, “Bivariate shrinkage with local variance estimation”, *IEEE Signal Processing Letters*, vol.9, no.12, pp.438-441, 2002.
- [63]A. Achim, P. Tsakalides, A. Bezerianos, “SAR image denoising via bayesian wavelet shrinkage based on heavy-tailed modeling”, *IEEE Transaction on Geoscience and Remote Senses*, vol.41, no.8, pp.1773-1784, 2003.
- [64]D.L. Donoho, X. M. Huo, “Wedgelets: nearly-minimax estimation of edges”, *Annals of Statist*, vol.27, no.4, pp.857-897, 1999.
- [65]E. Le Pennec, S. Mallat, “Bandelet image approximation and compression”, *IEEE Transactions on Image Processing*, vol.14, no.1, pp.423-432, 2005.
- [66]A.A. Patil, J. Singhai, “Image denoising using curvelet transform: an approach for edge preservation”, *Journal of Scientific and Industrial Research*, vol.69, pp.34-38, 2010.
- [67]Q. Guo, S. Yu, “Image denoising using a multivariate shrinkage function in the curvelet domain”, *IEICE Electronics Express*, vol.7, no.3, pp.126-131, 2010.
- [68]D. D-Y. Po, M. N. Do, “Directional multiscale modeling of images using the contourlet transform”, *IEEE Transactions on Image Processing*, vol.15, no.6, pp.1610- 1620, 2006.

- [69]Z. Wang, A.C. Bovik, H.R. Sheikh, “Image quality assessment: from error visibility to structural similarity”, *IEEE Transactions on Image Processing*, vol.13, no.4, pp.600-612, 2004.
- [70]B. Ouyang, F.R. Dalglish, F.M. Caimi, et al., “Image Enhancement for Underwater Pulsed Laser Line Scan Imaging System”, in: *Proc. of the SPIE Ocean Sensing and Monitoring IV*, vol.8372, pp.83720R-83720R-12, 2012.
- [71]T. Treibitz, Y.Y. Schechner, “Turbid Scene Enhancement Using Multi-Directional Illumination Fusion”, *IEEE Transactions on Image Processing*, vol.21, no.11, pp.4662-4667, 2012.
- [72]J.Y. Chiang, Y.C. Chen, “Underwater Image Enhancement by Wavelength Compensation and Dehazing”, *IEEE Transactions on Image Processing*, vol.21, no.4, pp.1756-1769, 2012.
- [73]J. Stack, “Automation for underwater mine recognition: current trends and future strategy”, in: *Proc. of SPIE*, vol.80170K, pp.1-21, 2011.
- [74]G.J. Dobeck, J.C. Hyland, L. Smedley, “Automated detection/classification of sea mines in sonar imagery”, in: *Proc. of SPIE*, vol.3079, pp.90-110, 1997.
- [75]D.D. Sternlicht, R.D. Dikeman, D.W. Lemonds, M.T. Korporaal, A.M. Teranishi, “Target confirmation architecture for a buried object scanning sonar”, in: *Proc. of IEEE OCEANS*, vol.1, pp.1-9, 2003.
- [76]A. Nevis, J. Bryan, J.S. Taylor, B. Cordes, “Object detection using a background anomaly approach for electro-optic identification sensors”, <http://www.dtic.mil>, ADA749176, 2002.
- [77]Y.Y. Schechner, Y. Averbuch, “Regularized Image Recovery in Scattering Media”, *IEEE Transactions on Pattern Analysis & Machine Intelligence*, vol.29, no.9, pp.1655-1660, 2007.

- [78]C. Ancuti, C.O. Ancuti, T. Haber, P. Bekaert, “Enhancing Underwater Images and Videos by Fusion”, *in : Proc. of IEEE Conference on Computer Vision and Pattern Recognition*, pp.81-88, 2012.
- [79]W. Hou, D.J. Gray, A.D. Weidemann, G.R. Fournier, J.L. Forand, “Automated Underwater Image Restoration and Retrieval of Related Optical Properties”, *in : Proceeding of IEEE International Symposium of Geoscience and Remote Sensing*, pp.1889-1892, 2007.
- [80]C. Tomasi, R. Manduchi, “Bilateral filtering for gray and color images”, *in: Proc. of IEEE International Conference on Computer Vision*, vol.839-846, 1998.
- [81]H. Yu, L. Zhao, H. Wang, “Image denoising using trivariate shrinkage filter in the wavelet domain and joint bilateral filter in the spatial domain”, *IEEE Transactions on Image Processing*, vol.18, no.10, pp.2364-2369, 2009.
- [82]K.N. Chaudhury, D. Sage, M. Unser, “Fast $O(1)$ bilateral filtering using trigonometric range kernels”, *IEEE Transactions on Image Processing*, vol.20, no.12, pp.3376-3382, 2011.
- [83]K. He, J. Sun, X. Tang, “Single Image Haze Removal Using Dark Channel Prior”, *IEEE Transactions on Pattern Analysis and Machine Intelligence*, vol.33, no.12, pp.2341-2353, 2011.
- [84]K. Sooknanan, A. Kokaram, D. Corrigan, et al., “Improving underwater visibility using vignetting correction”, *in: Proc. of SPIE*, vol.8305, pp.83050M-1-8, 2012.
- [85]C. Xiao, J. Gan, “Fast image dehazing using guided joint bilateral filter”, *The Visual Compute*, vol.28, no.6/8, pp.713-721, 2012.
- [86]A. Rizzi, C. Gatta, D. Marini, “A new algorithm for unsupervised global and local color correction”, *Pattern Recognition Letters*, vol.24, pp.1663-1677, 2003.

- [87]R. Mantiuk, K.J. Kim, A.G. Rempel, W. Heidrich, “HDR-VDP2: A Calibrated Visual Metric for Visibility and Quality Predictions in All Luminance Conditions”, *ACM Transactions on Graphics*, vol.30, no.4, pp.40-52, 2011.
- [88]経済産業省, 海洋エネルギー・鉱物資源開発計画, 2009.
- [89]経済産業省, 海底熱水鉱床開発計画第1期最終報告書, 2013.
- [90]中谷 武志, “自律型水中ロボットによる沈没船の自動観測システムの研究開発”, 東京大学, 修士論文, 2006.
- [91]Y.Y. Schechner, N. Karpel, “Recovery of underwater visibility and structure by polarization analysis”, *IEEE Journal of Oceanic Engineering*, vol. 30 , no. 3 , pp. 570-587, 2005.
- [92]S. Bazeille, I. Quidu, L. Jaulin, J.P. Malkasse, “Automatic underwater image pre-processing”, in : *Proc. of Carcterisation Du Milieu Marin (CMM '06)*, pp.1-8, 2006.
- [93]R. Fattal, “Single image dehazing”, *ACM Transaction on Graphics*, vol.27, pp.1-8, 2008.
- [94]C.B. Nicholas, M. Anush, R.M. Eustice “Initial results in underwater single image dehazing”, in: *Proc. of IEEE OCEANS 2010*, pp.1-8, 2010.
- [95]K. He, J. Sun, X. Tang, “Guided image filtering”, *IEEE Transactions on Pattern Analysis and Machine Intelligence*, vol.35, no.6, pp.1397-1409, 2013.
- [96]S. Serikawa, H. Lu, “Underwater image dehazing using joint trilateral filter”, *Computers and Electrical Engineering*, vol.40, no.1, pp.41-50, 2014.
- [97]Q. Yang, N. Ahuja, R. Yang, K.H. Tan, J. Davis, B. Culbertson, J. Apostolopoulos, G. Wang, “Fusion of median and bilateral filtering for range image upsampling”, *IEEE Transactions on Image Processing*, vol.22, no.12, pp.4841-4852, 2013.

- [98] F. Terai, T. Uehara, T. Nakajima, "Technologies for disaster recovery support robots", *Toshiba Review*, vol.68, no.10, pp.34-37, 2013.
- [99] V. I. Haltrin, *Light Scattering Reviews*, Chapter 10: Absorption and scattering of light in natural waters, Springer Praxis Book, pp.445-486, 2006.
- [100] C.D. Mobley, *Light and Water*, Academic Press, San Diego, 1994.
- [101] M.I. Mishchenko, L.D. Travis, A.A. Lacis, *Scattering, Absorption, and Emission of Light by Small Particles*, Cambridge University Press, Cambridge, 2002.
- [102] J. Sivaswamy, Z. Salcic, K.L. Ling, "A real-time implementation of non-linear unsharp masking with FPLDs", *Real Time Imaging*, vol.7, pp.195-202, 2001.
- [103] F. Bonin, A. Burguera, G. Oliver, "Imaging system for advanced underwater vehicles", *Journal of Maritime Research*, vol.VIII, no.1, pp.65-86, 2011.
- [104] H. Lu, Y. Li, L. Zhang, A. Yamawaki, S. Yang, S. Serikawa, "Underwater optical image dehazing using guided trigonometric bilateral filtering", in: *Proc. of 18th IEEE International Symposium on Circuits and Systems (ISCAS2013)*, pp.2147-2150, 2013
- [105] H. Lu, Y. Li, S. Yang, S. Serikawa, "Adaptive Cross Image Filters for Underwater Image Enhancement", *International Journal of Computer, Consumer, and Control*, vol.2, no.2, pp.9-16, 2013.
- [106] Y. Zheng, S. Lin, S.B. Kang, R. Xiao, J.C. Gee, C. Kambhamettu, "Single-image vignetting correction from gradient distribution symmetries", *IEEE Transactions on Pattern Analysis and Machine Intelligence*, vol.35, no.6, pp.1480-1494, 2013.
- [107] H. Lu, S. Serikawa, L. Zhang, S. Nakashima, "Acoustic-optical image denoising using alpha-stable multivariate shrinkage function in the contourlet

domain”, International Journal of Computer, Consumer and Control, vol.2, no.3, pp.35-43, 2013.

[108] H. Lu, Y. Li, L. Zhang, A. Yamawaki, S. Yang, S. Serikawa, “Underwater optical image dehazing using guided trigonometric bilateral filtering”, in: Proc. of 18th IEEE International Symposium on Circuits and Systems (ISCAS2013), pp.2147-2150, 2013.

[109] S. Serikawa, H. Lu, “Underwater image dehazing using joint trilateral filter”, Computers & Electrical Engineering (Elsevier), vol.40, no.1, pp.41-50, 2014.

[110] Y. Li, H. Lu, L. Zhang, S. Serikawa, “Real-time visualization system for deep-sea surveying”, Mathematical Problems in Engineering, 437071, 2014.

Acknowledgments

First of all, I owe much to my supervisor Prof. Seiichi Serikawa for giving me the opportunity and the support to work on this very interesting research project. His insightful remarks and suggestions were invaluable for me during this period. I have learned much that will last longer than this dissertation.

I would like to thank Serikawa Laboratory staff, in particular Dr. Lifeng Zhang, Dr. Shiyuan Yang, Miss Yujie Li, Mr. Kohei Miyata, and Dr. Akira Yamawaki. During the undertaking of this project, the laboratory staffs have been very supportive and have provided a wonderful working environment. I am very grateful to all my friends in the Serikawa Laboratory for their tremendous support.

I wish also to express my appreciation to the entire reviewers of my thesis, Prof. Yoshihisa Nakato, Prof. Takeshi Ikenaga, and Prof. Hyungseop Kim for giving me some helpful comments and suggestions. Your support has been extremely helpful and I am a better person because of it.

Finally, I would like to thank the Japan Society for the Promotion of Science (No.25J10713) for supporting this research during my Ph.D. course.

APPENDIX A: Underwater Optical Imaging System

Motivation

- Deep-sea Mining System Monitoring
- Deep-sea AUV or ROV Visualization
- Deep-sea Biological Monitoring

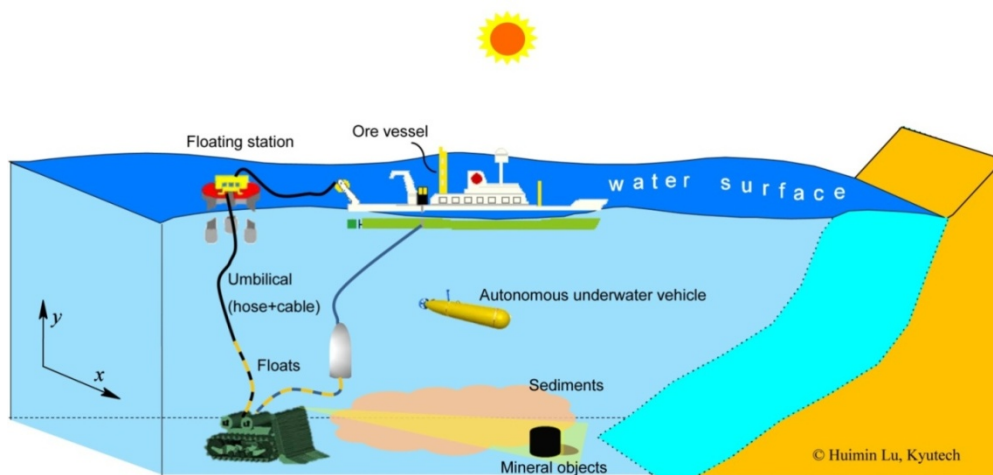


Figure A-1: Concept figure of deep-sea monitoring.

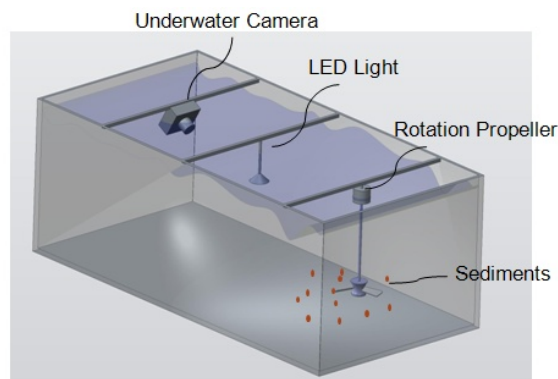


Figure A-2: Experimental Equipment Image.



(a)



(b)

Figure A-3: Equipment Sets.

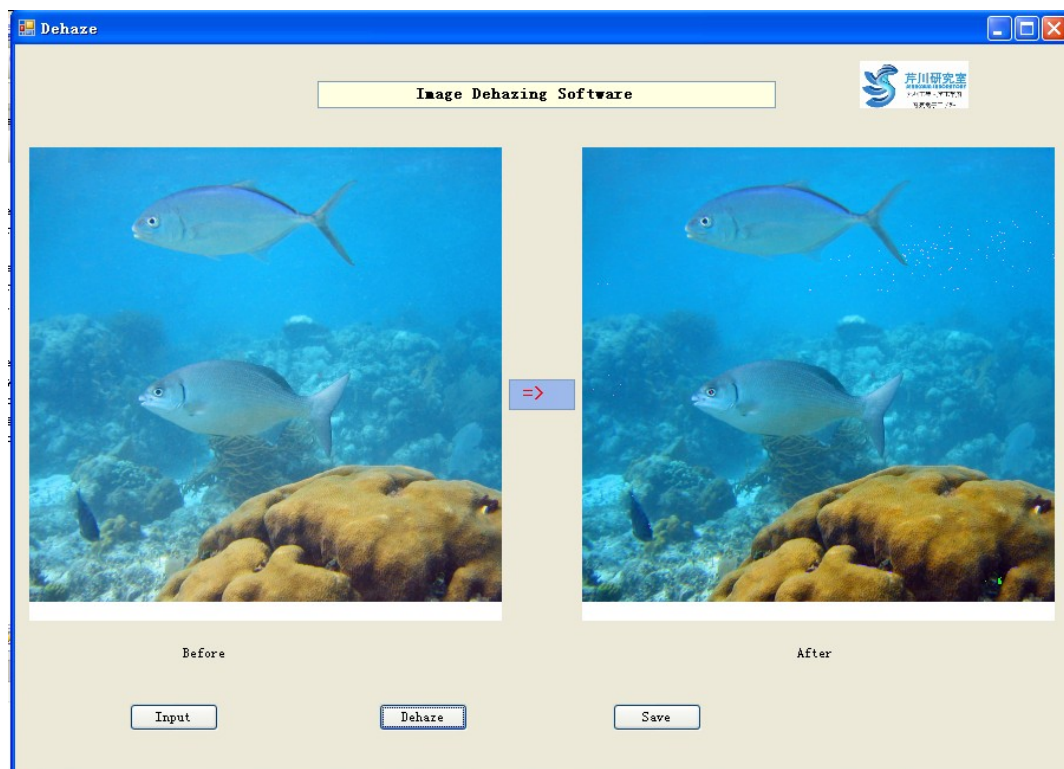


Figure A-4: Interface of Underwater Image Dehazing Software.

APPENDIX B: Publications

Journal Article

- [1] Huimin Lu, Lifeng Zhang, Seiichi Serikawa, “Maximum local energy: an effective approach for image fusion in beyond wavelet transform domain”, *Computers & Mathematics with Applications* (Elsevier), vol.64, no.5, pp.997-1004, 2012. (September 1, 2012).
- [2] Huimin Lu, Yujie Li, Lifeng Zhang, Seiichi Serikawa, “Enhancing underwater image by dehazing and colorization”, *International Review on Computers and Software* (Praise Worthy Prize), vol.7, no.7, pp.3470-3474, 2012. (December 1, 2012).
- [3] Huimin Lu, Shota Nakashima, Yujie Li, Lifeng Zhang, Yun Li, Seiichi Serikawa, “Underwater laser images denoising using bayesiancontourlet estimator of Bessel K Form”, *Innovative Computing, Information and Control Express Letters, Part B: Applications* (ICIC Express Letters Office), vol.4, no.3, pp.533-539, 2013. (June 1, 2013).
- [4] Huimin Lu, Akira Yamawaki, Seiichi Serikawa, “Curvelet approach for deep-sea sonar image denoising, contrast enhancement and fusion”, *Journal of International Council on Electrical Engineering* (The Korea Institute of Electrical Engineers), vol.3, no.3, pp.250-256, 2013. (July 1, 2013).
- [5] Yujie Li, Huimin Lu, Seiichi Serikawa, “Segmentation of offshore oil spill images in leakage acoustic detection system”, *Research Journal of Chemistry and Environment*, vol.17, no.S1, pp.36-41, 2013. (September 1, 2013).
- [6] Seiichi Serikawa, Huimin Lu, “Underwater image dehazing using joint trilateral filter”, *Computers & Electrical Engineering* (Elsevier), vol.40, no.1, pp.41-50, 2014. (January 1, 2014).
- [7] Yujie Li, Huimin Lu, Lifeng Zhang, Seiichi Serikawa, “Real-time visualization

system for deep-sea surveying”, *Mathematical Problems in Engineering*, 437071, 2014.

- [8] Huimin Lu, Yujie Li, Ling Chen, Seiichi Serikawa, “Image restoration using anisotropic multivariate shrinkage function in contourlet domain”, *International Journal of Computational Science and Engineering (Inderscience)*, In Press.

Conference Article

- [9] Huimin Lu, Yujie Li, Lifeng Zhang, Akira Yamawaki, Shiyuan Yang, Seiichi Serikawa, “Underwater optical image dehazing using guided trigonometric bilateral filtering”, in: *Proc. of 18th IEEE International Symposium on Circuits and Systems (ISCAS2013)*, pp.2147-2150, 2013, Beijing, China (May 19-22, 2013).
- [10] Huimin Lu, Yujie Li, Seiichi Serikawa, “Real-time underwater imaging system for mineral source location and concentration”, in: *Proc. of The 26th International Conference on Efficiency, Cost, Optimization, Simulation and Environmental Impact of Energy Systems (ECOS2013)*, G001, pp.1-15, 2013, Guilin, China (July 16-19, 2013).
- [11] Huimin Lu, Yujie Li, Seiichi Serikawa, “Underwater image enhancement using guided trigonometric bilateral filter and fast automatic color correction”, in: *Proc. of 20th IEEE International Conference on Image Processing (ICIP2013)*, pp.3412-3416, 2013, Melbourne, Australia (September 15-18, 2013).
- [12] Huimin Lu, Seiichi Serikawa, “Underwater scene enhancement using weighted guided median filter”, in: *Proc. of IEEE International Conference on Multimedia & Expo (ICME2014)*, Chengdu, China, accepted.